Max-Planck-Institut für Intelligente Systeme
(**ehemals Max-Planck-Institut für Metallforschung)**
Stuttgart

A new production method for Fresnel zone plates for high-resolution X-ray microscopy and investigation of their imaging properties

Marcel Wolfgang Richard Mayer

Dissertation
an der
Universität Stuttgart

Bericht Nr. 236
Juli 2011

A new production method for Fresnel zone plates for high-resolution X-ray microscopy and investigation of their imaging properties

Von der Fakultät Chemie der Universität Stuttgart
zur Erlangung der Würde eines Doktors der Naturwissenschaften
(Dr. rer. nat.) genehmigte Abhandlung

Vorgelegt von
Marcel Wolfgang Richard Mayer
aus Stuttgart

Hauptberichter: Prof. Dr. G. Schütz
Mitberichter: Prof. Dr. J. Bill
Prüfungsvorsitzender: Prof. Dr. E. J. Mittemeijer

Tag der mündlichen Prüfung: 12.07.11

Max-Planck-Institut für Intelligente Systeme Stuttgart
(ehemals: Max-Planck-Institut für Metallforschung Stuttgart)
2011

Richard und Ewald Kugler,
die uns leider zu früh verlassen haben.

Danksagung

Diese Arbeit entstand zwischen Februar 2008 und Mai 2011 am Max-Planck-Institut für Intelligente Systeme in Stuttgart, besser bekannt als das ehemalige Max-Planck-Institut für Metallforschung, in der Abteilung von Frau Prof. Dr. Gisela Schütz. Natürlich ist eine solche Arbeit ohne die Unterstützung von Kollegen, Familie und Freunden nicht durchführbar. Daher möchte ich bei dieser Gelegenheit allen beteiligten Personen für ihre Unterstützung danken.

Frau Prof. Dr. Gisela Schütz danke ich für die Überlassung dieses spannenden und herausfordernden Themas, mit dem wir Neuland in der Abteilung sowie in der Röntgenmikroskopie betreten haben.

Herrn Prof. Dr. Joachim Bill danke ich für seine freundliche Bereitschaft, den Mitbericht für diese Arbeit übernommen zu haben.

Meiner Betreuerin, Frau Dr. Corinne Grévent, danke ich für ihre Unterstützung, die maßgeblich zum Gelingen dieser Arbeit beigetragen hat. Trotz aller Widrigkeiten hat sie stets an das Projekt geglaubt und wir sind fast immer zu einer Lösung gekommen.

Unseren Kooperationspartnern aus Halle an der Saale, Herrn Dr. Mato Knez und Frau Dr. Adriana Szeghalmi, danke ich für die Möglichkeit ihre ALD-Anlagen benutzen zu dürfen und die freundliche Aufnahme in ihre Gruppe während meiner Aufenthalte dort.

Herrn Dr. Michael Hirscher und Frau Ulrike Eigenthaler danke ich für die Hilfe und Unterstützung alle Fragen das FIB betreffend und für so manche Überstunde beim Präparieren allerlei Proben.

Markus Weigand und Michael Bechtel danke ich für die tolle Unterstützung während der MAXYMUS-Strahlzeiten.

Dr. Anatoly Sigirev and Dr. Irina Snigireva, I want to thank you very much for your support during our ESRF beamtimes, for amusing storries around the X-ray community one would not find in any book or paper and the very interesting introduction into the field of hard X-rays.

Frau Marion Kelsch und Frau Ute Salzberger vom Stuttgarter Zentrum für Elektronenmikroskopie danke ich für ihren tollen Einsatz bei der Präparation und der Untersuchung der TEM-Proben.

Herrn Dr. Gerd Schneider und Herrn Dr. Stefan Rehbein danke ich für die Überlassung und die Einführung in das ZPTGW-Programm und so manches, was es über Zonenplatten sonst noch zu wissen gibt.

Dem technischen Stab der Abteilung Schütz und den verschiedenen Servicegruppen und Werkstätten an den beiden Max-Planck-Instituten in Stuttgart danke ich für ihre Unterstützung bei der Durchführung so mancher Spezialaufgabe.

Meinen Kollegen danke ich für die lustigen Kaffeerunden, die witzigen Abende im "Joe Penas" und die allgemein freundliche und nette Arbeitsatmosphäre.

Last but not least möchte ich mich aufs Allerherzlichste bei meiner Familie bedanken, die mir mein Studium nicht nur ermöglicht, sondern mich auch bei jedem Schritt nach Kräften unterstützt hat.

Zu allerletzt, das Beste kommt ja immer zum Schluss, möchte ich mich bei meiner Freundin Stephanie bedanken, die mit mir durch dick und dünn (sprichwörtlich und wörtlich) gegangen ist und die immer für mich da war. Ich werde mich dafür revanchieren!

List of abbreviations

(SP)CVD	(surface plasma) chemical vapour depositiion
(U)HV	(ultra-)high vacuum
AFM	atomic force microscopy
ALD	atomic layer deposition
ALE	atomic layer epitaxy
ALS	Advanced Light Source
APD	avalance photodiode
BESSY	Berliner Elektronen Speicherringgesellschaft für Synchrotronstrahlung
CCD	charge coupled device
CRL	compound refractive lens
CWT	coupled wave theory
DC	direct current
EBL	electron beam lithography
ESRF	European Synchrotron Radiation Facility
EUV	extreme ultra violet
FIB	focused ion beam
FWHM	full width at half maximum
FZP	Fresnel zone plate
GIS	gas injection system
K-B	Kirkpatrick-Baez

LIGA ..... Lithographie Galvanik Abformung

LINAC ..... linear accelerator

LMIS ..... liquid metal ion source

MAXYMUS ..... magnetic X-ray microscope and UHV Spectroscope

MLL ..... multilayer Laue lens

MOTB ..... microoptics test bench

MPI ..... Max-Planck-Institute

NA ..... numerical aperture

OSA ..... order sorting aperture

PGM ..... plane grating monochromator

PID ..... proportional-integral-derivative

PLD ..... pulsed laser deposition

PMT ..... photo multiplier tube

rf ..... radio frequency

RIE ..... reactive ion etching

S(T)XM ..... scanning (transmission) X-ray microscope

SEM ..... sanning electron microscope

SLS ..... Swiss light source

TEM ..... transmission electron microscope

TFEL ..... thin film electroluminescent

TMA ..... Trimethylaluminium

TXM ..... transmission X-ray microscope

VASE ..... variable angle sectroscopic ellipsometry

Contents

Chapter 1

Introduction

Since the discovery of X-rays by Wilhelm Conrad Röntgen at the university of Würzburg in 1895 [1, 2] numerous attempts have been been brought forward to utilize their inherent properties. In particular their short wavelength and large penetration depth have been exploited for simple imaging and diffraction and later for microscopy purposes, beyond the optical limit. The hardest task, in the practical implementation of an X-ray microscope was, due to the exceptional properties of X-rays, the development of effective and reliable focusing devices, which provide high resolution and high efficiency combined with little or no aberrations. Therefore, several kinds of focusing devices in the form of mirrors [3], refractive lenses [4] and diffractive optics [5] have been developed. Mirrors under grazing incidence show, even if they are perfectly made, optical aberrations when they are used for imaging of extended objects. Nowadays they are mainly used as pre focusing optics in synchrotron X-ray beam lines and in astronomy. Refractive lenses in the form of compound refractive lenses (CRL) can be used for imaging only in the hard X-ray regime. Due to the low efficiency of a single lens, stacks of many lenses have to be used. An extension of their field of application into the soft X-ray regime is not possible. The most widely used X-ray optical elements when it comes to high resolution X-ray microscopy, especially in the soft X-ray regime, are diffractive optics in the form of Fresnel zone plates (FZP).

The Fresnel zone plate [6] is a circular diffraction grating with an outwardly increasing line density. It creates point foci of different order via constructive interference. Zone plates are highly chromatic and therefore have to be used with radiation of a narrow spectral bandwidth to show diffraction limited focusing. Their focal length (f) is defined

by their diameter (D), the wavelength (λ) of the light they are used at and their outermost zone width (Δr), which also determines their spatial resolution.

Among other techniques, Fresnel zone plates are nowadays mainly produced by processes involving electron beam lithography (EBL) [7]. In this approach, a substrate is coated with an electron sensitive resist, the zone pattern is written into the resist and after its development, transferred into another material by deep etching and/or electroplating. With special variants of the lithographic approach, resolutions down to 9 nm have been achieved [8], with reasonable efficiencies in the soft X-ray regime. Restrictions in the aspect ratio prevent however to create high resolution zone plates for the hard X-ray regime with simple lithography based techniques. In a different approach, the so called "sputter-sliced" technique [9], consecutive layers of absorbing or phase shifting and transparent material are deposited onto a rotating wire by sputter deposition. After the deposition, the coated wire is embedded, sectioned and thinned with mechanical techniques. Sputter-sliced zone plates suffer from poor layer qualities and their restriction to the hard X-ray regime due to the large minimal thicknesses achievable with mechanical sectioning and thinning techniques. Extensive imaging could not be performed with these zone plates.

In summary it can be stated that besides the attempts to manufacture zone plates by lithography, as well as by sputter-sliced techniques, it is also necessary to develop new approaches for zone plate manufacturing, presenting new possibilities in terms of high resolution, high efficiency and applicability over a wide range of the X-ray optical spectrum, which can circumvent the restrictions of the established techniques. Envisaged processes should ideally be reliable, flexible and productive. Furthermore they should be able to produce high resolution and high efficiency zone plates which are applicable over a wide range of the X-ray spectrum. Hence, the aim of this thesis is to present a new manufacturing process which inherently meets these requirements. The new method derives from the sputter-sliced approach but relies on a new and unique combination of techniques which has never been applied to Fresnel zone plate production. The initial point of the approach lies in the multilayer deposition of an absorbing and a transparent material on a glass fibre substrate by atomic layer deposition (ALD) [10]. The thicknesses of the layers hereby follow very closely the zone plate design rule (equation 2.9). ALD has several advantages over sputtering which include a high conformality of the deposited layers, a good adhesion of the films on the substrate and a low interface roughness in

multilayer deposition. In contrast to physical deposition methods like sputtering, films in ALD are deposited in the form of cycles, where each cycle leads to the deposition of one atomic layer under ideal conditions. The method will be treated extensively in section 3.1. After the deposition the Fresnel zone plate is cut from the coated fibre with focused ion beam (FIB) [11], which will be introduced section 3.2. The use of this sophisticated technique also offers significant advantages over the established mechanical techniques. The thickness of the lens can be chosen, from a few tens of micrometres, down to a few hundred nanometres. Therefore, zone plates suitable for a wide range of X-ray energies can be produced. Furthermore the FIB offers very clean cuts, avoiding any scratches on the surface or distortions of the layer structure, which occur when a sample is mechanically polished. The inherent properties of this technique show, that it is suited for the production of high resolution zone plates for both the soft and the hard X-ray regime.

With this new approach, it was for the very first time possible to achieve diffraction limited focusing with multilayer based FZPs and thus high resolution imaging in the soft X-ray regime. The generation of a symmetrical, high intensity focal spot is a major improvement, compared to former attempts with sputter-sliced zone plates in the hard X-ray regime. In addition, the new zone plate could also be used as objective lens in full-field X-ray microscopy. The pioneering work of this thesis sets the foundation stone for many possible future developments based on the principle of FZP manufacturing by ALD deposition and FIB preparation.

The thesis is outlined as follows: In chapter 2 the generation of X-rays in 3^{rd} generation synchrotron light sources and the fundamental properties of X-rays, as well as the basic concepts of X-ray microscopy and X-ray focusing elements are described. As Fresnel zone plates have an exceptional status as focusing elements in X-ray microscopy and because the development of a new manufacturing process for FZPs is the main goal of this thesis, FZPs are described theoretically and practically in detail.

In chapter 3 the main experimental methods employed in this thesis are described in detail. First the basic principles of atomic layer deposition are explained. Then, the Picosun ALD reactor SUNALE^{TM} R100, which has been used in this study is described. In the second part of this chapter, the FEI Nova NanoLab 600 DualBeam^{TM} instrument (combining SEM and FIB), which has been used for the different preparation steps in

the sectioning and thinning procedure is explained, together with some fundamentals of scanning electron and focused ion beam microscopy. In the final part of this chapter, the setups used to test the zone plates are presented. For the soft X-ray regime, the scanning X-ray microscope (SXM) of the Max-Planck-Society MAXYMUS, which has been installed at BESSY II, Berlin in November 2009, has been used. For the hard X-ray regime, two dedicated setups have been constructed, one for the qualitative evaluation of the zone plates and one for full-field imaging, both installed at the microoptics test bench (MOTB) at beamline ID6 at the European Synchrotron Radiation Facility (ESRF) in Grenoble, France.

In chapter 4 the results of the thesis are presented. In the first part, calculations of the diffraction efficiency to identify a suited material combination for the zone plate, as well as their optimal thickness are shown. Then the fabrication of the FZPs is described. Finally, the results of the investigation of the zone plates in terms of electron microscopy and X-ray optical performance are shown.

In chapter 5 the results are discussed and set in context to other attempts found in the literature, to produce FZPs.

The thesis concludes with a summary (6.1) of the results and an outlook (6.2) on future possibilities of this new and promising approach and a summary in German language (chapter 7).

Chapter 2

Fundamentals and state of technology

In this chapter, the generation of X-rays in electron storage rings will be briefly described. Then the fundamental interactions of x-rays with matter, which are needed to understand the different approaches for X-ray focusing, will be introduced. As two of the most important X-ray microscopy methods, the zone plate based techniques, scanning (STXM) and full-field (TXM) X-ray microscopy will be introduced. Then, an introduction to different X-ray focusing methods will be given. As Fresnel zone plates (FZP) have an outstanding status among the X-ray focusing elements, and because the aim of this work is the introduction of a new manufacturing method for FZPs, their properties and manufacturing will be presented in more detail, presenting the problems, encountered with current manufacturing methods.

2.1 Synchrotron sources and X-ray interactions with matter

2.1.1 Generation of X-rays

Nowadays, 3^{rd} generation electron storage rings serve as very bright sources for synchrotron radiation. The basic characteristics of such a light source and the electron storage rings of BESSY II in Berlin and of the ESRF in Grenoble, where the experiments for this thesis have been performed, are described in the following.

Synchrotron radiation

Electromagnetic radiation is generated when charged particles are accelerated. This effect is exploited in the preferred light source for X-ray microscopy, the electron storage ring, where highly relativistic electrons are forced onto a closed circular path by magnetic fields and emit X-rays tangential to their direction of motion. An extensive overview of accelerator physics including synchrotron science since the development of the synchrotron principle in 1945 is given in [12]. The experiments of this thesis have been performed at BESSY II for the soft, and at the ESRF for the hard X-ray regime, respectively. The technical realisation of a synchrotron is described for the storage ring BESSY II as an example for a 3^{rd} generation light source in figure 2.1 (adopted from [13]). At BESSY II,

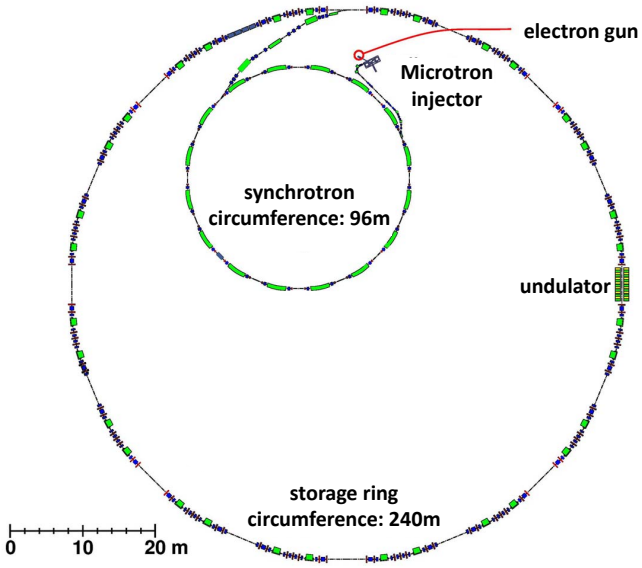

Figure 2.1: Schematic illustration of BESSY II. Electrons are generated in an electron gun and pre-accelerated in a microtron. Then they are transferred to the synchrotron, where they are further accelerated to their final energy of 1.7 GeV. The electrons are then injected into the storage ring where they circulate for several hours. Light is generated in bending magnets or insertion devices (wigglers or undulators).

the electrons are generated in an electron gun where they are accelerated to an energy of 70 keV. The next stage of acceleration to an energy of 50 MeV is performed in a microtron. Other light sources, like the ESRF, use linear accelerators (LINAC) for this purpose. For the final acceleration the electrons are transferred to the synchrotron where their kinetic energy is further increased by one or several rf-cavities, until they reach the energy of the storage ring. This energy is 1.7 GeV at BESSY II and 6 GeV at the ESRF. Finally

the electrons are injected into the storage ring (circumference of 240 m and 844 m for BESSY II and the ESRF, respectively) where they circulate for several hours. The whole environment is held under UHV-conditions (10^{-9} to 10^{-10} mbar).

Two different methods are used in electron storage rings to create light, bending magnets and insertion devices (undulators or wigglers). Both types of light emitting devices are shown schematically in figure 2.2 (a) reproduced from [14] and b) reproduced from [15]). In the magnetic field of a bending magnet (figure 2.2 a)), the electrons are

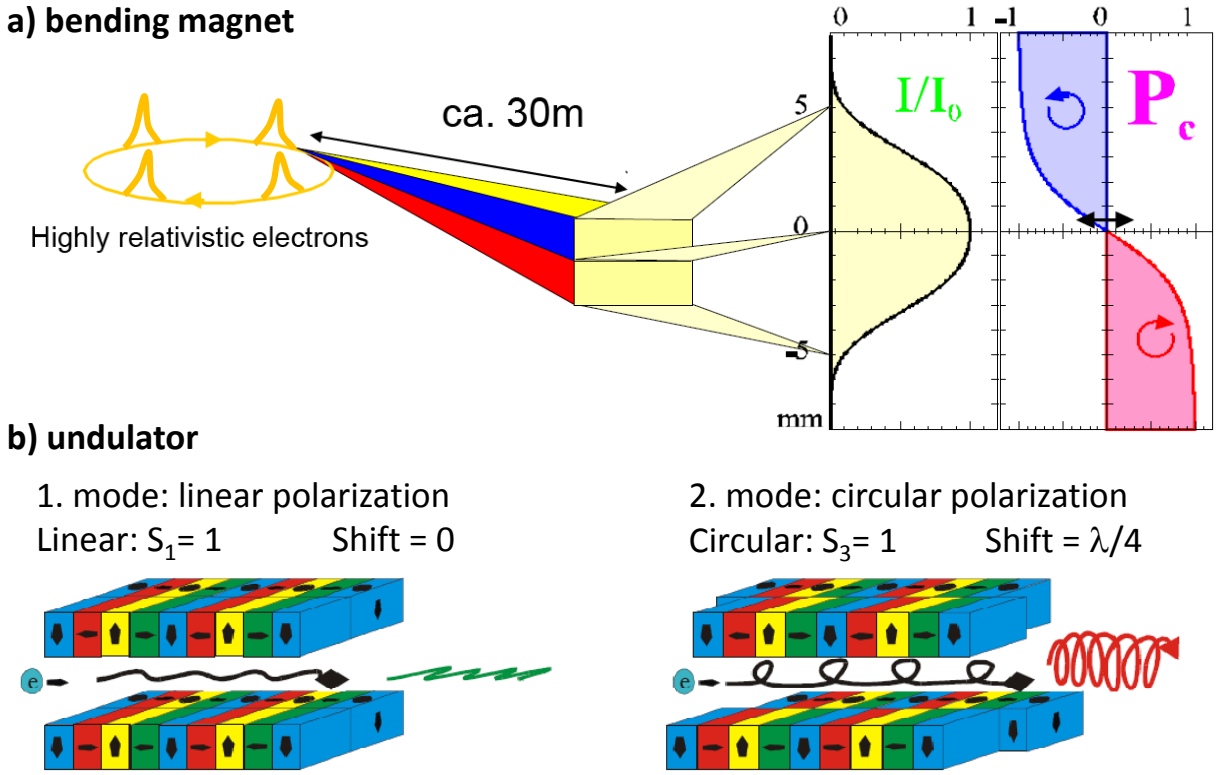

Figure 2.2: Schematic illustration of two light generating devices in a storage ring, the bending magnet and the undulator. a) In the bending magnet, the electrons are accelerated towards the center of the storage ring by a magnetic field. Due to their relativistic velocity, they emit highly collimated radiation, tangential to their direction of motion. b) In the undulator, the electrons are forced on an oscillating path by permanent magnets above and below the electron beam plane. The polarization of the emitted X-rays can be changed by shifting the permanent magnets with respect to each other.

accelerated towards the center of the storage ring, therefore they emit radiation tangential to their direction of motion, with a continuous distribution of wavelengths from the

infra-red, far into the X-ray regime. Because the velocity of the electrons approaches the light velocity c, the cone of emittance does not resemble the typical dipole emittance, but is strongly directed in forward direction and highly collimated. The radiation is linearly polarized in the plane of emittance and circularly polarized, with opposite helicities, above and below the plane of emittance. Circularly polarized light is especially important in magnetic studies [16]. In 3^{rd} generation storage rings like BESSY II or the ESRF, which are optimized for the generation of light, the straight sections of the storage ring are equipped with so called "insertion devices" like undulators or wigglers which represent the second source for synchrotron radiation. An undulator (figure 2.2 b)) typically consists of arrays of magnetic structures, usually permanent magnets, above and below the electron beam plane. The magnets are arranged in a way to force the electrons on a oscillating path with small deflections. The radiation which is generated in every reversal point interferes constructively or destructively in forward direction, leading to a high brilliance and a spectrum containing distinct harmonics. To coarsely change the wavelength of the radiation, the gap between the upper and the lower magnetic array is changed. The polarisation is changed by sliding the different magnetic arrays with respect to each other. Due to its high brilliance and high degree of coherence, undulator radiation is the preferred source of X-rays for STXM. To achieve the very fine energy resolution ($\frac{\Delta E}{E}$) of 10^{-3} to 10^{-4}, which is necessary for spectroscopic studies and to achieve diffraction limited resolution in the STXM, a monochromator in the form of a plane grating (typical for the soft X-ray range) or a Si-double-crystal monochromator (typical for the hard X-ray range) is implemented in the beam line.

Figure 2.3 (adopted from [17]) shows a comparison of the brilliance of X-rays generated in X-ray tubes (Continuum (bremsstrahlung), carbon K, copper L and K, aluminium K and molybdenum K) and X-rays generated in 3^{rd} generation light sources in bending magnets (Bends) and insertion devices (Undulators and Wigglers) for a light source with 1.9 GeV respectively 7 GeV beam energy. Radiation from undulators shows a several orders of magnitude higher brilliance than bending magnet radiation.

- A high brilliance of the source, allows short measurement times.
- Energy tuneability and high spectral resolution using monochromators, allows to select the absorption edges of the sample, to perform exact energy scans and to achieve diffraction limited focusing.

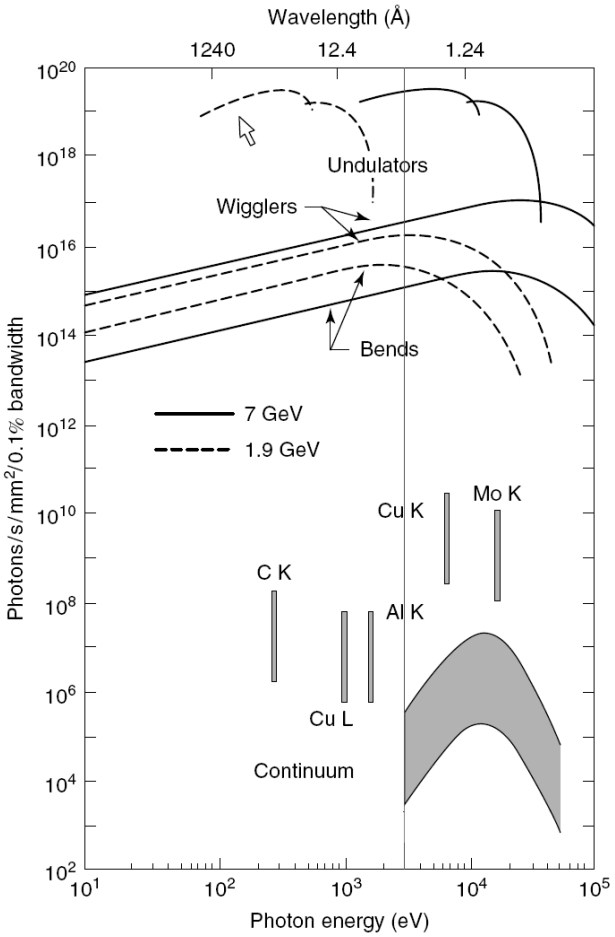

Figure 2.3: Comparison of the brilliance of different X-ray sources. Continuum (bremsstrahlung), carbon K, copper L and K, aluminium K and molybdenum K originate from X-ray tubes, the others from 3^{rd} generation electron storage rings. These sources show several orders of magnitude higher brilliance than X-ray tubes.

- Tunable polarization (linear, circular) of the X-rays, used to achieve magnetic contrast.

This is why most X-ray microscopes are operated at 3^{rd} generation electron storage rings.

2.1.2 Interactions of X-rays with matter

In this section, the main interactions of X-rays with matter (reflection, absorption and phase shift) are presented. Starting with the general description of reflection, two different cases are regarded in more detail: total external reflection and reflection from multilayers. Then the absorption and the phase shift of an X-ray wave in a homogeneous medium are

calculated. The equations used in this section have been adopted from [6] if not cited differently.

Reflection

If a electromagnetic wave (i.e. light) encounters an interface between two media with different index of refraction, the wave usually undergoes reflection and refraction. This is illustrated in figure 2.4 (adopted from [6]) for the interface between vacuum (n = 1) and an arbitrary material with the complex refractive index n = 1 - δ + i β, where ϕ is the angle of

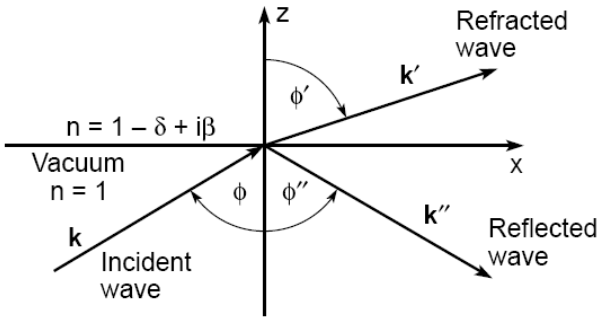

Figure 2.4: Illustration of the reflection/refraction of an X-ray wave at the interface between vacuum and a material of refractive index n = 1 - δ + i β.

the incident wave to the surface normal and ϕ' the angle between the refracted wave and the surface normal. The reflection angle ϕ" is equal to the incidence angle ϕ because both waves travel in the same medium. The angle of the refracted wave ϕ' can be calculated from the incidence angle ϕ and the index of refraction n of the medium by using *Snell's* law (equation 2.1):

$$\begin{aligned} \sin\phi' &= \frac{\sin\phi}{n} \\ \text{where } n &= 1 - \delta + i\beta. \end{aligned} \tag{2.1}$$

In the case of X-rays, the index of refraction has to be written as a complex quantity to account for absorption, as it plays a significant role at those energies. The frequency dependent index of refraction of a material *n(ω)* is strongly related to the atomic scattering factors and can be written in the form of its complex components as (equation 2.2):

$$n(\omega) = 1 - \delta + i\beta = 1 - \frac{n_a r_e \lambda^2}{\pi}\left[f_1^0(\omega) - i f_2^0(\omega)\right], \tag{2.2}$$

where δ is the phase shift and β the absorption, n_a is the number density of atoms per unit volume, r_e is the classical electron radius and λ is the wavelength[1]. Equation 2.2 shows, that the coefficients δ and β of the refractive index can be expressed in terms of the atomic scattering factors f_1^0 and f_2^0 (equations 2.3a and 2.3b):

$$\delta = \frac{n_a r_e \lambda^2}{2\pi} f_1^0(\omega) \tag{2.3a}$$

$$\beta = \frac{n_a r_e \lambda^2}{2\pi} f_2^0(\omega). \tag{2.3b}$$

For visible light, the index of refraction is larger than unity (typically around 1.5 for common glass), this leads to a deceleration of the phase velocity and a retardation of the phase in the material. For X-rays however, the index of refraction is slightly less than unity (δ and β, are positive and very small), wherefore, the phase velocity of X-rays in a material is slightly larger than in vacuum and the phase in general advances when X-rays pass through matter. The transition illustrated in figure 2.4 hence takes place from a medium with a refractive index of $\mathrm{n} = 1$ (vacuum) to a material with a refractive index slightly smaller than 1 ($\mathrm{n} = 1 - \delta + \mathrm{i}\,\beta$).

Total external reflection If the absorption in the medium is considered negligible ($\beta \to 0$), the index of refraction becomes $\mathrm{n} = 1 - \delta$. In this case, as δ is positive, it follows that n is smaller than 1 and therefore, the wave is refracted away from the surface normal for all incidence angles. If the incidence angle approaches 90°, the refraction angle ϕ' can reach $\frac{\pi}{2}$ and the refracted wave propagates along the surface of the medium, instead of penetrating it. This occurs at the so-called *critical angle of incidence* $\phi = \phi_c$. The complementary angle, measured from the incoming wave to the surface of the medium, $\theta_c = 90° - \phi$ is called the *critical angle for total external reflection* which has first been observed by Compton in 1922 [18], and is given by (equation 2.4):

$$\theta_c = \sqrt{2\delta} = \sqrt{\frac{n_a r_e \lambda^2 f_1^0(\lambda)}{\pi}}, \tag{2.4}$$

where all variables have the same meaning as in equation 2.3a. The atomic density in atoms per unit volume n_a varies slowly among the the natural elements. Therefore, the

[1] A positive imaginary part for the refractive index has been chosen, following Attwood [6] (page 20 and 60) to be consistent with his formulations for the calculation of absorption.

functional dependencies of the critical angle are $\theta_c \propto \lambda\sqrt{Z}$ because the optical constant $f_1{}^0$ can be approximated with Z [6] (p. 71).

If absorption is not neglected ($\beta \nrightarrow 0$), the assumption that the incoming wave propagates along the interface does not hold any more, some energy flows into the medium and the fields of the wave inside the material decay with an exponential dependence. The penetration depth of the wave into the medium z is greatest at the critical angle ($\theta = \theta_c$) and can be calculated to be $z_c \backsimeq \frac{\lambda}{2\pi\beta^{1/2}}$.

Reflection from multilayer structures At normal incidence the reflectivity $R_\perp$ of a material with the refractive index $n = 1 - \delta + i\beta$ can be calculated as $R_\perp \simeq \frac{\delta^2+\beta^2}{4}$. As δ and β are very small for all materials, $R_\perp$ is nearly zero if only a single interface is present. The situation is different if multilayer interference coatings (or multilayer mirrors) are used that consist of alternating thin layers of high and low Z materials. They present a periodically changing refractive index. Their periodicity d (one pair of layers) is designed to be $d = \lambda/2$ at normal incidence illumination to achieve constructive interference of the reflected intensity.

At non-normal incidence the conditions of reflection for a multilayer interference coating are described by *Bragg's* law (equation 2.5):

$$m\lambda = 2d \sin\theta\sqrt{1 - \frac{4\bar{\delta}d^2}{m^2\lambda^2}}, \tag{2.5}$$

which has been complemented with a square root factor. This factor contains the quantity $\bar{\delta}$ which is the bilayer weighted real part of the refractive index, the design wavelength λ, the reflection order m = 1, 2, 3,... and the incidence angle to the surface, θ.

Absorption and phase shift

Based on the complex index of refraction, used to describe the reflection of an X-ray wave, we can also calculate the absorption and the phase shift of a wave as it passes in x-direction through a material. For a plane wave in a homogeneous medium of refractive

index n = 1 - δ + i β we can write [19] (equation 2.6):

$$\psi(x) = Ae^{-inkx} = Ae^{-ikx}e^{-i\delta kx}e^{-\beta kx}, \tag{2.6}$$

where A is the amplitude and k = $\frac{2\pi}{\lambda}$ is the wave vector of the plane wave. The first factor (e^{-ikx}) represents the propagation of the wave in vacuum, the second ($e^{-i\delta kx}$) is responsible for the phase shift and the third ($e^{-\beta kx}$) accounts for the decay of the wave due to absorption.

The intensity I of the wave after the propagation through a material with the thickness t can be calculated by taking the modulus squared of ψ(t) and thus obtaining (equation 2.7):

$$I_t = I_0 e^{-\mu t}, \tag{2.7}$$

where $\mu = 2\beta k = 4\pi\beta/\lambda$ is the linear absorption coefficient known from the *Beer–Lambert* law. The inverse (μ^{-1}) is the penetration depth for X-rays of wavelength λ and a material with the optical constant β. It is the distance after that the intensity has decreased by a factor e.

The phase shift $\Delta\phi$ of the wave when it has travelled through the thickness t amounts to (equation 2.8):

$$\Delta\phi = 2\delta kt = \frac{2\pi}{\lambda}\delta t. \tag{2.8}$$

The phase shift does not lead to an attenuation of the wave but to an angular redistribution of the transmitted intensity. In visible light optics, this would correspond to the deflection of a monochromatic beam of light when it is sent through a prism at non-normal incidence.

2.2 X-ray microscopy

Several lensless [20] and lens based [21] approaches with manifold applications exist in X-ray microscopy. Here, the two main zone plate based microscopy techniques, the scanning transmission X-ray microscope and the full-field transmission microscope are introduced. An overview of the whole setup, from the light source to the microscope is illustrated in figure 2.5 (b) adopted from [22]) for a) a STXM and b) the TXM XM-1 at the ALS in

Berkeley, USA.

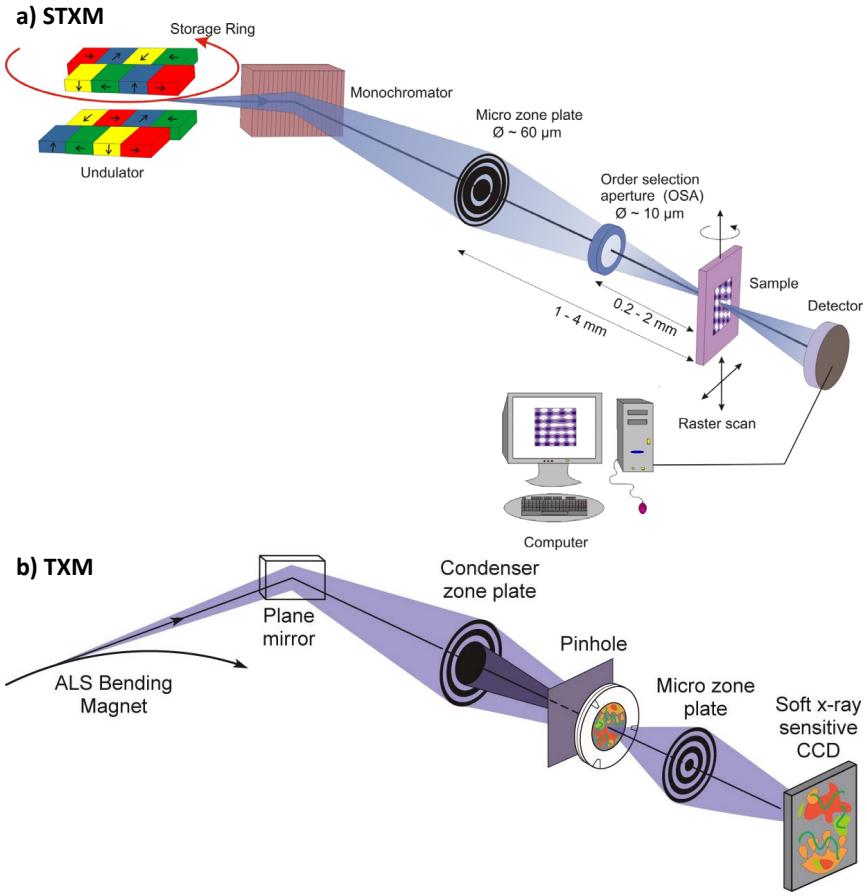

Figure 2.5: Illustration of two X-ray microscopy beamlines. a) STXM and b) TXM (XM-1). In both beamlines, a monochromator is implemented to achieve high energy resolution.

2.2.1 Scanning transmission X-ray microscopy

The basic principle of a zone plate based scanning transmission X-ray microscopy is shown in figure 2.6 (adopted from [6]). The concept of the STXM has been pioneered by H. Rarback, J. Kirz and co-workers [23]. In this type of microscope, nearly parallel, monochromatic and coherent X-rays are focused to a diffraction limited spot by means of a Fresnel zone plate, the size of the focal spot on the sample determines the resolution of the microscope. The FZP is equipped with an opaque center stop and an order sorting aperture (OSA) is placed between FZP and sample to block higher and the 0^{th} diffraction order. While scanning the sample or the zone plate, the transmitted radiation is recorded

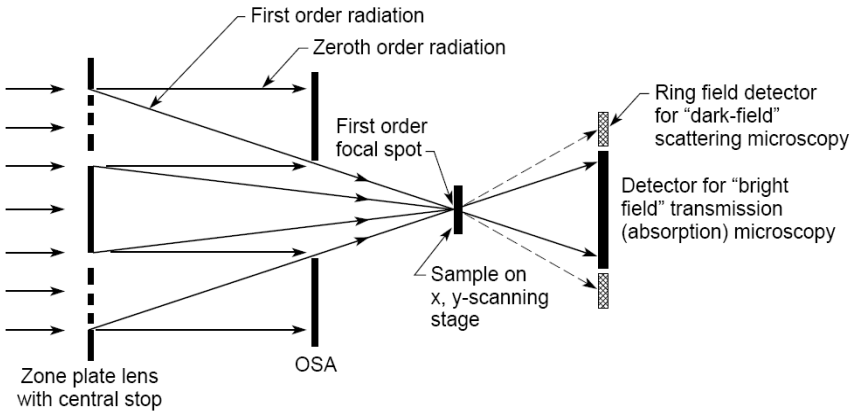

Figure 2.6: Schematic illustration of the STXM. Nearly parallel X-rays are focused to diffraction limited spot on the sample. A OSA and a center stop block higher order and 0^{th}-order radiation. FZP or sample are raster scanned and the transmitted radiation is collected to compose an image.

with a point detector, typically a photomultiplier tube (PMT) or an avalanche photodiode (APD).

2.2.2 Full-field X-ray microscopy

The basic principle of the full-field or transmission X-ray microscopy is shown in figure 2.7 (adopted from [6]). This type of microscope has been pioneered by G. Schmahl, D.

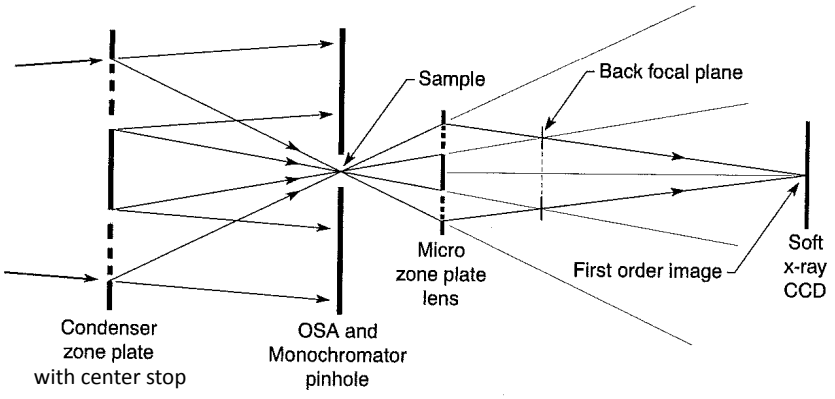

Figure 2.7: Schematic illustration of the TXM. A condenser zone plate with a center stop (not shown) is used to illuminate the sample. A micro zone plate creates a highly magnified image on a CCD-camera.

Rudolph and colleagues [24, 25]. In principle a TXM works in the same manner as a visible light microscope. A condenser zone plate or a glass capillary [26] is used to illuminate the sample on an area of several square micrometers. The condenser is often rotated or wobbled to make the illumination more homogeneous and to break the coherence of the light. This is necessary in order to avoid interference effects which result in speckles in the image [27]. If a zone plate is used as condenser, an OSA is applied to block unwanted radiation. In the case of a capillary, no higher orders exist, and the beam has already been monochromatized so that no OSA is necessary [28]. In both cases, a center stop has to be applied to block the 0^{th}-order radiation and to create hollow cone illumination necessary to achieve best resolutions [6] (page 364/365). Down stream of the sample, a micro zone plate is used as objective lens to create a highly magnified image of a large sample area on an X-ray sensitive CCD-camera in a single exposure. The distance between micro zone plate and CCD can be several meters which creates magnifications of several thousand. While, the quality of the illumination can somewhat improve the overall resolution, the resolution of the microscope is mainly determined by the resolution of the micro zone plate.

2.3 X-ray focusing optics

Various approaches exist, to focus X-rays [29, 30]. Some of these methods are presented in this paragraph. First, mirrors, capillary optics and refractive lenses which rely on reflection from surfaces and refraction, respectively will be briefly reviewed. Then Fresnel zone plates as diffractive X-ray optical devices and the main topic of this thesis will be treated in detail.

2.3.1 X-ray mirrors

Nowadays, several types of mirrors exist for X-ray focusing [3]. In 1948 P. Krikpatrick and A. Baez introduced the concept of using two crossed mirrors with spherical concave shape under grazing incidence to focus X-rays [31]. The use of two crossed mirrors equals the effect of two crossed cylindrical lenses for visible light. As mirrors under gazing incidence show very severe astigmatism, the second mirror is set orthogonal to the first mirror to correct for its astigmatism. Nevertheless, imaging of extended objects suffers form strong aberrations. Due to the lack of other X-ray optics, microscopes containing mirrors in the Kirkpatrick-Baez geometry have nevertheless been build [32]. Nowadays, Kirkpatrick-Baez (K-B) mirrors are mainly used as focussing optics in synchrotron X-ray beamlines, where focal spot sizes below 50 nm have been achieved [33]. An immediate

application in high resolution X-ray microscopy is yet prevented by the asymmetry of the focal spot and the complicated and time consuming fabrication of very high resolution K-B-mirrors which require elliptical profiles with ultra smooth surfaces [34, 35].

Another approach to use mirrors as focusing elements for X-rays has been proposed by H. Wolter in 1952 [36]. Wolter optics consist of two mirrors, one with parabolic or elliptic rotational symmetry and the second with hyperbolic rotational symmetry. Internal (*Wolter mirror type I*) and external (*Wolter mirror type II*) reflection from the hyperbolic mirror surface is hereby used to achieve a shorter or longer focal length. Wolter optics are used for example in the satellite XMM-Newton which consists of 58 Wolter type I grazing-incidence mirrors [37]. Similarly to K-B-mirrors, Wolter mirrors set high requirements for the smoothness of the mirror surface.

A third important type of reflecting optics are multilayer mirrors or interference coatings [38]. They rely on Bragg-reflection at the interfaces of the multilayer structure as introduced in the previous section (equation 2.5). The multilayer structure has to consist of a low Z and a high Z material to achieve a large difference in the refractive indices at the interface. The low Z material, which acts as a spacer, should have optical constants (δ and β) which are as low as possible to achieve low absorption and a large difference to the optical constants of the high Z material whose thickness is reduced as much as possible, to minimize absorption. To ensure an optimal functioning of these mirrors, the thicknesses of the layers have to be controlled very accurately. In addition, the interfaces have to be as sharp as possible to achieve high reflectivity and the films should be amorphous to avoid reflections form crystallites. A high reflectivity, approaching unity, even when absorption in the layers is present can be achieved with about 100 interfaces. Multilayer mirrors also act as bandpass filters with an energy resolution $\left(\frac{\lambda}{\Delta\lambda}\right)$ of 10 up to 100. Multilayer mirrors have been fabricated with nearly every thin film deposition technique [39]. The most widely used method is sputtering [40]. Other methods include evaporation [41], pulsed laser deposition (PLD) [42] and recently atomic layer deposition (ALD) [43]. Applications of multilayer mirrors include astronomy [44], EUV lithography for semiconductor manufacturing [45] and photoemission microscopy [46]. Very recently sub-10 nm focusing has been demonstrated in the hard X-ray regime by using a deformable mirror [47], however the achieved focus was only one dimensional and its generation needed extensive intensity measurements in the focal plane and complicated *in-situ* wavefront-correction calculations

which prevents a simple implementation in standard microscopy setups.

2.3.2 Capillary optics

Another possibility to use total reflection for X-ray focusing is in capillary optics. This can be achieved by using polycapillary optics, also called Kumakhov optics [48], where a bunch of optical fibres is used to guide the X-rays into a focus by multiple reflections [49], or by using paraboloidally or ellipsoidally shaped single-bounce capillary optics, where focusing is achieved with a single grazing incidence reflection on the inner surface [50]. These optics can be used as condensers in full-field X-ray microscopes [51].

2.3.3 Refractive lenses

One of the first experiments that Röntgen performed when he started investigating X-rays, consisted in trying to focus X-rays with biconvex refractive lenses [1]. The reason why this approach was doomed to failure is the fact, that the index of refraction is below unity for all materials as mentioned in section 2.1. In consequence, lenses have to be concave in order to focus X-rays. In addition, due to the small deviation of the refractive index from unity, a series of lenses has to be used. An overview over refractive lenses for X-ray focusing is given in [4]. The idea of a refractive lens for X-rays was proposed and patented by T. Tomie in 1994 [52]. The first practical demonstration of compound refractive lenses (CRL) was however achieved by A. Snigirev *et al.* by drilling a line of holes [53] and later by cross drilling [54] into a block of solid aluminium, where a line focus of $8\,\mu$m and a spot focus of $8 \times 18\,\mu$m has been achieved. The focal length f of a stack of N lenses can be calculated as $\mathrm{f} = \frac{R}{2\delta N}$ where R is the radius of curvature and δ is the deviation of the real part of the refractive index from unity. To improve the optical performance of CRLs, rotational symmetric lenses have been developed, based on the impingement of a parabolically shaped tool into a thin aluminium or beryllium foil [55, 56]. The parabolic shape of the lens profile is necessary to avoid spherical aberration. Good imaging properties and a resolution in the $0.1\,\mu$m range have been demonstrated [57]. Other possibilities to fabricate compound refractive lenses are for instance reactive ion etching demonstrated by C. Schroer *et al.* [58, 59], deep X-ray lithography (LIGA process) pioneered at the Karlsruhe Institute of Technology [60, 61] or by putting air bubbles into an epoxy filled hollow glass capillary [62, 63, 64].

2.3.4 Fresnel zone plates

Experiments with diffractive optics in the form of Fresnel zone plates for visible light, date back to Lord Rayleigh in 1871 ([65] page 495). Further developments of FZPs were brought forward by J. L. Soret who reported in 1875 about his experiments with so-called binary or amplitude zone plates [66], which have completely opaque and transparent zones and R. W. Wood who, after the suggestion of Lord Rayleigh, developed the so-called phase zone plates in 1898 [67]. The idea of using FZPs for X-ray focusing has been presented and realized by Baez in 1952 [68, 69, 70, 71, 72].

A Fresnel zone plate is a circular diffraction grating which consists of concentric rings called zones (figure 2.8), where the period of the grating decreases with increasing radius [6]. In the case of the classical amplitude zone plate, the rings are alternately transparent

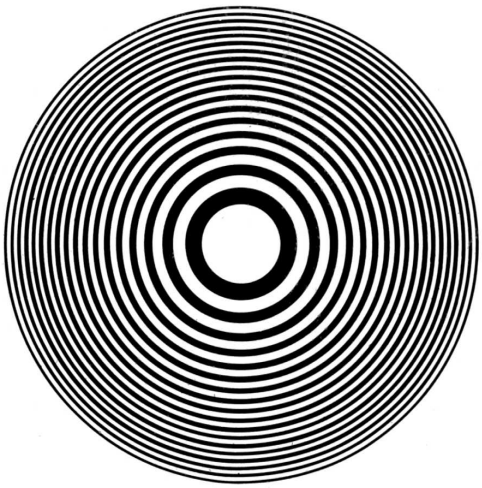

Figure 2.8: Schematic illustration of a binary zone plate with transparent (white) and opaque (black) rings.

and absorbing to the incoming light and are placed in such a way that the diffracted light interferes constructively at a point on the axis of rotation of the FZP, forming a focus. It has to be noticed that a zone plate in fact creates several foci, corresponding to different diffraction orders of the grating (FZP), where the first order focus, usually used for imaging, contains 10 % [6] (p. 348) of the incoming light. The multiple foci are depicted in figure 2.9 (image and following equations have been adopted from [6]). In the case of a phase zone plate, the materials of the zones are chosen to introduce a 180° phase shift to the incoming light which then interferes constructively at a point to form a focus of

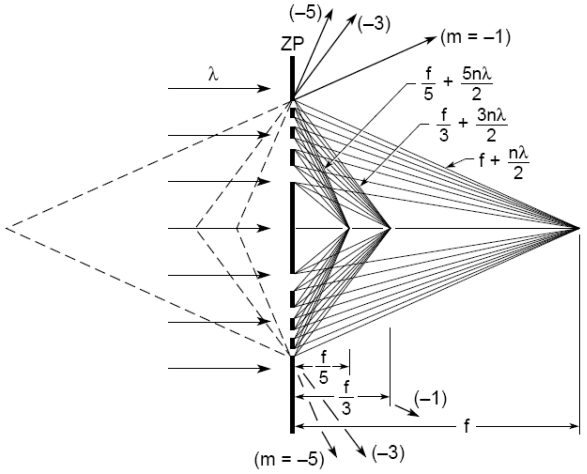

Figure 2.9: Schematic illustration of the different diffraction orders of a Fresnel zone plate. The third and the fifth orders are shown at $\frac{f}{3}$ and $\frac{f}{5}$, where f is the first order focal distance.

higher intensity than in the case of the amplitude FZP with 40 % [73] of the incoming light.

The radius of the consecutive zones is given by equation 2.9,

$$r_n^2 = n\lambda f + \frac{(n\lambda)^2}{4}, \tag{2.9}$$

where n is the index of the zone, ranging from 1 (innermost zone) to N (total number of zones). The second term $\left(\frac{(n\lambda)^2}{4}\right)$ represents the spherical aberration, which can be neglected if f$\gg \frac{n\lambda}{2}$. In this case, equation 2.9 can be simplified to (equation 2.10)

$$r_n = \sqrt{n\lambda f}. \tag{2.10}$$

The focal length of the zone plate is given by (equation 2.11):

$$f \simeq \frac{D\Delta r}{\lambda} \simeq \frac{4N(\Delta r)^2}{\lambda}, \tag{2.11}$$

which is valid if $\Delta r \ll r_N$, which is the case if the number of zones N is large and with D$\simeq 4N\Delta r$. As can be seen from the equations for the zone radii (2.9) and the focal length (2.11) zone plates are highly chromatic. To achieve diffraction limited resolution, the spectral bandwidth of the X-rays must be smaller than the inverse of the total number

of zones (equation 2.12):

$$\frac{\Delta\lambda}{\lambda} = \frac{\Delta E}{E} = \frac{1}{N}, \tag{2.12}$$

where E is the X-ray energy. The numerical aperture (NA), defined as $\mathrm{NA} \equiv \sin\theta$ where θ is the angle measured from the optical axis to the ray diffracted from the outermost zone, is given by (equation 2.13):

$$NA \simeq \frac{\lambda}{2\Delta r}. \tag{2.13}$$

The spatial resolution of a FZP can be quantified by the *Rayleigh resolution* criterion and is given by (equation 2.14):

$$\Delta r_{Rayl.} = \frac{0.610\lambda}{NA} = 1.22\Delta r, \tag{2.14}$$

where $\Delta r_{Rayl.}$ is the *Rayleigh resolution* and λ is the wavelength of the radiation. As can be seen from this equation, the resolution is comparable to the outermost zone width Δr, and higher resolutions can be achieved with fine outermost zones.

The depth of focus (Δz) of a zone plate is given by (equation 2.15):

$$\Delta z = \pm\frac{1}{2}\frac{\lambda}{(NA)^2} = \pm 2\frac{(\Delta r)^2}{\lambda}. \tag{2.15}$$

It is defined as the permitted distance, away from the focal or image plane, for which the intensity on axis is diminished by 20 %.

Calculation methods for diffraction efficiencies

Different methods exist to calculate the diffraction efficiencies of Fresnel zone plates. The essential difference among these is, if the zone plate is regarded as an optically thin or an optically thick grating. For optically thin gratings, the *Kirz*-theory can be applied. The extreme cases of this approach are the pure absorption and pure phase shifting zone plate. If the lens has to be treated as an optically thick grating, which is the case when the aspect ratio of the zone plate gets large, a more accurate model like the *rigorous coupled wave theory* (CWT) has to be applied.

Kirz theory Calculating diffraction efficiencies by regarding the lens as an optically thin grating has first been performed by J. Kirz in 1974 [73]. As all materials are characterized

by a complex refractive index of the form n = 1-δ-iβ as already shown in section 2.1[2], an X-ray wave, which passes through a material of thickness t, is attenuated and phase shifted. The amplitude is attenuated by $\exp^{-2\pi\beta t/\lambda}$ and the phase is shifted by $\phi = 2\pi t\delta/\lambda$ with respect to the open zones. A traditional FZP consists of absorbing/phase shifting zones and empty, non material filled zones. The wave amplitudes after passing through the empty zones (A_p) and the material filled zones (A_s) can be calculated by equation 2.16a and 2.16b [73]:

$$A_p = \frac{C}{2\pi}\int_0^{\pi} e^{i\theta}d\theta = \frac{iC}{\pi} \text{ and} \tag{2.16a}$$

$$A_s = \frac{C}{2\pi}e^{-2\pi\beta t/\lambda}\int_{\pi}^{2\pi} e^{i(\theta-\phi)}d\theta = -\frac{iC}{\pi}e^{-2\pi\beta t/\lambda}e^{-i\phi}, \tag{2.16b}$$

where θ is the phase change of the wave over the distance of one pair of zones and $C^2 = I_{inc}$ is the total incident flux on this zone pair. The intensity contribution to the image of this pair of zones is (equation 2.17) [73]:

$$I_1 = |A_p + A_s|^2 = \frac{C^2}{\pi^2}\left(1 + e^{-4\pi kt/\lambda} - 2e^{-2\pi kt/\lambda}\cos\phi\right). \tag{2.17}$$

If this equation is expanded to a general expression where the diffraction order m is introduced one obtains (equation 2.18) [73]:

$$I_m = \begin{cases} 0 \text{ or } \frac{1}{4}, & m = 0 \\ \frac{C^2}{m^2\pi^2}\left(1 + e^{-4\pi kt/\lambda} - 2e^{-2\pi kt/\lambda}\cos\phi\right), & m \text{ odd} \\ 0, & m \text{ even.} \end{cases} \tag{2.18}$$

Equation 2.18 takes absorption and phase shift into account. The value of I_m for m = 0 is depending on which of the extreme cases with just one contribution is regarded. If $\beta \to \infty$, absorption is dominant and the efficiency of the a binary amplitude or *Soret* zone plate is obtained. In this simplest case, of completely transparent and opaque zones, the

[2]Here with the convention of Kirz, using a negative sign for the imaginary part of the refractive index.

diffraction efficiency can be calculated by (equation 2.19):

$$\eta_m = \begin{cases} \frac{1}{4} & m = 0 \\ \frac{1}{m^2\pi^2} & m \text{ odd} \\ 0 & m \text{ even.} \end{cases} \tag{2.19}$$

where, η_m is the diffraction efficiency and m is the diffraction order. Here, 50 % of the incoming radiation is absorbed by the opaque zones, 25 % are transmitted undiffracted and $\frac{1}{m^2\pi^2}$ % is diffracted into the odd orders m (m = ±1, ±3, ±5,...), which leads to approx. 10 % for the first and approx. 1 % for the third order, respectively.

In the other extreme case of $\beta \to 0$ and $\phi = \pi$, absorption is negligible and the result of a *Reileigh-Wood* or pure phase zone plate is obtained, where the opaque zones are replaced with zones that lead to a π phase shift of the incoming radiation without absorption. The efficiency can be increased by a factor of 4, compared to the binary zone plate, leading to (equation 2.20):

$$\eta_m = \begin{cases} 0 & m = 0 \\ \frac{4}{m^2\pi^2} & m \text{ odd} \\ 0 & m \text{ even.} \end{cases} \tag{2.20}$$

Here, no radiation is absorbed and no radiation stays undiffracted. This leads to efficiencies of approx. 40 % for the first and approx. 4.5 % for the third order, respectively.

The original concept by Kirz only treats zone plates which consist of open zones and zones filled with one material. If both zones are filled with different materials it needs to be extended. This has been done by W. Yun *et al.* [74]. For two materials with the complex refractive index $n_i = 1\text{-}\delta_i\text{-}i\beta_i$ with i = 1,2 for material 1 and 2, respectively, one obtains (equation 2.21):

$$\eta_m = \begin{cases} \frac{1}{4}\left(\gamma_1^2 + \gamma_2^2 - 2\gamma_1\gamma_2 \cos\left[2\pi d\left(\delta_2 - \delta_1\right)/\lambda\right]\right), & \text{m=0} \\ \left(\gamma_1^2 + \gamma_2^2 - 2\gamma_1\gamma_2 \cos\left[2\pi d\left(\delta_2 - \delta_1\right)/\lambda\right]\right) / \left(m\pi\right)^2, & \text{m=odd} \\ 0, & \text{m=even,} \end{cases} \tag{2.21}$$

where $\gamma_i = \exp(-2\pi d\beta_i/\lambda)$. With this equation it is possible to calculate the diffraction

efficiency of a zone plate consisting of any possible material combination as a function of its thickness. All results of chapter 4 referred to as calculated with the "*Kirz*-theory" were calculated with equation 2.21 .

Coupled wave theory If the aspect ratio (zone height to zone width) of a FZP becomes large, the thin grating approximation is no longer valid. For these optically thick gratings other models have to be applied to describe their diffraction behaviour accurately. One possibility is the so called *rigorous coupled wave theory* (CWT), which has been applied to zone plates by J. Maser and G. Schmahl in 1992 [75]. The theory indicates that if the zones remain parallel to the optical axis in an optically thick grating (large aspect ratio), the diffraction efficiency is reduced to very poor values. Therefore the zones of a zone plate which have to be regarded as an optically thick grating have to be tilted towards the optical axis. Only if the Bragg-condition is fulfilled between the incoming wave and the zones of the zone plate, a high diffraction efficiency is obtained.

In 1997 G. Schneider has extended the theory with the diffraction into higher diffraction orders and has calculated the influence of variable line to space ratios on the diffraction behaviour [76]. In addition he regarded the influence of roughness and interdiffusion on the diffraction efficiency [77], which is especially important for multilayer zone plates. The CWT is the basis for the ZPTGW-program (version march 2001) which has been used to obtain the results presented in chapter 4, which are referred to as calculated with the CWT.

2.4 Fresnel zone plate fabrication

In this section, a review of different methods which have been employed for the fabrication of Fresnel zone plates is presented. The general challenge in zone plate manufacturing is the creation of dense structures of very fine features, to achieve high resolution (equation 2.14). In general, two different alternatives are used to create the zone structures: 1^{st} structuring a homogeneous material or 2^{nd} building up layers of materials with very different refractive indices. In very early approaches, FZPs were made by drawing concentric ring patterns and making reduced photographic reproductions of them [66], or by mechanically producing free standing metal zone plates [71]. Due to the limits in achievable feature

sizes, optical methods like holography[3] were applied [78]. FZPs made with this technique suffered from spherical aberration due to the large difference in wavelength of the laser they were produced with and the X-rays they were designed for. Therefore, other structuring methods which are capable to produce finer features had to be found. As an outgrowth of techniques developed for the semiconductor industry [79], electron beam lithography (EBL) has been suggested by D. Sayre in 1972 [80], and emerged as the most popular structuring technique for zone plates to date. Other surface structuring methods include X-ray lithography [81], nanoimprint lithography [82] and focused ion beam [83]. Techniques involving EBL and FZP manufacturing techniques involving multilayer deposition, will be treated in more detail in the following.

Lithography based techniques

First practical results in applying EBL for FZP manufacturing were reported by D. Shaver *et al.* [84] and D. Kern *et al.* [85], where zone widths in the range of 100 nm could be achieved. They also introduced Si_3N_4-membranes as carriers for zone plates and specimens, which are still widely used in the the X-ray microscopy community. Three of the main processes of fabrication are: the single layer, the double layer and the trilayer process, combined with deep etching.

The single layer process, is depicted in figure 2.10 (adopted from [6]) and details about the process are given in appendix A. In this process, a substrate is coated with an electron sensitive resist, which is then structured and developed. After the development, the created structures are filled by electroplating. Outer zone widths of $\Delta r = 20\text{-}40$ nm can be achieved with maximum aspect ratios (ratio of zone height to zone width) of $3:1$ or $4:1$ [6]. These low aspect ratios are a drawback of this technique, especially for zone plates dedicated to higher photon energies, where high aspect ratios are required.

Some improvement can be achieved with the double layer process [86] (details are given in appendix A). Sub 30 nm lines and spaces and aspect ratios of $6:1$ [87] have been produced with this technique, which is an improvement compared to the single layer process but can still be too low for high energy X-rays.

Multilayer processes have been introduced and are used to achieve higher aspect ratio

[3]Using lasers from the visible to the UV spectral range.

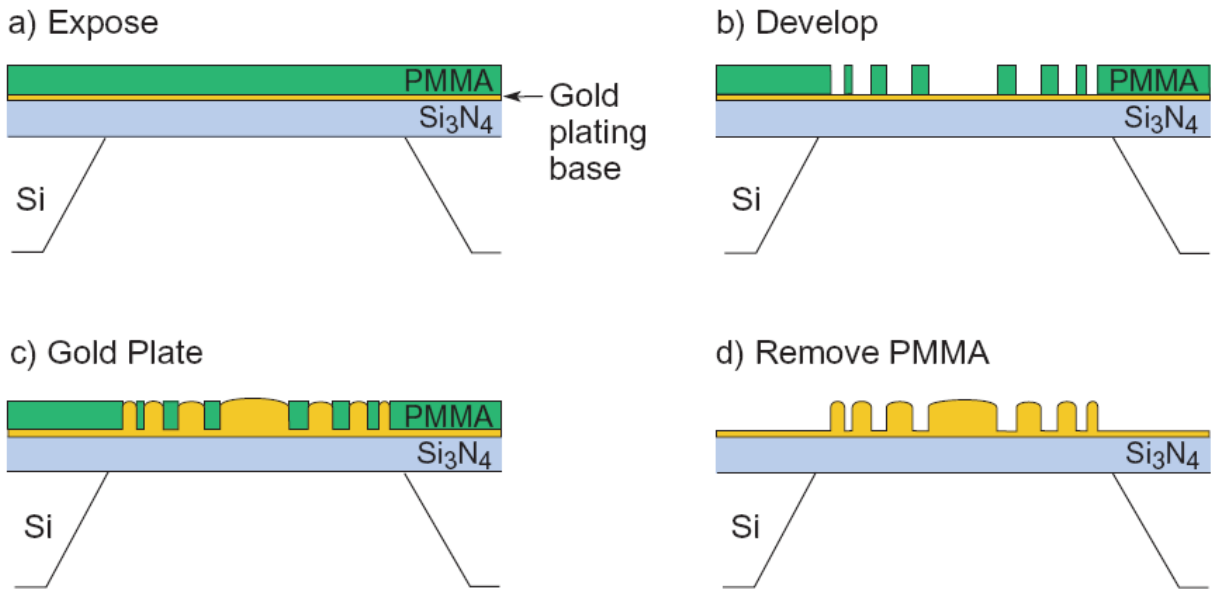

Figure 2.10: Schematic illustration of the single layer process for zone plate fabrication. The fabrication steps are: a) Expose, b) Develop, c) Gold Plate and d) Remove PMMA.

structures. Here, an additional metal layer (typically titanium) is deposited between the hard baked polymer and the electron sensitive resist and serves as a hard mask for a second etching step. Structure sizes of 20 nm with aspect ratios of nearly 9 : 1 have been achieved [88, 89, 90]. This trilayer process is, with slight modifications, also followed by other groups [91] who use higher order imaging [92] and introduced the stacking of zone to increase the aspect ratio [93, 94, 95]. To avoid the plating step, the polymer can be replaced with another material like germanium [96] ($\Delta r = 30\,nm$, aspect ratio 10 : 1) or a high absorbing metal layer (e.g. tungsten) [97, 98, 99]. Tungsten zone plates with structure sizes of 30 nm and aspect ratios of 5 : 1 (for $\Delta r = 30\,nm$) up to 15 : 1 (for $\Delta r = 200\,nm$) are commercially available. A decrease of the achievable zone width for single exposure electron beam lithography, is accomplished by cold development treatments [100], where zone plates with 13 nm outer zone width with aspect ratios of 2.7 : 1 [101] have been obtained. All of the aforementioned processes share several problems which can be summarized as the imitations in zone widths for lithography based approaches due to beam size limitations and scattering effects in the resist, the aspect ratio which is limited to maximal 10 : 1 (for $\Delta r \leq 30\,nm$) and the necessity to increase the outer zone width if higher aspect ratios are desired.

To circumvent these drawbacks, special processes like the “double patterning” tech-

nique have been developed. In this approach, even and odd zones are made in consecutive steps [102] and resolutions of 15 to 12 nm [103] with aspect rations of 5 : 1 to 2.5 : 1 were achieved. The "zone-doubling" technique, where a lithographically structured template with sparsely distributed zones made from a low refractive index material is coated with a high refractive index material in an atomic layer deposition process [104] has allowed a resolution of 9 nm [8] with an aspect ratio of 15 : 1 for 12.5 nm-wide structures. Very recently this kind of FZPs have been used to resolve sub-20 nm lines and spaces in the hard X-ray regime at 6.2 keV [105].

Multilayer based techniques

The second basic approach for FZP manufacturing beside EBL are multilayer based methods known as "sputter-sliced" or "sliced jelly roll" technique. A schematic illustration of this preparation method is given in figure 2.11 (adopted from [106]). The basic idea is to

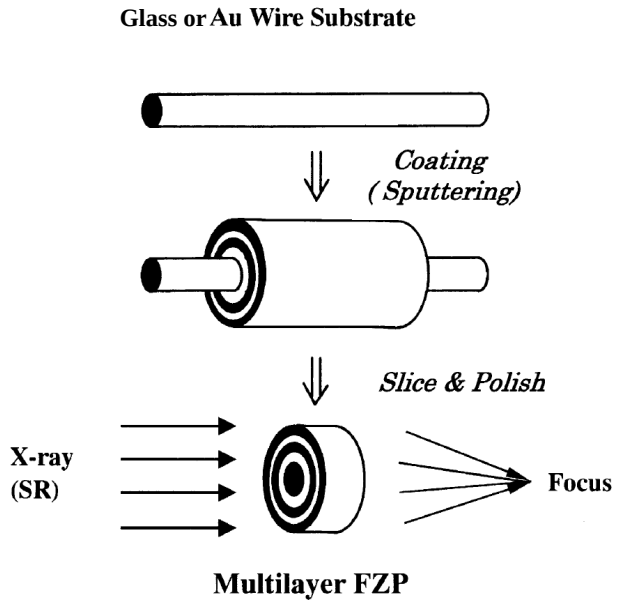

Figure 2.11: Schematic illustration of the "sputter-sliced" technique: A wire is coated with a multilayer by sputtering and is sliced and polished to form a zone plate.

deposit two different materials, one very absorbing, the other "as-transparent-as-possible" onto a wire which is rotating around its longitudinal axis during the deposition, followed by sectioning and thinning the wire to form the zone plate. First results of this approach with evaporation where presented in 1980 [9]. Subsequent experiments were performed

with ion sputtering [107]. For further experiments, the deposition technique was changed to magnetron sputtering and the substrates to glass wires [108]. Minimum outer zone widths of 17 nm and thicknesses down to 3-4 μm could be achieved with dimpling and ion milling. Because of these large minimal thicknesses, the scope of the multilayer zone plates concentrated on hard X-ray focusing [109]. Due to the low zone quality and the non optimal thickness for the applied energies of 4.1 and 18.6 keV [110], none of these zone plates could produce a diffraction limited spot with a size comparable to the outer zone width. Furthermore, no images could be obtained with these zone plates applied as X-ray lenses.

Groups from Japan also contributed to the field of sputter-sliced zone plates [111, 112]. They concentrated their work on focusing high energy beams [113, 114, 115, 116], developing further the sputtering apparatus to improve the quality of the layers [117, 118] and producing so called kinoform style zone plates which show high efficiencies due to a gradually varying refractive index [119, 120, 121, 122]. Nevertheless, the layer quality [123] and hence the imaging capabilities [124, 125] of multilayer zone plates based on sputtering stay rather poor.

As an alternative to sputtering, the surface plasma chemical vapour deposition (SPCVD) technique has also been used to fabricate multilayer zone plates [126, 127]. Also in this case the focusing capabilities of the lens are reduced due to imperfections in the zone plate structure.

Like the lithography based techniques, all processes based on multilayer deposition on cylindrical substrates share several problems which include corrugated interfaces, accumulated interface roughness during the deposition of thick multilayer sequences, a lower limit of the zone plate thickness of approx. 3 μm if mechanical sectioning and thinning techniques are used and the very limited focusing and imaging capabilities. Despite their wide range of attainable aspect ratios, they are very difficult to prepare for the soft X-ray regime.

As alternative, multilayer zone plates on planar substrates, known as multilayer Laue lenses (MLL), have been introduced [128, 129]. A schematic illustration is given in figure 2.12 (adopted from [130]). The advantage claimed for this technique is that the thinnest layers which require the highest precision are deposited first and therefore do not suffer from

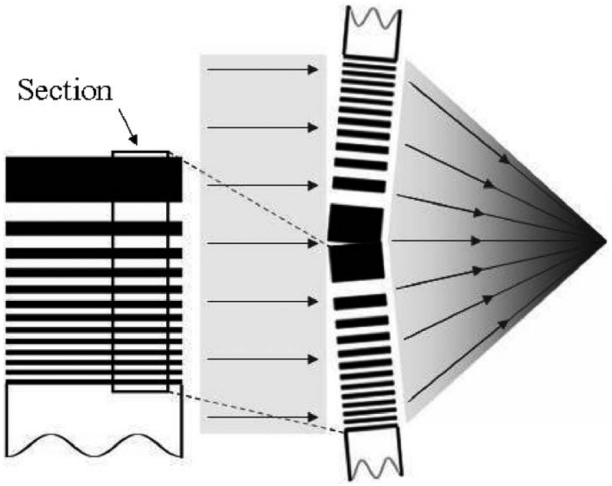

Figure 2.12: Schematic illustration of a multilayer Laue lens. A thin film sequence, obeying the zone plate design rule is deposited onto a Si-substrate. The multilayer is sectioned, and two pieces of the zone structure are used to form a linear focus.

roughness accumulation. After the sputter process the multilayer structure is sandwiched face to face and thinned to a wedge with mechanical techniques to a thickness of 5-25 μm [131]. With finest layer thicknesses of 5 nm a linear focus of 16 nm could be obtained [130]. Recently MLLs have been prepared by a combination of pulsed laser deposition (PLD) and focused ion beam (FIB) preparation [132]. The resolution of these MLLs of 180 nm was however far lower than the design value of 50 nm.

Chapter 3

Experimental methods

In the first part of this chapter, the fundamentals of atomic layer deposition are explained, and the Picosun SUNALE^{TM} R100 ALD reactor which has been used for the preparations is presented. In the second part, the Nova Nanolab 600 DualBeam^{TM} instrument is presented. In the last part the setups which have been used to investigate the zone plates at BESSY II and at the ESRF are presented.

3.1 Atomic layer deposition

The technique of atomic layer deposition has been developed by T. Suntola and S. Lindfors in the mid 1970s in Finland, and has first been introduced by the name of atomic layer epitaxy (ALE) [133]. A driving force for the development of ALD was the production of thin film electroluminescent (TFEL) flat panel displays, with epitaxially grown manganese doped zinc sulfide [134, 135, 136].

3.1.1 Fundamentals

ALD deposition

The ALD technique is a particular form of chemical vapour deposition (CVD) [10]. An extended overview of ALD is given in [137]. While in conventional CVD, the precursors are continuously fed into the reaction chamber, in ALD the different precursors are introduced sequentially into the reaction chamber and the growth takes place on the surface of the substrate in a self limiting manner. To illustrate the ALD process, the

deposition of TiO_2 is described below (figure 3.1). For this process, $TiCl_4$ and H_2O are used as precursors. Two possible surface conditions of the substrate and of the growing

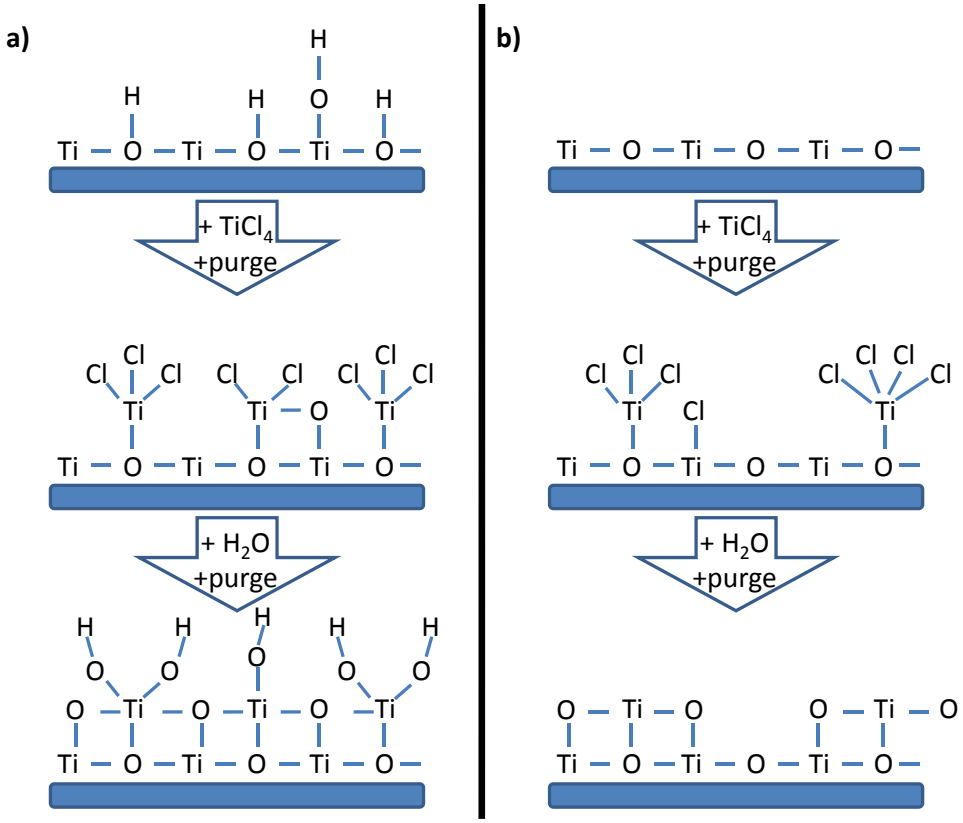

Figure 3.1: Schematic illustration of the ALD process for the growth of a TiO_2. The surface of the substrate and hence the growing film is shown in two possible states during the deposition: in a) the surface is hydroxyl group terminated, in b) the surface is dehydroxylated. A complete cycle is divided into precursor pulses and purges.

film may be encountered, leading to two different types of surface reactions. In the case of a hydroxyl group terminated surface (figure 3.1 a)), $TiCl_4$ reacts with the surface by releasing some of its ligands. If the surface is completely dehydroxylated (figure 3.1 b)), $TiCl_4$ undergoes chemisorption in a dissociative or intact way. The degree of hydroxyl group coverage depends on the substrate temperature and on the exposure to water, which is often used as an oxygen source in metal oxide deposition. For both surface conditions, the exposure of the substrate to a first $TiCl_4$-pulse and the purge of the reaction chamber from unabsorbed precursor and ligands, leads to the formation of a chemisorbed layer, where only the molecules which are covalently bond to the surface stay on the substrate. Depending on the type of reactor, the purge can either be a pulse of inert gas or the

evacuation of the chamber. Following the first purge, the oxidant, in this case H_2O, is introduced into the chamber and reacts with the chemisorbed layer, forming a solid film of TiO_2, and restoring the surface to its original state (either hydroxyl terminated or dehyroxylated). The ALD cycle is completed by a second purge that cleans the chamber from reaction by-products and nonreacted precursor. The whole cycle is then repeated until the desired film thickness is achieved.

In the ideal case, a full atomic monolayer is deposited at each ALD cycle and allows a very accurate thickness control, an excellent conformality and sharp interfaces. Derivations from this ideal ALD growth mechanism may be due to incomplete coverage of the surface with functional groups or to steric hindrance by using bulky ligands, but this does not affect the self limiting growth characteristic of ALD as long as all reactions of the precursors with the substrate and the purge cycle have been completed.

A very important parameter in ALD is the substrate temperature. The ideal temperature range for a surface controlled growth is called the "ALD window" (figure 3.2). For the deposition of multilayers, where different materials have to be deposited, the "ALD window" of the different materials have to overlap. In the case of Al_2O_3 and Ta_2O_5, the ALD windows of both materials overlap between 150 and 275°C. At temperatures below the optimal range, an increase of the deposition rate may be observed if multilayer absorption and condensation of the precursor on the substrate occurs (physisorption); a decrease of the growth rate is more often observed, and occurs if the reaction processes are kinetically hindered and the reactions become too slow to be completed during the precursor pulse. This problem could be reduced by an increase in the pulse time, but as a consequence the increased cycle time would reduce the productiveness of the process. Above the ALD window, an increase of the growth rate is observed if the precursor thermally decomposes and a decrease occurs if the precursor desorpts from the substrate.

Besides the deposition temperature, precursor flux, pulse and purge times significantly influence the growth characteristics of the film. Precursor flux and pulse times are optimized to achieve complete saturation of the surface with precursor molecules and hence a nearly saturated growth rate ($\geq 90\,\%$). To accomplish a 100 % saturated growth rate would often result in impractically long pulse times, without any additional benefits for film properties like uniformity, confromality and purity. Unnecessarily long pulse

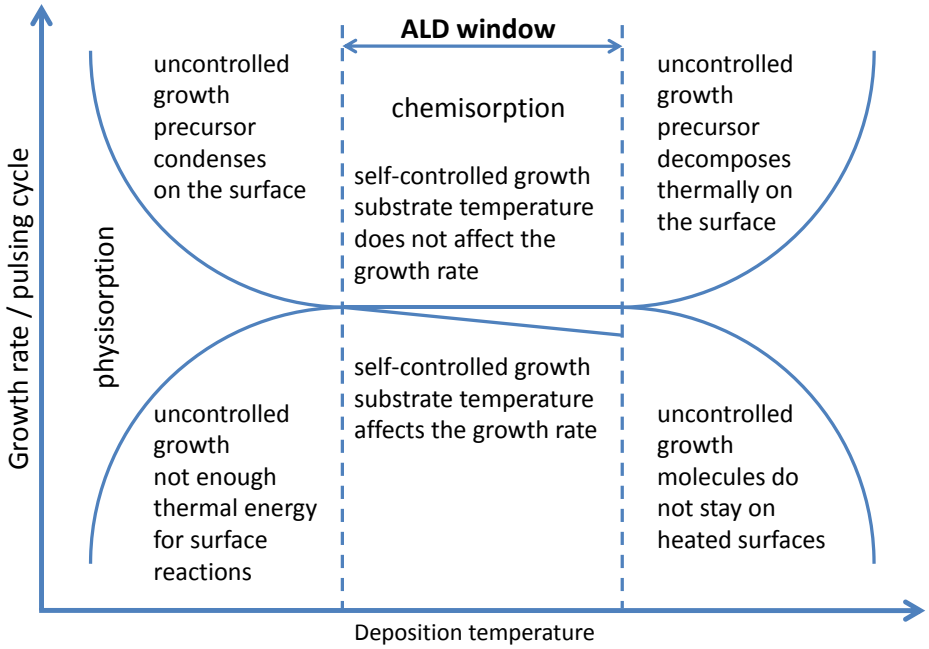

Figure 3.2: Schematic illustration of the ALD window. Only in the center part, the growth proceeds in a self limiting way. If the deposition temperature is too high or too low the growth rate becomes nonlinear.

times or high precursor fluxes decrease the productiveness of the process also in terms of precursor consumption and the need for long purge times. The purge times, which are very reactor dependent, are optimized to completely separate the precursor pulses and hence avoid CVD-like growth. Excessive purging is again detrimental to the productiveness of the process in terms of long cycle times and can promote surface reactions that diminish the amount of absorbed precursor or reactive sites on the surface.

A large variety of materials with lots of different precursors can be deposited with ALD [137]. The most prominent material classes are oxides, nitrides, sulfides, flourides and pure metals. For this thesis, multilayers of Al_2O_3 and Ta_2O_5 have been prepared with Trimethylaluminium (TMA; $Al(CH_3)_3$) and Tantalum(V)ethoxide ($Ta(OEt)_5$) as precursors, and H_2O_2 as an oxidant. The reaction mechanism leading to the formation of Al_2O_3 has been intensively studied and reviewed [138]. The overall reaction can be written as

(equation 3.1):

$$Al(CH_3)_3(g) + \frac{3}{2}H_2O(g) \longrightarrow \frac{1}{2}Al_2O_3(s) + 3CH_4(g). \tag{3.1}$$

If the reaction occurs at –OH groups on the surface, the subreactions can be written as (equation 3.2a and 3.2b):

$$\| - OH + Al(CH_3)_3(g) \longrightarrow \| - O - Al(CH_3)_2 + CH_4(g), \tag{3.2a}$$
$$\| - Al - CH_3 + H_2O(g) \longrightarrow \| - Al - OH + CH_4(g). \tag{3.2b}$$

The reaction mechanism of the deposition process of Ta_2O_5 has been presented by K. Kukli *et al.* [139], where the overall reaction is (equation 3.3):

$$2Ta(OCH_2CH_3)_5(g) + 5H_2O(g) \longrightarrow Ta_2O_5(s) + 10CH_3CH_2OH(g). \tag{3.3}$$

For a reaction at –OH groups on the surface, the subreactions can be written as (equation 3.4a and 3.4b):

$$\| - OH + Ta(OCH_2CH_3)_5(g) \longrightarrow \| - O - Ta(OCH_2CH_3)_4 + CH_3CH_2OH, \tag{3.4a}$$
$$\| - Ta(OCH_2CH_3)_4 + 4H_2O(g) \longrightarrow \| - Ta - (OH)_4 + 4CH_3CH_2OH(g), \tag{3.4b}$$

whereas the vertical lines represent the surface for all reactions. For this thesis, H_2O_2 (30 % in aqueous solution) instead of H_2O has been used, which led to a better uniformity of the films.

ALD reactor types

ALD reactors are distinguished by their working pressure. The two main types of reactors are the high- (or ultrahigh-) vacuum reactors which work in molecular flow conditions and the inert gas flow reactors which work in viscous flow conditions.

In the (U)HV-type, the reaction chamber is evacuated to the (U)HV-range in-between pulses which leads to long purge times and hence a low productiveness. Furthermore, these reactors show a lower precursor utilization efficiency which makes them non attractive, especially for production purposes.

In the flow type (base pressure 1–10 Torr), a constant inert gas flow is applied. During the pulses, the precursors are injected into this inert gas stream and directed into the reaction chamber. For purging the inert gas alone flushes away the residue precursor molecules and reaction by products. The flow type reactors allow much shorter purge times than the high- (or ultrahigh-) vacuum type reactors. In addition they show an increased precursor utilization efficiency, because the precursor molecules make multiple hits with the substrate when they are being transported through the reactor, which increases their reaction probability. Due to these inherent benefits, all commercially available ALD reactors are of the flow type.

3.1.2 The Picosun SUNALE^{TM} R100 ALD-device

All depositions for this thesis were carried out in collaboration with the BMBF[1] research group "functional 3D-nanostructures by atomic layer deposition" at the Max-Planck-Institute of Microstructure Physics at Halle (Saale), using their commercial Picosun SUNALE^{TM} R100 ALD device. Being a multi-purpose device, the reactor is of the hot-wall top-flow type, with a dual chamber design. A schematic illustration of the main parts of the reactor is given in figure 3.3. A constant inert gas flow of 200 sccm of nitrogen is used for each source which is connected to the reaction chamber via a separate gas line. In addition the reaction chamber is fed with a constant inert gas flow of 200 sccm. In the configuration used for this study, the rector is equipped with 3 sources for liquid precursors. Only two of them are shown in the schematic illustration. The TMA and H_2O_2 source are kept at room temperature, which is high enough for these liquids to develop a sufficient vapour pressure to allow efficient dosing. On the contrary, the $Ta(OEt)_5$ has to be kept at approximately 120°C to ensure a high vapour pressure. This source is designed as bubbler, where the nitrogen is led through the source container during pulsing. All sources are equipped with *Swagelok* diaphragm valves for precise dosing and short pulse times. The reactor itself can be heated up to 500°C, whereas for this application a temperature of 250°C has been used. At this temperature, the ALD windows for both materials overlap, so that multilayers can be deposited. The wall of the reaction chamber is kept hot to avoid precursor condensation. The outlet of the reaction chamber is connected to a vacuum pump which brings the reactor to its base pressure in the fine vacuum range (below 1 mbar), assures for a continuous flow and absorbs all gaseous components which leave the chamber.

[1] German: Bundesministerium für Bildung und Forschung

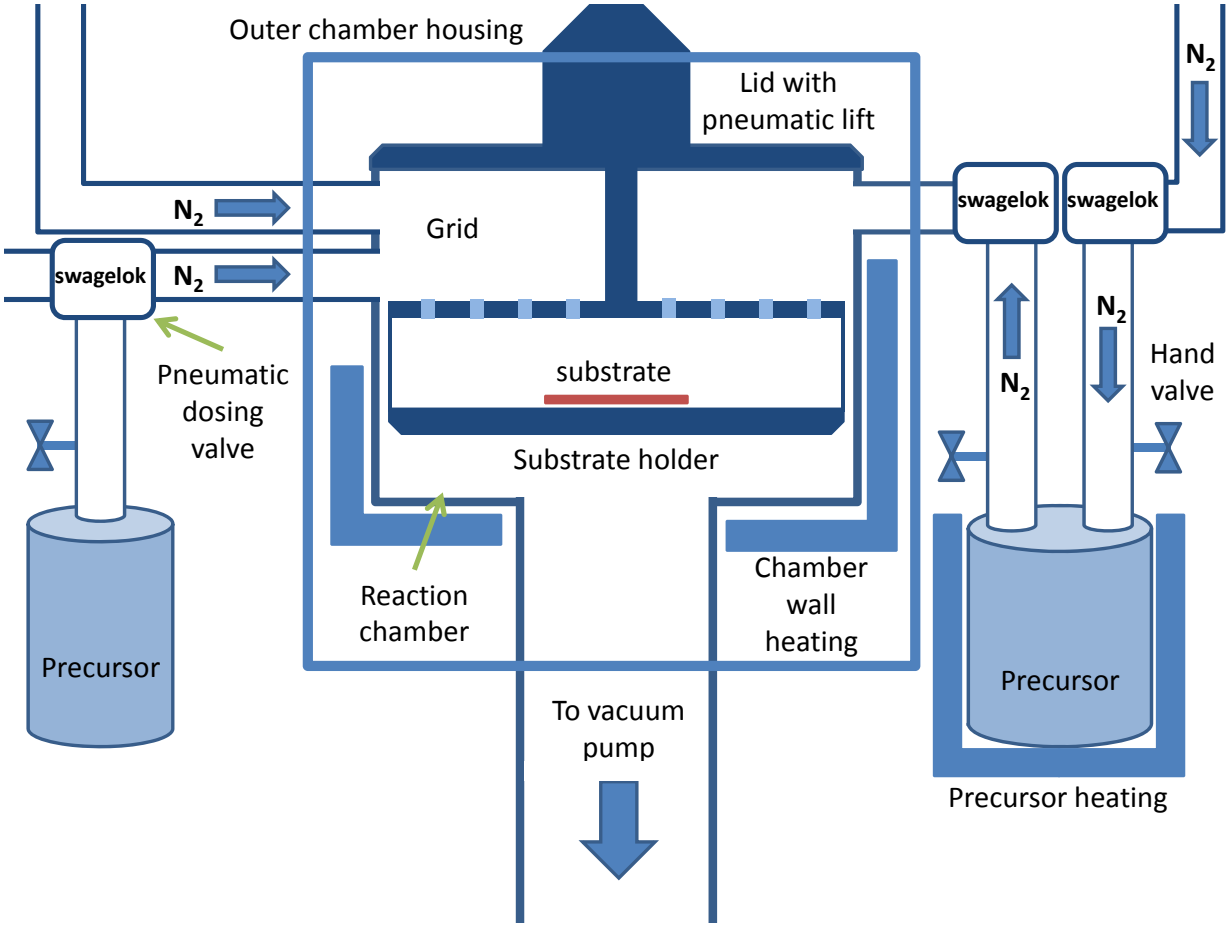

Figure 3.3: Schematic illustration of the Picosun SUNALE R100 ALD device. The image shows two precursor sources, one at room temperature, the other as a heated source (bubbler). Both sources are connected to the reaction chamber with separated lines which are constantly fed with nitrogen and into which the precursors are injected. The walls of the reactor are heated to avoid precursor condensation. The reactor contains a gird to homogeneously distribute the gas and a suspended substrate holder. All reaction products are dragged into a vacuum pump.

3.2 The FEI Nova NanoLab 600 DualBeam^{TM}

The Fresnel zone plates for this thesis were sectioned from the coated fibres with focused ion beam in a combined SEM/FIB instrument, the FEI Nova NanoLab 600 DUALBEAM^{TM}. Its features, together with the basic principles of SEM and FIB are described in the following.

In a DualBeam^{TM} system, a FIB is implemented for milling the material, while the imaging is conducted with a SEM. Both columns are mounted at an angle of 52° with respect to each other, with the SEM being vertical, as shown schematically in figure 3.4. In a scanning electron microscope, electrons are generally generated in an electron

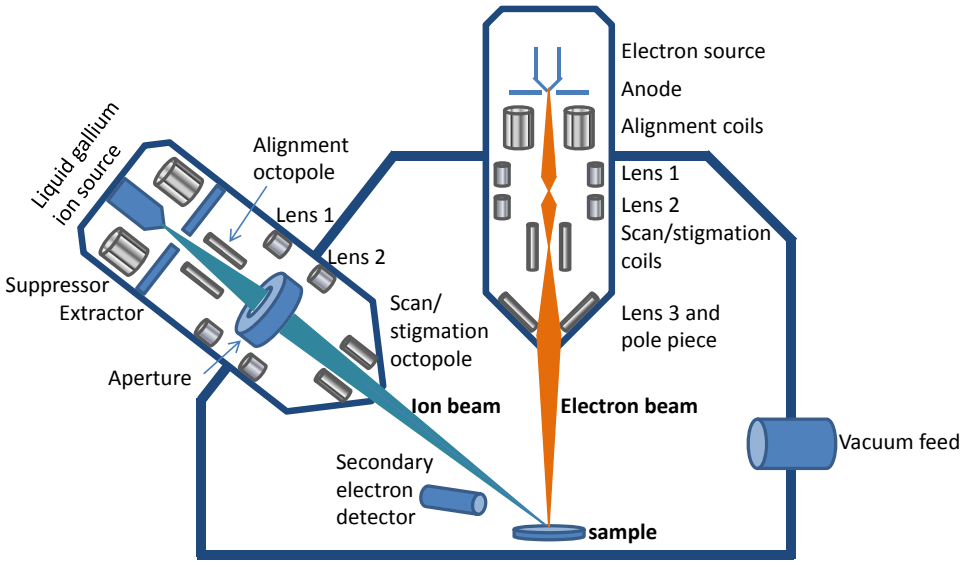

Figure 3.4: Schematic illustration of a DualBeam^{TM} instrument. The SEM column is mounted vertically and used for imaging, while the FIB column is mounted at an angle of 52° to the vertical and used for material milling.

gun, either by thermal emission from a tungsten filament or from a LaB_6-crystal or by field emission from a tungsten single crystal (cold emission) or a zirconium oxide crystal (thermally assisted or Schottky emission) and accelerated to a typical energy range of 0.5 to 40 keV. To achieve a narrow beam with a diameter of typically 0.4 - 5 nm, the electrons

pass one or more condenser lenses, before the beam is raster scanned over a rectangular area on the sample surface by pairs of scanning coils or deflector plates, typically situated in the final lens of the electron column. When the electrons impact the surface they create secondary and backscattered electrons as well as characteristic X-rays, which are recorded by different detectors and displayed on a computer monitor. The most basic detector for secondary electrons is the *Everhart-Thornley*-detector, which consists of a scintillator inside a Faraday-cage and a photomultiplier. The magnification of the SEM is defined as the ratio of the area of the displaying monitor to the area on the sample surface which has been scanned by the beam. Typical magnifications can range from some tens to several hundred thousand. To avoid scattering of the electrons with residue gas atoms and the contamination of the sample surface, the electron column is kept under UHV and the specimen chamber under high vacuum condition.

A focused ion beam instrument is generally used to alter the surface of a sample, either by milling patterns or by depositing layers with ion beam enhanced deposition. To achieve efficient milling, heavier particles than electrons are needed: most FIB instruments are equipped with liquid metal ion sources (LMIS), usually gallium sources, where the gallium (metal) is put into contact with a tungsten filament, which is heated to temperatures above 30 °C which causes the gallium to melt and wet a needle. At the tip of the needle a very large electric field $\left(>10^8 \frac{V}{cm^2}\right)$ is applied to ionize the gallium and cause field emission of Ga^+ ions. The ions are accelerated to energies of typically 5 - 50 keV, the beam is focused to a diameter of a few nanometers and raster scanned over the surface. An extended overview over ion column design and properties is given in [140]. The milling yield is dependant on the accelerating voltage as well as the current, delivered by the ions to the sample, which is on the order of tens of pico amperes to tens of nano amperes. In addition to milling, the incoming ions produce secondary electrons and ions which can be detected in a similar way as in the SEM and used for imaging. Similar to the SEM, column and specimen chamber have to be kept at UHV and high vacuum conditions, respectively.

The particular instrument used for the preparations described in this thesis, consists of a high-resolution SIRION^{TM} SEM column with a Schottky type thermal field emission electron source and a MAGNUM^{TM} ion column with a gallium (Ga^+) liquid metal ion source. The range of accelerating voltages for the SEM is 200 V to 30 kV and a probe

current of ≤ 20 nA is adjustable in 21 steps. The ion source operates in an acceleration voltage range of 5 to 30 kV and presents probe currents of 1 pA to 20 nA adjustable in 15 steps. The system offers several types of detectors. The basic detector for low resolution imaging is a *Everhart-Thornley* secondary electron detector. For high resolution imaging, an in-lens detector for both, secondary and backscattered electrons is installed: With the SEM a resolution down to 1.1 nm and with the FIB a resolution down to 7 nm can be achieved. For the patterning of specimens, a digital patterning generator allows a resolution of 4000 x 4000 pixels and a total of 1 million addressable pixels. The dwell time per pixels can be adjusted from 100 ns to 4 ms. With the ion beam, structures as fine as 15 nm can be milled and TEM samples with a thickness down to 50 nm can be prepared. For layer deposition, the system is equipped with gas injection systems (GIS); in our case platinum has been deposited with Trimethyl-Methylcyclopentadienyl-Platinum ($C_9H_{16}Pt$) as precursor. Structures as fine as 20 and 50 nm can be deposited with electron and ion beam enhanced deposition, respectively. For the transfer of specimens the DualBeam^{TM} contains a micromanipulator (*Omniprobe*) equipped with very fine tungsten needle.

3.3 X-ray optical experiments

3.3.1 The scanning X-ray microscope MAXYMUS

The FZP has been characterized and used as a lens in the FZP based scanning soft X-ray microscope MAXYMUS at BESSY II in the soft X-ray range. It is based on the principle of an interferometrically controlled STXM developed by T. Tyliszczak and colleagues at the ALS [141]. A further development of this instrument has been installed at the SLS [142]. This instrument and MAXYMUS have both been constructed and built by Bruker EST (former ACCEL company). The instrument at BESSY II has been installed at beamline UE46_PGM2 [143] in 2009. A detailed description of this instrument is found in [144]. Photographs of different relevant parts of the microscope are shown in figure 3.5. The microscope is mounted on an assembly of girder movers on which the socket of the microscope, an artificial granite block, is placed (figure 3.5 a)). The girder movers allow the alignment of the whole microscope in the beam axis with 5 degrees of freedom, and minimize the influence of vibrations. A laser interferometer system assures for high positional accuracy and reproducibility when the microscope is operated in active feedback mode. Two interferometers, one for the X- and one for the Y-axis, detect differential motion of the sample and FZP piezo stages with up to 10 kHz sampling rate. For both axes this signal is fed

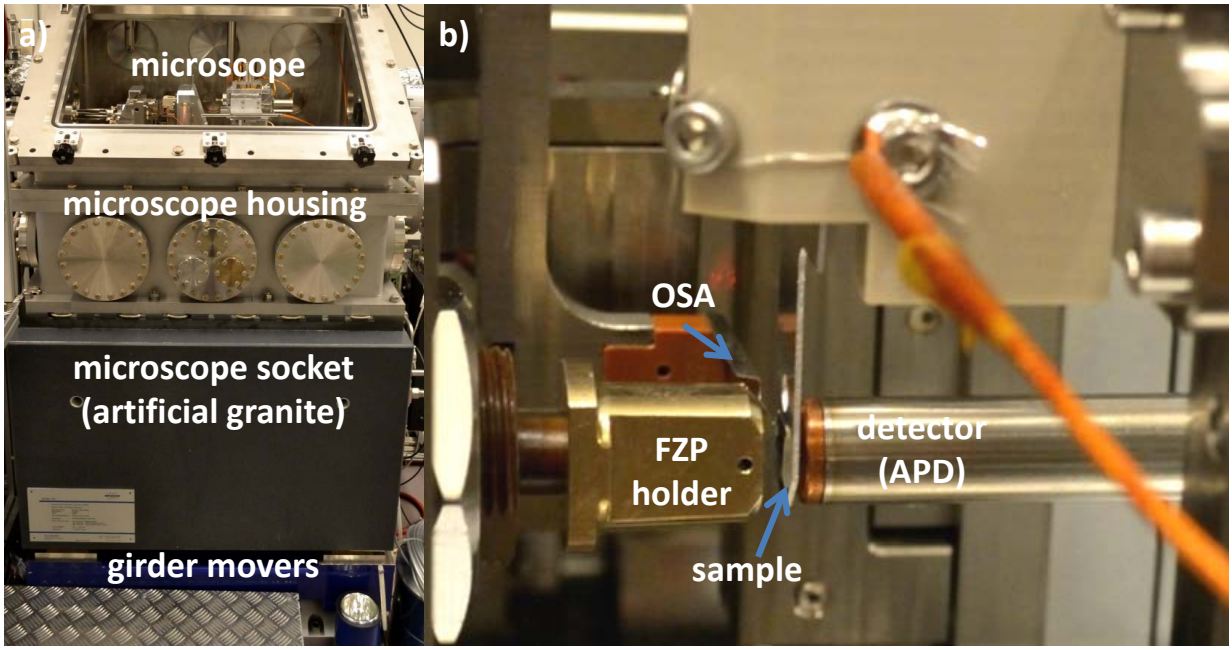

Figure 3.5: Photographs of the SXM MAXYMUS at BESSY II, Berlin. a) Shows an overview of the microscope housing with its mounting on an assembly of girder movers and an artificial granite block. b) Shows a close up view of the zone plate, the OSA, the sample and the detector.

into a PID[2] loop on the interferometer controller card, which sends a correction output signal back to the stages. This operation is suited to correct for drifts and to suppress low frequency vibrations. The resolution of the interferometer is less than 1 nm which makes the microscope suitable for very high resolution optics and spectroscopic studies. As the microscope is operated at an undulator, the generally high photon flux allows short dwell times. In addition, the plane grating monochromator (PGM) used at beamline UE46, delivers X-rays with a narrow spectral bandwidth ($\frac{\Delta\lambda}{\lambda}$) of $5*10^{-4}$ to $1*10^{-4}$ (depending on the grating and the X-ray energy) necessary for diffraction limited focusing (due to the high chromaticity of the FZPs). Figure 3.5 b) shows the arrangement of FZP, OSA, sample and detector in the core of the microscope (see also figure 2.6). The design of the microscope allows very short distances between these components and thus allows the usage of high resolution zone plates which have very short focal lengths.

[2]proportional–integral–derivative

3.3.2 Hard X-ray experiments

All experiments in the hard X-ray regime, were performed at the microoptics test bench (MOTB) at the ID6 beamline at the ESRF in Grenoble, France. This undulator beamline is dedicated to the evaluation of techniques and instruments and offers a flexible environment for various kinds of tests. The MOTB is equipped with a large and solid optical table, made of granite, that hosts a stage assembly for the manipulation of specimens and to carry a camera. A CCD-camera (Sensicam QE) with 1376 x 1040 pixels and a size of 6.45 μm per pixel is used to record images. In front of the CCD-chip, a scintillator converts the incoming X-rays into visible light. In combination with an objective (Olympus UPLAPO x10) which performs a magnification by a factor of 10, the resolution of the camera (defined as two pixels) is 1.3 μm with a field of view of 887 x 670 μm. The distance between the camera and the other stages can be adjusted in a wide range, which allows other components to be placed in the optical path as described below. For all experiments, a beam energy of 8 keV was used.

Qualitative characterization of the zone plates

In a first test, the diffraction characteristics of the zone plate in the form of a qualitative evaluation were tested.

Description of the experiment By focusing the nearly parallel incoming X-rays onto the screen of a CCD-camera, different patterns are obtained and allow to qualitatively characterize the FZP. A schematic illustration of the ray paths and the corresponding patterns on the CCD-camera for different focusing conditions are presented in figure 3.6. The active zones of the FZP form a cone of diffracted light which narrows towards the focal length, reaches a spot with minimum diameter at the focal length and then diverges again. In figure 3.6 a) the camera is shown in overfocused condition (distance between camera and FZP larger than f). In this geometry the diffracted light forms a ring on the screen of the CCD-camera. In figure 3.6 b) FZP and camera are shown in focused condition. Here, only a spot of diffracted light is visible on the screen of the camera.

Description of the setup The zone plate holder consists of a 2 mm thick aluminium plate, containing 3 holes with a diameter of 200 μm to let the incoming radiation pass through the zone plates and confine it to the given diameter (Drawings of all mechanical components are presented in appendix D.). The FZPs (mounted on the TEM-grids as

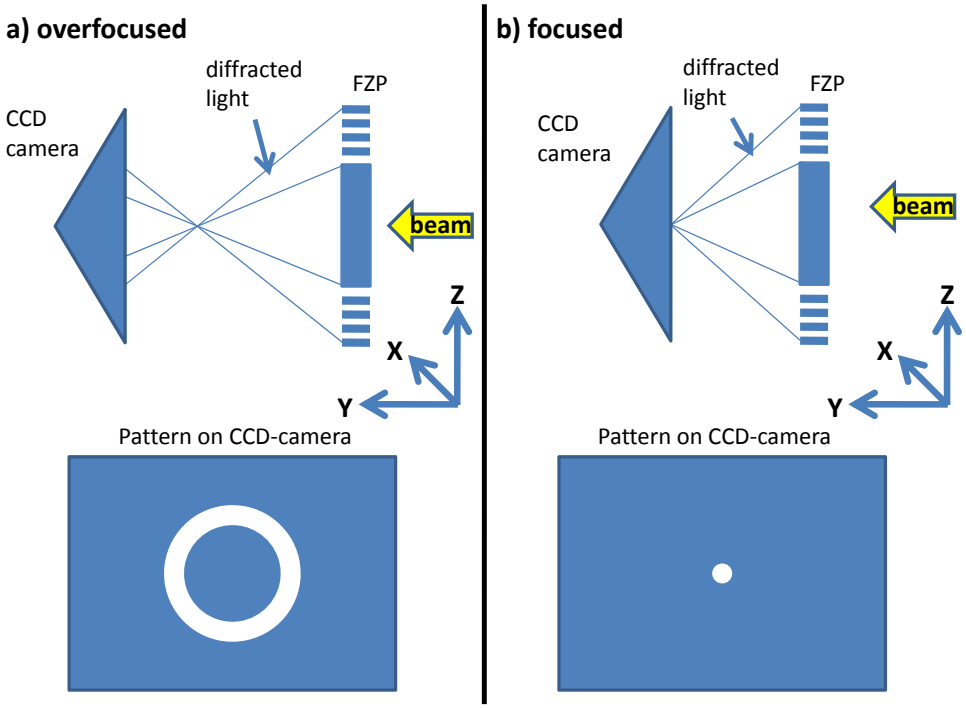

Figure 3.6: Ray paths for the qualitative characterization of the FZPs. a) FZP and camera in overfocused condition. b) FZP and camera in focused condition.

shown in section 4.2) are glued in front of the holes with conduction silver paste. The holder plate is screwed to a base plate which is connected via a post to a sample stage (by HUBER Diffraktionstechnik GmbH & Co. KG) which allows translation in X,Y and Z as well as rotation around the Z-axis (yaw) and the X-axis (pitch). The coordinate system is defined right-handed, with the Y-axis pointing in beam direction downstream (figure 3.7). The diffracted radiation is collected with the CCD-camera described above, which is also mounted on a stage assembly (by HUBER Diffraktionstechnik GmbH & Co. KG). Its positioning is adjustable in X and Z allowing the centering of the camera in the beam. Besides the light diffracted by the active zones, the image on the screen is a direct projection image of the zone plate on its TEM-grid. The setup is shown as a schematic illustration and the corresponding photographs in figure 3.7.

Conduction of the experiment First, the camera is centred on the optical axis. Then, sample stage and camera are moved towards each other until a section of, or a complete bright ring (overfocused condition) appears in the projection image of the zone plate on the CCD-camera. The bight ring consists of light which is diffracted from the zones of the

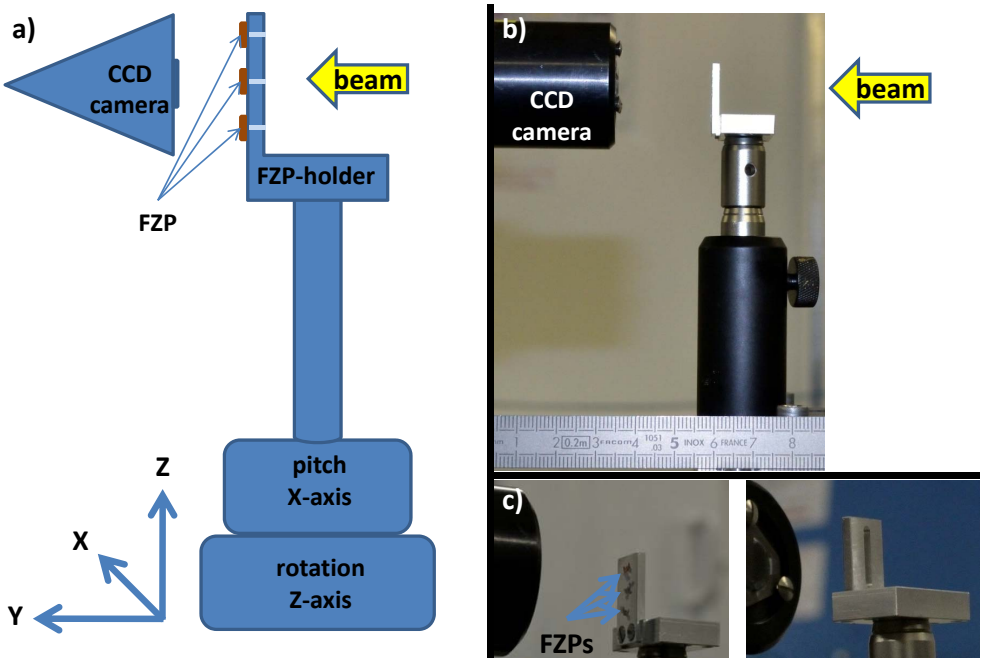

Figure 3.7: Schematic illustration a) and photograph b) of the test setup for the qualitative evaluation of the diffraction characteristic of the zone plate. The X-ray beam enters the assembly from the right. The FZP is mounted on a sample stage which can be adjusted in X, Y, Z and rotation around the X- and Z-axis. The CCD-camera on the left can also be adjusted in X, Y and Z to capture the light transmitted through one hole at a time. c) Shows a detailed view of the zone plate holder and the camera from different perspectives, to show the three zone plates mounted on the holder.

zone plate into focus, accompanied by dark areas on the active zones. At the same time as the bright ring appears, the area on the zone plate from which the light is diffracted away appears dark in the image. If camera and FZP are moved further towards each other, the diameter of the ring decreases as the FZP approaches the focal point. If only a section of a ring appears, the inclination between zone plate and beam has to be corrected via rotation of the sample stage around the X- and Z-axis until the ring closes, that is until the FZP surface is perfectly perpendicular to the beam. After this correction, FZP and camera are further approached until the ring of diffracted light reaches a minimum in diameter. In the ideal case, it is possible to focus the light into just one pixel, because the pixel size of the camera is 0.645 μm and the zone plates are expected to produce focal spots with a diameter of 10, 15 and 35 nm. The ratio of the power of the beam in the focal spot to the incident power of the beam on the FZP surface gives an estimation of the efficiency of the zone plate.

Full-field microscopy

Description of the experiment To evaluate the imaging capabilities of the FZP more accurately and to gain insight into its resolution, an open TXM setup has been built. The reasons for the special geometrical circumstances for imaging are given in chapter 4. A schematic illustration of the imaging geometry is shown in figure 3.8. The nearly parallel

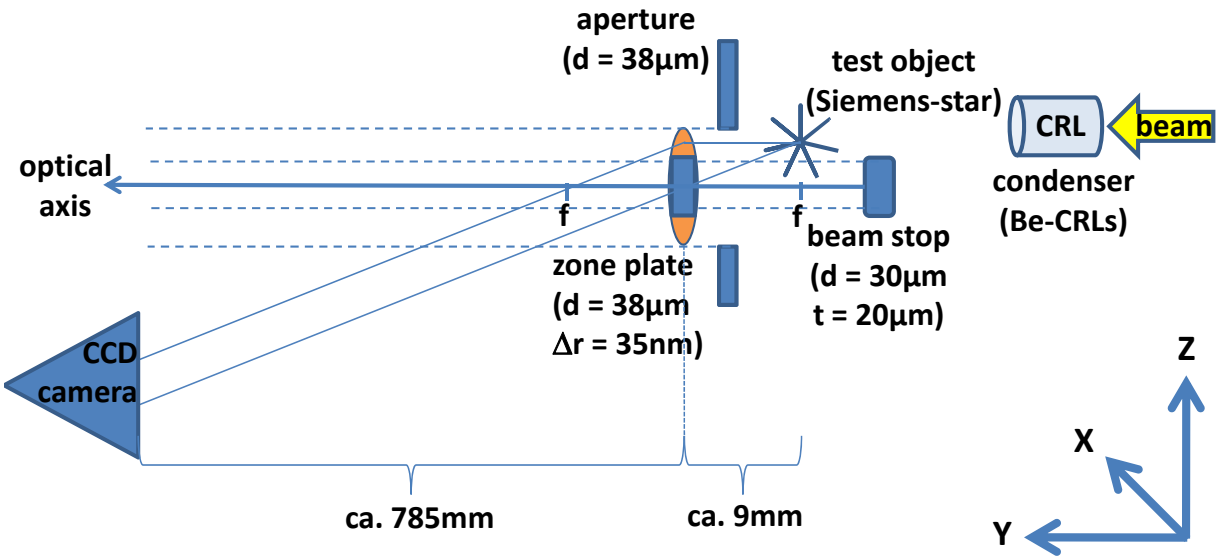

Figure 3.8: Schematic illustration of the full-field setup with the imaging geometry.

X-ray beam from the beam line, is focused by a condenser onto the sample. The multilayer zone plate serves as objective lens, creating a magnified image on the CCD-camera. A beam stop blocks radiation from passing through the glass core of the zone plate and an aperture prevents radiation passing around it.

Description of the setup The components of the setup are presented in figure 3.9. The setup consists (figure 3.9 a)) of a condenser (beryllium compound refractive lenses (see section 2.3.3)), a gold beam stop (30 μm diameter, 30 - 40 μm thickness by NTT AT Corporation), the sample (Siemens-star (X50-30-7), minimal structure size 50 nm in gold, structure height 650 nm by Xradia), the aperture (Pt/Ir (95/5 %) stripe with pinholes of 38 μm diameter by Günther Frey GmbH & Co. KG), the zone plate (Δr =35 nm) and the CCD-camera (see above). Sample, aperture and zone plate are hereby fixed on a small additional table which is equipped with 9 stages (by Newport cooperation) arranged in groups of three to allow for X,Y and Z adjustment of all components. Figure 3.9 b)

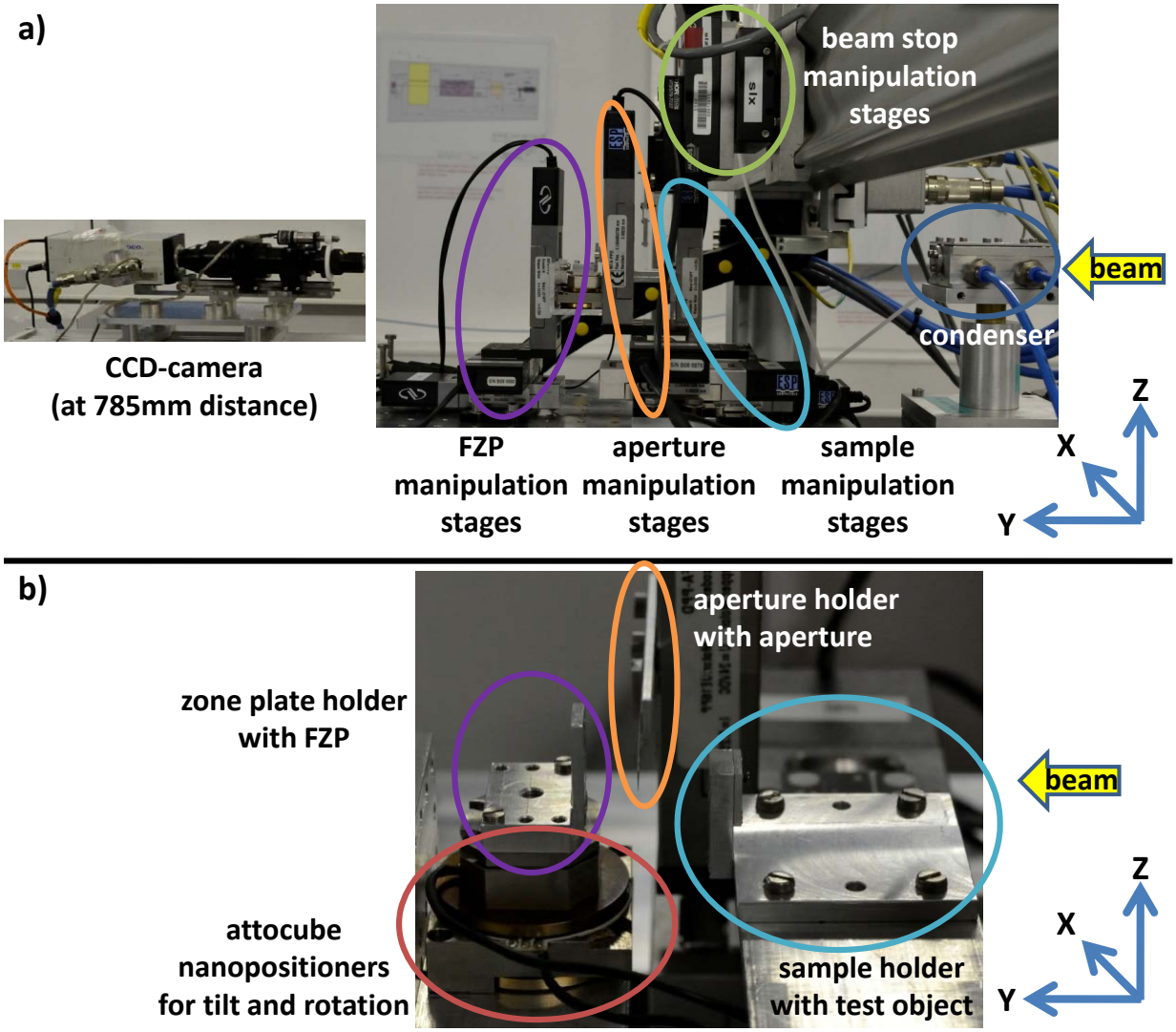

Figure 3.9: a) Overview photograph of the setup with condenser, stages of the manipulation of the optical components and CCD-camera. b) Close-up view of test object, aperture and zone plate holder. The zone plate holder is mounted on attocube nanopositioning devices to adjust rotation and tilt of the zone plate. (Same colours have been used in a) and b) to mark same components.)

shows a close-up view of test object, aperture and zone plate holder. In addition to the possibility of X,Y and Z alignment, the zone plate is mounted on a two nanopositioning devices (ANR200/RES and ANGt101/RES by attocube systems) to allow for rotation around the Z-, and tilt around the X-axis, respectively. The distances between sample and FZP and FZP and CCD-camera are approx. 9 mm and 785 mm, respectively.

Chapter 4

Results

In the first part, theoretical calculations of the diffraction efficiency are presented. Then, the new fabrication technique and procedure for the zone plates is explained in detail and the results of the microscopic characterization will be shown. Finally the X-ray optical performance of the FZPs in the soft and hard X-ray regime is presented.

4.1 Theoretical considerations

The choice for the optimal material combination was based on the results of the theoretical calculations of the diffraction efficiency of several material combinations and on the calculation of the optimum FZP thickness.

Choice of materials

Several material combinations were theoretically investigated by calculating their diffraction efficiencies depending on the FZP thickness for several "working" X-ray energies. The "working" energy is defined as that X-ray energy at which the zone plate is to be used. The diffraction efficiencies for working energies of 1200 eV and 8000 eV are shown in figure 4.1 and 4.2, respectively. The calculations were performed, using the "*Kirz*-theory" (equation 2.21 defined on page 34). From the calculations for both energies it is evident, that several candidates exist for multilayer zone plate fabrication which show high diffraction efficiencies. The maximal diffraction efficiencies for all material combinations at both working energies are summarized in table 4.1. At both working energies, the combination SiO_2 - Al_2O_3 shows the highest diffraction efficiency, followed by the other combinations containing SiO_2 and completed by the combination Al_2O_3 - Ta_2O_5. As the

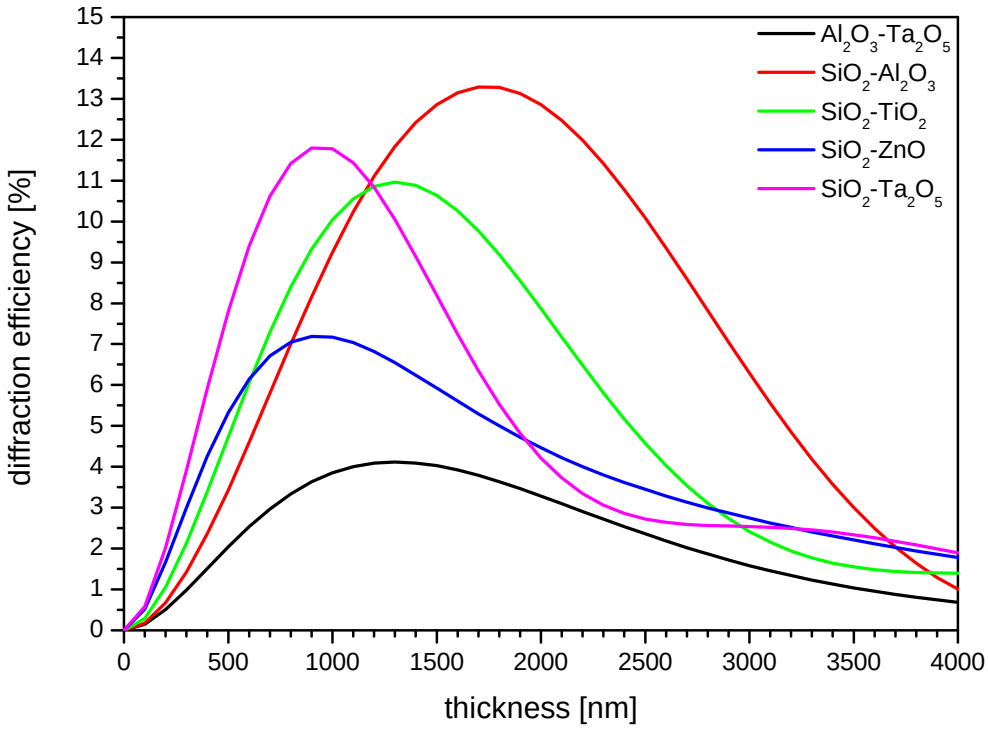

Figure 4.1: Diffraction efficiencies at a working energy of 1200 eV for the material combinations: Al_2O_3 - Ta_2O_5, SiO_2 - Al_2O_3, SiO_2 - TiO_2, SiO_2 - ZnO and SiO_2 - Ta_2O_5 calculated with the *Kirz*-theory.

deposition of SiO_2 with ALD is still difficult and not reliable (see below), the material combination Al_2O_3 - Ta_2O_5 was chosen for the production of all FZPs for this thesis. Both, the deposition of Al_2O_3 and Ta_2O_5 is known [138, 139], and expertise in multilayer production of these materials also exists [43].

A reliable deposition process for SiO_2 as an important dielectric is highly desirable for the semiconductor industry. Possible precursors for its deposition are for example $SiCl_4$ and H_2O. The process itself is however highly complicated as it either requires high temperatures > 325°C or the use of catalysts like ammonia (NH_3) [145] or pyridine (C_5H_5N) [146]. Furthermore, corrosive hydrochloric acid (HCl) as a reaction by-product is formed, which requests special safety precautions and can form ammonium salts with the halide precursor, that can impede the SiO_2 film growth. To avoid salt formation, alternative

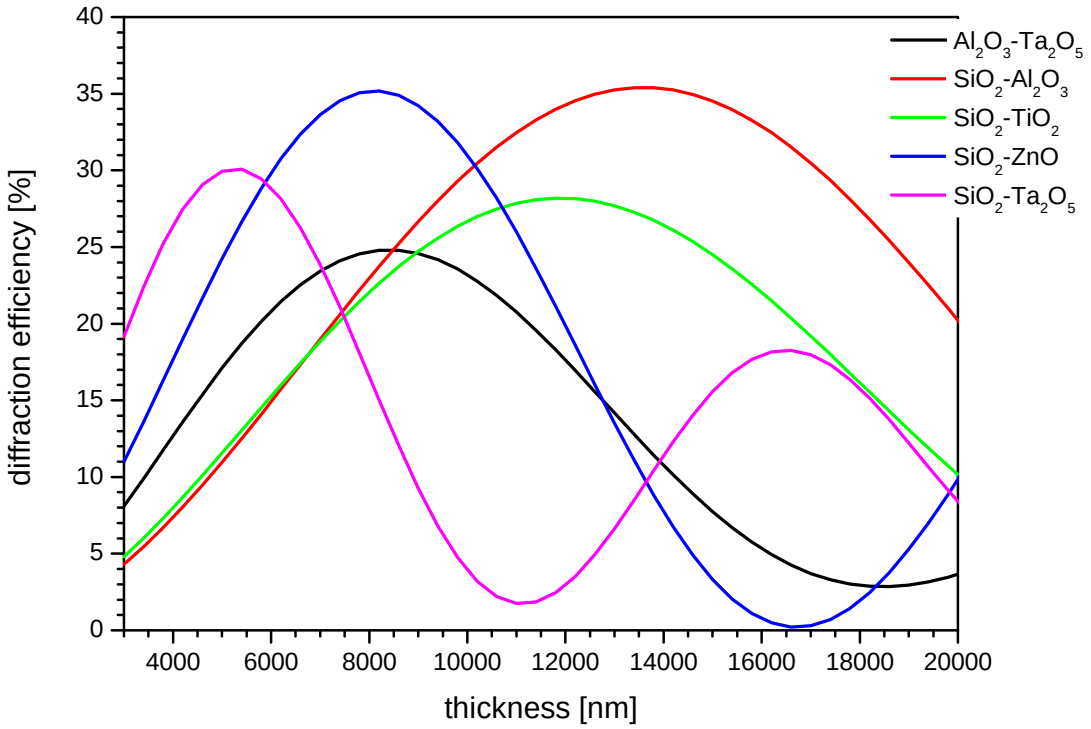

Figure 4.2: Diffraction efficiencies at a working energy of 8000 eV for the material combinations: Al_2O_3 - Ta_2O_5, SiO_2 - Al_2O_3, SiO_2 - TiO_2, SiO_2 - ZnO and SiO_2 - Ta_2O_5 calculated with the *Kirz*-theory.

precursors like tetraethoxysilane (TEOS) and H_2O with NH_3 as a catalyst have been applied [147]. Yet a general drawback for this and almost all processes for SiO_2 deposition are the long cycle times which are required to reach completion in the reactions and which result in a low productiveness when applied to Fresnel zone plate production. Another process is the so-called "rapid" ALD deposition of SiO_2 with tris(tert-butoxy)silanol ($(Bu^tO)_3SiOH$) as a precursor and TMA as a catalyst at temperatures between 225 and 250°C [148]. In this process the cycle times are extremely long but accompanied by a very large deposition rate of 120 $\AA$/cycle. A large deposition rate is normally desirable as long as the growth proceeds in a surface controlled manner and if thick films have do be deposited. For the deposition of thin films for zone plate applications however, the thicknesses have to be controlled very accurately and the variation has to be slow and with respect to the zone plate design rule. Therefore large steps of 120 $\AA$/cycle are not desirable. In addition, the long-term stability

Table 4.1: Maximum diffraction efficiencies, calculated for complete zone plates, for several material combinations at working X-ray energies of 1200 and 8000 eV.

material combination	maximum efficiency at 1200 eV [%]	maximum efficiency at 8000eV [%]
Al_2O_3 - Ta_2O_5	4.1	24.9
SiO_2 - Al_2O_3	13.3	35.4
SiO_2 - TiO_2	11.0	28.2
SiO_2 - ZnO	7.2	35.2
SiO_2 - Ta_2O_5	11.8	30.1

of the process has not yet been demonstrated. More recently a self-catalytic deposition process for SiO_2 from 3-aminopropyltriethoxysilane ($H_2N(CH_2)_3Si(OCH_2CH_3)_3$), H_2O and ozone (O_3) has been presented [149]. This process is claimed to be free of hazardous by-products, to show beneficial growth characteristics and to produce high quality films. The use of 3 precursors however lowers its productiveness. Again, the long term stability and the possibility to use short cycle times has not been investigated. As a consequence of the problems and uncertainties of the aforementioned processes, Al_2O_3 and Ta_2O_5 have been chosen as materials for the zone plates due to their well known chemistry, the controllability and the long-term stability of their deposition processes.

Optimum FZP thickness

The *Kirz*-theory, according to equation 2.21 treats the FZP in the "thin grating" approximation. The thickness of the FZP is only taken into account to calculate the phase shift of the wave inside the material, but no volume effects, caused by an increase in the aspect ratio of the zone plate, are respected. Therefore the CWT, which takes FZP thickness, outermost zone width and hence volume effects into account, has to be applied to calculate the optimal FZP thickness depending on the outermost zone width and the working X-ray energy. The optimum FZP thickness is that thickness where the diffraction efficiency reaches a maximum. The diffraction efficiencies, calculated for outer zone widths of $\Delta r = 10$, 15 and 35 nm at working energies of 1200 eV and 8000 eV are shown in figure 4.3 and 4.4, respectively. For comparison, the diffraction efficiencies calculated with the *Kirz*-theory are also shown. For both working energies, the efficiency curve progression for a zone plate with $\Delta r = 35$ nm is close to the curve calculated with the *Kirz*-theory. In this case (thin-grating approximation), the aspect ratio of the zone

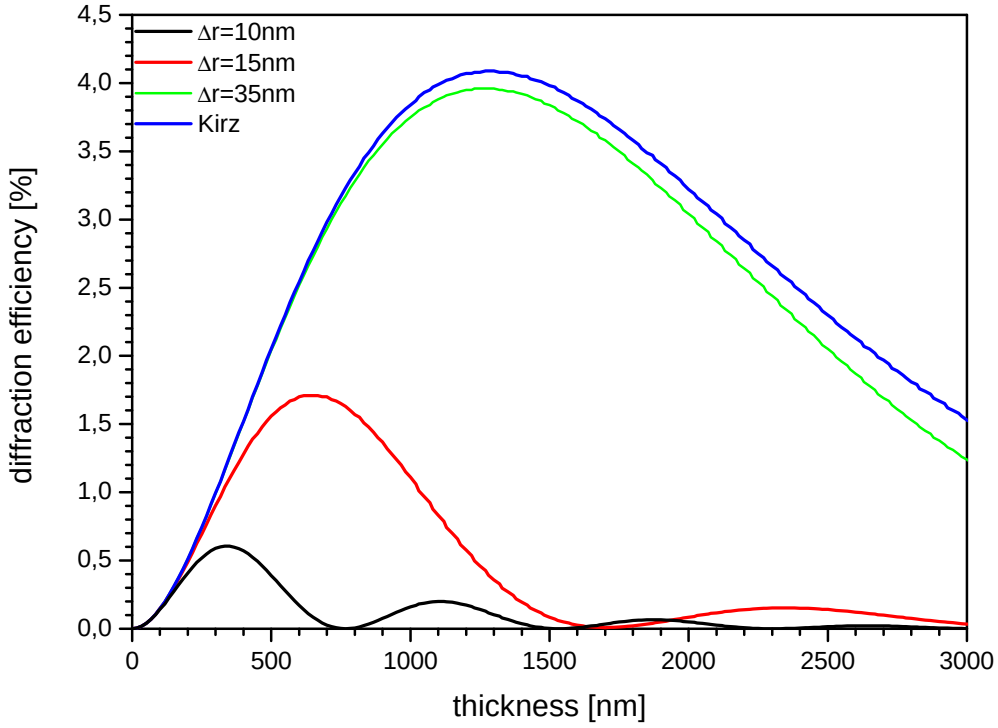

Figure 4.3: Diffraction efficiencies at a working energy of 1200 eV for the material combination Al_2O_3 - Ta_2O_5 and outer zone widths of 10, 15 and 35 nm, calculated with the CWT. The diffraction efficiency calculated with the *Kirz*-theory is shown for comparison.

plate does not have to be taken into account for the calculation. For outermost zone widths of $\Delta r = 15$ and 10 nm there is a huge derivation between the curves calculated with the CWT and the curve calculated with the *Kirz*-theory. In both cases, volume effects due to the aspect ratios of the zone plates have to be considered for the efficiency calculation and the *Kirz*-theory is no longer valid. The optimum FZP thicknesses and the corresponding maximal diffraction efficiencies for both working energies and all zone widths are summarized in table 4.2. As expected, the efficiency decreases with decreasing outer zone width, when Δr reaches the order of magnitude of the X-ray wavelength [150]. To avoid this decrease in efficiency with decreasing Δr, the zone would have had to full-fill the *Bragg*-condition with respect to the incoming beam, which is impossible in this case due to the use of a cylindrical glass fibre as substrate, and the yet parallel zones.

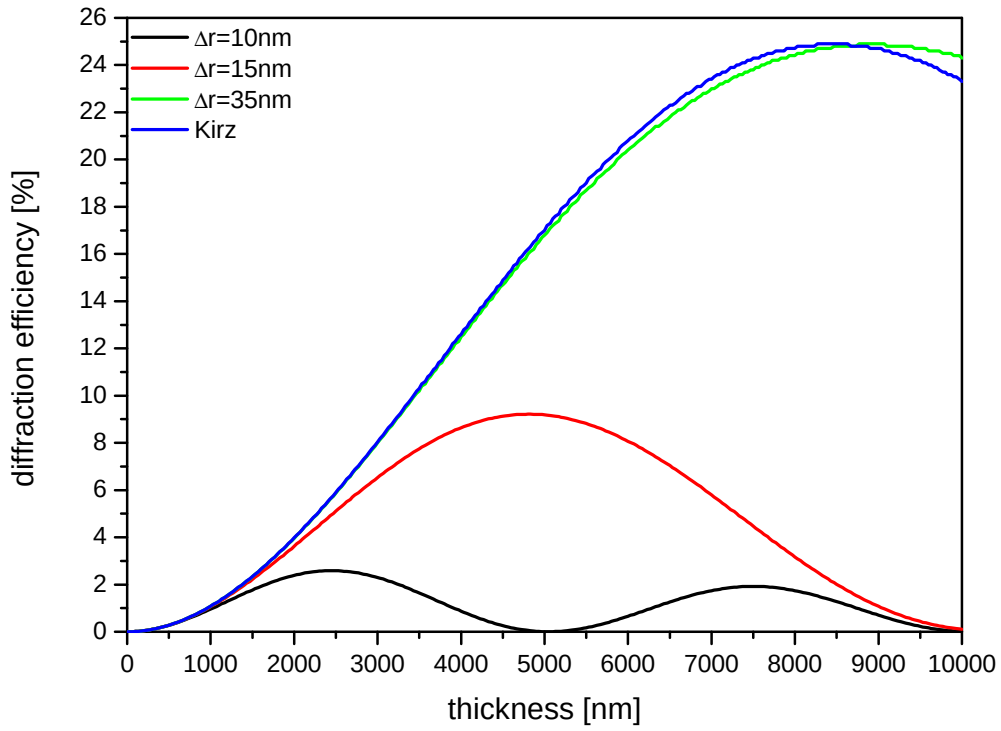

Figure 4.4: Diffraction efficiencies at a working energy of 8000 eV for the material combination Al_2O_3 - Ta_2O_5 and outer zone widths of 10, 15 and 35 nm, calculated with the CWT. The diffraction efficiency calculated with the *Kirz*-theory is shown for comparison.

The calculations also show, that thicknesses smaller than 1300 nm are necessary for high resolution zone plates in the soft X-ray regime. This range of thicknesses was not accessible with mechanical sectioning and thinning techniques in previous attempts to manufacture multilayer zone plates. In the hard X-ray regime, thicknesses above 2400 nm are required for zone plates which combine high resolution with high efficiency. These thicknesses, corresponding to high aspect ratios in conjunction with very fine outer zone widths, are not accessible to FZPs made by EBL.

4.2 Fabrication

Three different types of zone plates with outermost zone widths of $\Delta r = 35$, 15 and 10 nm were prepared. The basic concept of the fabrication method is outlined in figure 4.5.

Table 4.2: Optimum FZP thicknesses and peak diffraction efficiencies, calculated for complete zone plates, for all outer zone widths at working X-ray energies of 1200 and 8000 eV.

outermost zone width [nm]	working energy [eV]	optimum FZP thickness [nm]	peak diffraction efficiency [%]
35	1200	1262	4
35	8000	8920	25
15	1200	644	1.7
15	8000	4812	9.3
10	1200	339	0.6
10	8000	2451	2.6

Partial zone plates with a total thickness of active layers of 4 μm, deposited on a 30 μm

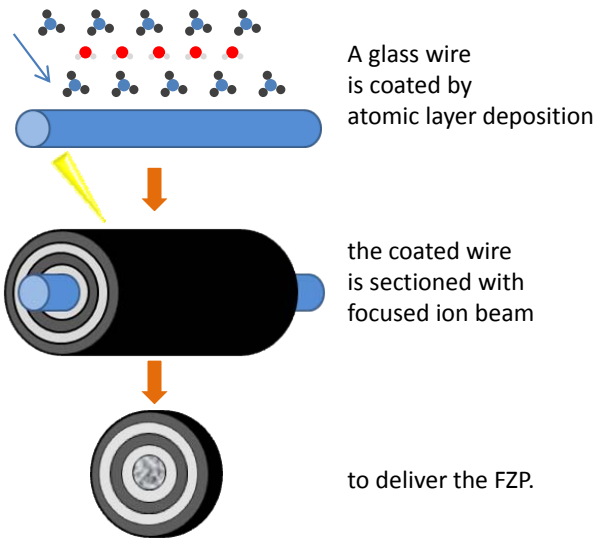

Figure 4.5: Basic concept of the fabrication: a glass fibre is coated by atomic layer deposition (ALD) with a multilayer of X-ray absorbing and transparent material and sectioned by focused ion beam to obtain a slice, which is the zone plate.

diameter fibre, leading to a overall diameter of 38 μm for the FZP, have been produced. The glass fibre is coated with a multilayer of X-ray absorbing and transparent material in an ALD process and sectioned and thinned with focused ion beam to deliver a slice, the Fresnel zone plate.

As a substrate, a commercially available glass fibre (A2 by SCHOTT AG) with 30 μm diameter was chosen, for its high roundness (below 50 nm, measured on a cross-section

by transmission X-ray microscopy), its high smoothness (below 1 nm measured by atomic force microscopy (AFM)) and its reactive surface with terminal hydroxyl groups, advantageous for the deposition process. A TXM image of a cross-section of the coated

Figure 4.6: TXM cross-section image of the glass fibre used as a substrate for the multilayer zone plate.

fibre is presented in figure 4.6, which has been obtained at 1300 eV photon energy with an exposure time of 2 s. The boundary between the glass and the deposited zones is located between the light grey and the dark grey area. This image has also been used to measure the roundness of the fibre by fitting a circle into the boundary and evaluate the difference in radii in horizontal and vertical direction. The available accuracy is two pixels of the applied X-ray CCD-camera which provides an image pixel size of 25 nm at the chosen magnification of 802-fold which corresponds to a roundness below 50 nm. The resolution of the image is also determined by the micro zone plate, which had a better resolution than the image pixel size of the camera. For the deposition, the fibre was point-glued onto a metal mesh with a low-degassing epoxy glue (Polytec PT) to enable an easy precursor access from all sides.

ALD was chosen as deposition method due to the high quality of the deposited layers, the accurate thickness control and the high confromality of the layers on almost every substrate geometry. With ALD it is possible to coat the fibre from all sides without rotation, which cannot be achieved with physical deposition methods and is an advantage

of the method, as it allows vibration free deposition.

FIB was chosen as sectioning and thinning method due to the wide range of accessible thicknesses for the final FZP and the good surface quality of the cuts. The use of FIB offers, for the first time, thicknesses for multilayer FZPs, suitable for the soft X-ray regime. The optimum thicknesses were also calculated theoretically (section 4.1). The sectioning and thinning procedure is described in detail in section 4.2.2.

A summary of all chemicals, substrates and mechanical elements of the setups is given in appendix D.

4.2.1 Deposition of the Fresnel zone plates

Before the deposition of the actual the zone plate, the growth rate of Al_2O_3 and Ta_2O_5 was determined. Films of different thickness were deposited on Si (100) substrates under different growth conditions. The thickness was measured with variable angle spectroscopic ellipsometry (VASE) in a Woollam M-2000V ellipsometer. The data was analysed with the WVase32 software. From the measured thicknesses the growth rates for both materials were calculated (results are given in appendix B). The necessary number of cycles for each zone was then calculated form the growth rate. As already mentioned, partial zone plates with an outer zone width of $\Delta r = 35$, 15 and 10 nm were deposited onto a 30 μm glass fibre substrate. For the $\Delta r = 35$ nm a decrement (variable over the progression of the deposition) was defined, with which the amount of ALD cycles was reduced after each deposited zone. For the $\Delta r = 10$ and 15 nm zone plate, a given number of zones had to be approximated with a constant number of ALD cycles, due to the slowly varying zone width. The detailed strategy, how the individual zone thicknesses, calculated via the zone plate design rule (equation 2.9) were approximated with the number of ALD cycles is given in appendix B. An overview of the prepared zone plates with their corresponding cycle numbers is given in table 4.3. For all zone plates, more than 100 zones were deposited, which is considered as the lower limit to get a satisfying behaviour of the FZP when it is used as a lens [151]. Onto all zone plates, a capping layer of 1000 cycles Ta_2O_5 was deposited to protect the outermost zones. All cycle times for all zone plates are summarized in table 4.4.

Table 4.3: Summary of all zone plates prepared for this thesis and their cycle numbers.

name of zone plate	zone thickness [nm]		total number of zones	number of ALD cycles				total number of cycles
				Al_2O_3		Ta_2O_5		
	from	to		from	to	from	to	
35	44	35	103	393	327	700	554	51455
15	19	15	240	162	135	248	203	45101
10A	12.7	10	360	116	97	171	138	47318
10B	12.7	10	360	116	97	156	123	44633

Table 4.4: Summary of all zone plates prepared for this thesis and their cycle times.

name of zone plate	TMA [s]	$Ta(OEt)_5$ [s]	H_2O_2 [s]	purge [s]
35	0.1	0.5	2	4
15	0.1	0.5	2	4
10A	0.1	0.5	2	4
10B	0.1	0.5	2	4

4.2.2 Sectioning and thinning of the Fresnel zone plates

In the following, the sectioning and thinning procedure in the DualBeam^{TM} device is described in more detail. The corresponding illustrations are given in figure 4.7 a) to i). Prior to the introduction of the coated fibres into the vacuum chamber of the microscope, a thin layer of Au/Pd was sputtered onto the fibres in a BAL-TEC SCD 500 sputter-coater to make them conductive for the following preparation steps. First a platinum bar of $\geq 5\,\mu$m width and $> 1\,\mu$m thickness is deposited onto the fibre to protect the outermost zones from damage during the ion milling process (figure 4.7 a)). Then, a slice with a width comparable to the platinum bar is cut from the fibre in the area of the bar. The depth of the cut is only 5/6 of the total fibre diametre so that the slice is still attached to the fibre by a small bridge (figure 4.7 b)). This remaining connection between slice and fibre is necessary to keep the slice in position during the attachment of the micro-manipulator for the transfer of the slice from the fibre to its final position on a TEM-grid. This grid is used as holder for further easy manipulation of the zone plate. The manipulator is connected to the slice by platinum deposition (figure 4.7 c)). The connection between slice and fibre is cut through, the slice is transferred to the TEM-grid and attached to it by platinum deposition. When the lens is located at its final position, it is disconnected from the micro-manipulator (figure 4.7 d)) and the space between TEM-grid and slice is filled with platinum to make the connection more rigid (figure 4.7

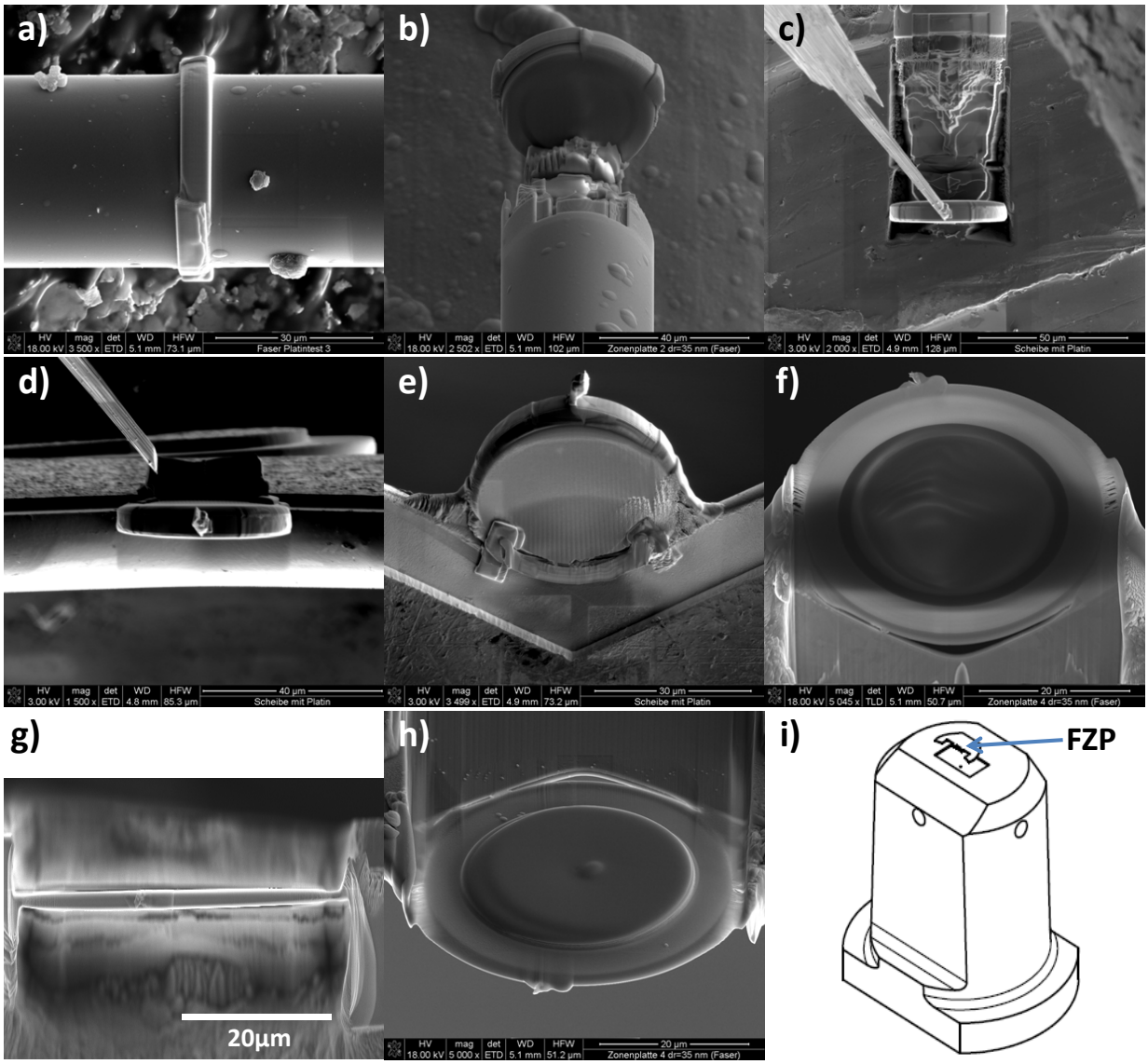

Figure 4.7: Illustration of the preparation steps needed to prepare a FZP with beam stop from a coated fibre. Details are described in the text.

e)). Finally, the zone plate is thinned and polished to its final thickness, depending on the X-ray energy at which it is to be used, by ion beam milling in several steps from both sides (figure 4.7 f) and g)). The exact milling parameters can be found in appendix C.

For the use in the soft X-ray regime, a beam stop to obstruct the 0^{th}-order radiation from passing through the glass substrate, of approx. $2\,\mu$m thickness is deposited directly on the glass core of the FZP by platinum deposition, taking care that none of the active

zones are obstructed by the platinum (figure 4.7 h)). After the preparation, the TEM-grid carrying the FZP is mounted on an appropriate holder. The modified FZP-holder, used in the scanning X-ray microscope MAXYMUS is shown (figure 4.7 i)).

4.3 Microscopic investigation of the Fresnel zone plates

The quality of the ALD deposition was controlled in terms of regularity of the layers, quality of the interfaces and homogeneity of the deposition. For this purpose, SEM images of the prepared zone plates and TEM images of the layers were recorded for. The TEM lamellae were prepared from the fibre by means of DualBeam^{TM}. The same instrument was also used to obtain the SEM images. The TEM images were recorded in a JEOL 4000FX 400 keV TEM.

Figure 4.8 shows a series of SEM and TEM images of the $\Delta r = 35\,nm$ zone plate, demonstrating the quality of the zones deposited by ALD. The TEM lamellae were investigated in terms of thickness of the individual layers and their interface roughness. In figure 4.8 a) the whole FZP is shown. The zones are distributed homogeneously over the whole circumference. The surface of the lens is smooth after the ion milling procedure. No scratches are visible as it is the case for mechanical polishing. This is even better visible in figure 4.8 b) which shows the 103 zones deposited in the ALD process in more detail. The pictures clearly show that the ion milling thinning procedure leaves the zones completely undisturbed. Moreover, the layers show no accumulation in roughness towards the outside, as opposed to sputtered films which are prone to roughness accumulation. For a better investigation of the interface quality the TEM images figure 4.8 c) and d) were taken. White layers indicate Al_2O_3, black layers Ta_2O_5. The overview in figure 4.8 c) contains 38 layers, taken from the central part of the coating. The sharp interfaces between the layers are well visible. No inter-mixture of neighbouring layers is present and no roughness accumulation is noticed despite the large number of deposited layers. The close-up in figure 4.8 d) where only 4 layers are present shows the excellent interface quality. The interfaces are well defined and sharp, even at this magnification, with an interface roughness $\leq 2\,nm$.

The microscopic investigations show, that ALD is well suited for the deposition of

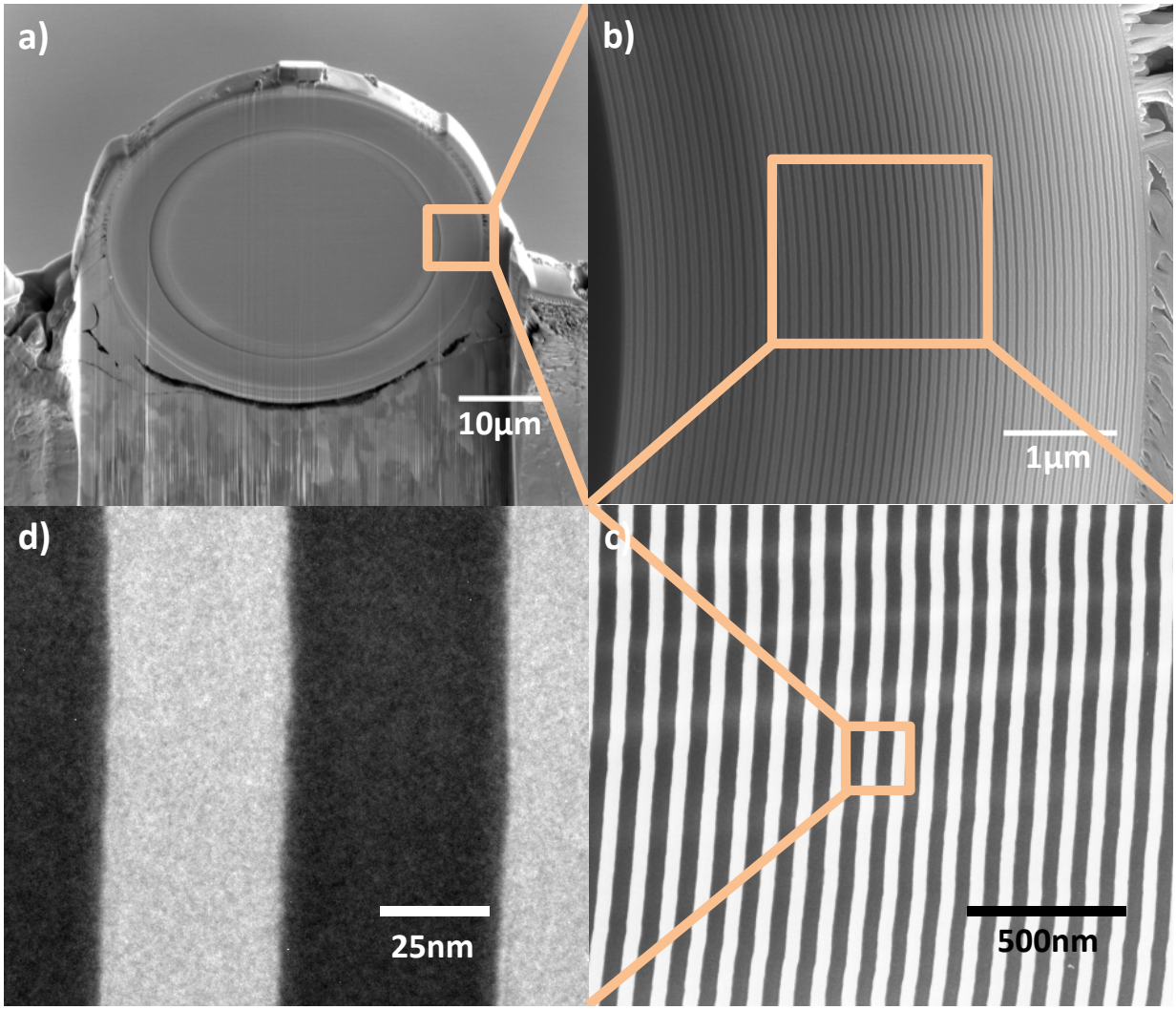

Figure 4.8: Images of the $\Delta r = 35\,nm$ zone plate with increasing magnification. a) And b), SEM images: white layers are Ta_2O_5, black layers are Al_2O_3. c) And d), TEM images of the lower part of the lens: white layers are Al_2O_3, black layers are Ta_2O_5. The zones are very homogeneous. The low interface roughness and sharp compositional changes are well visible and a sign for the high quality of the FZP fabricated with the present technique.

high quality films for zone plate applications. Compared to sputtered films, the quality is indubitably highly superior in terms of low interface roughness, low mixing of adjacent layers and low roughness accumulation even for an overall thickness of $4\,\mu m$. The thicknesses of the individual layers was measured in high resolution TEM images from samples prepared from the upper and lower part and taken form different areas along the fibre. The measured values are compared to the theoretical zone thicknesses calculated via equation 2.9 in figure 4.9, where red circular symbols represent Al_2O_3 layers and black

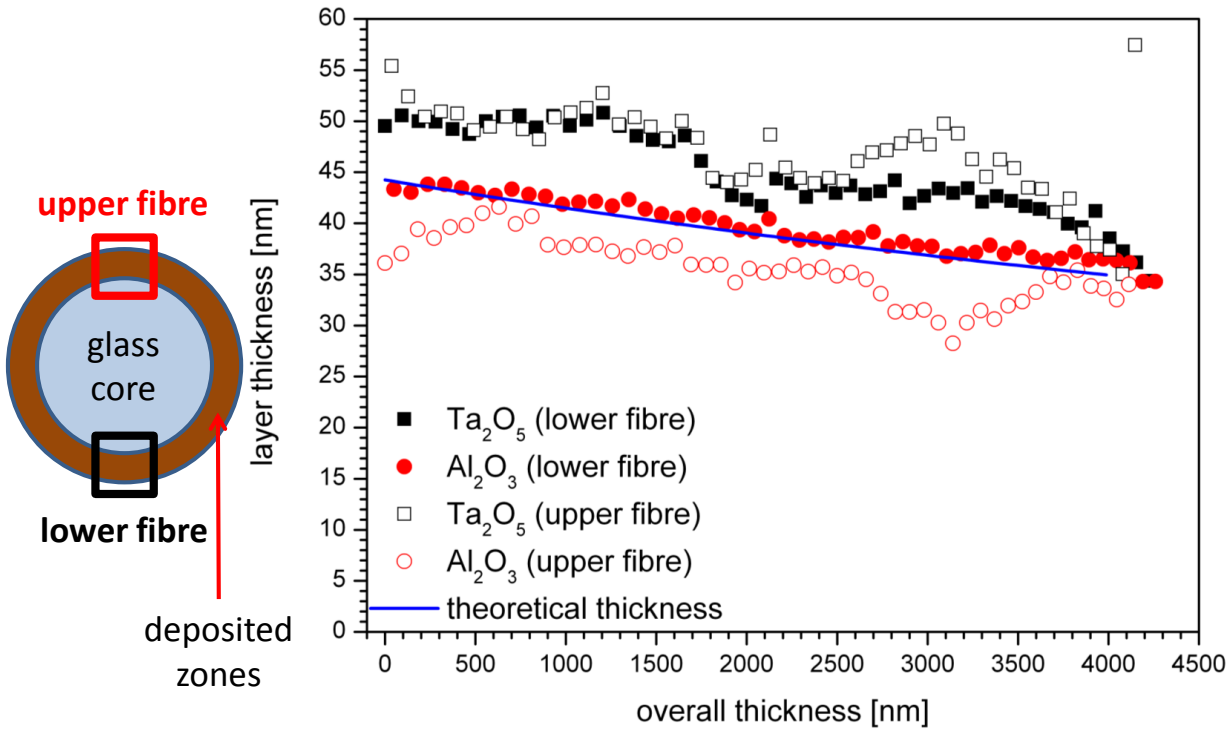

Figure 4.9: Layer thicknesses of the fibre coated with the $\Delta r = 35\,nm$ zone plate structure. Al_2O_3 and Ta_2O_5 layers of the upper and lower part of the fibre, as determined from the TEM measurements, were compared with theoretical thicknesses.

square symbols represent Ta_2O_5 layers. The solid blue line represents the theoretical thickness and the targeted zone thicknesses are presented in appendix B. The deposited overall thicknesses, excluding the capping layer, from the upper and the lower part of the fibre equal 4.15 and 4.29 μm, respectively, whereas the targeted overall thickness equals 4.08 μm (theoretical: 4.02 μm). The TEM measurement shows, that the thicknesses of the Al_2O_3 layers from the lower part of the fibre closely follow the theoretical thicknesses. The Al_2O_3 layers from the upper part of the fibre are mostly thinner than the nominal zone thicknesses. For Ta_2O_5 the situation is different. All Ta_2O_5 layers appear to be thicker than the target zone thicknesses. For layers form the upper part of the fibre, this behaviour is more pronounced than for layers from the lower part of the fibre, especially between 2.5 and 3.5 μm overall thickness. For the outermost zones, the thickness of all layers is close to the theoretical thickness.

Microscopic investigations of $\Delta r = 10\,nm$ and $\Delta r = 15\,nm$ FZP showed, that problems occurred during the deposition process for the 10A and 15 zone plates. SEM images of the

10A, 10B and 15 FZP are presented in figure 4.10, where figure 4.10 a) and b) show images of the 15 FZP as overview and detail image, respectively. The overview shows a conformal coating with well defined zones, sharp interfaces and no accumulating roughness. At the last fifth of the coating (marked with red arrow), the Ta_2O_5 layers are approximately five times as thick as desired and no Al_2O_3 layers can be seen in-between. Figure 4.10 c) and d) show images of the 10A FZP as overview and detail image, respectively. In analogy to the 15 nm FZP, the zones are of high quality as long as the ALD is ideally working. During two short periods of 8 respectively 13 layers however, problems in the process are visible which are marked by red arrows. During these periods, the Ta_2O_5 layers are deposited normally, while the Al_2O_3 layers have almost vanished. Figure 4.10 e) and f) show images of the 10B FZP as overview and detail image, respectively. Both images show, that the deposition worked without any difficulty during the whole process. The zones are well defined and show sharp interfaces and no roughness accumulation is visible. Therefore, ALD is inherently suitable to produce zone structures for zone plates in the $\Delta r = 10\,nm$ and sub-10 nm range.

A closer look on the layers of the zone plate 10B by TEM is presented in figure 4.11. In both images, the white layers indicate Al_2O_3 and the black layers Ta_2O_5. The overview image in figure 4.11 a) shows that the zones of the 10B zone plate have a very regular appearance in the TEM, the interfaces appear sharp, especially towards the end of the deposition and no roughness accumulation is present. Some modulation of contrast is visible in the upper part of the image, which is caused by the sample preparation via FIB. The change in image brightness from the lower to the upper part of the image can be attributed to a change in thickness of the whole sample. The detail image in figure 4.11 b), where the last 15 zones and a part of the capping layer are shown, shows the quality of the layers more accurately. In areas of the sample where the zones have not been disturbed by the ion beam during sample preparation, their interfaces appear very sharp with no accumulating roughness, even for the very last zones. In areas where the ion beam has disturbed the zones during the preparation, the zone boundaries are smeared out. This is for example well visible in the encircled area.

The thicknesses of the individual layers of the 10B zone plate were measured from high resolution TEM images and are compared to the theoretical zone thicknesses (calculated by equation 2.9) in figure 4.12, where red and black symbols represent

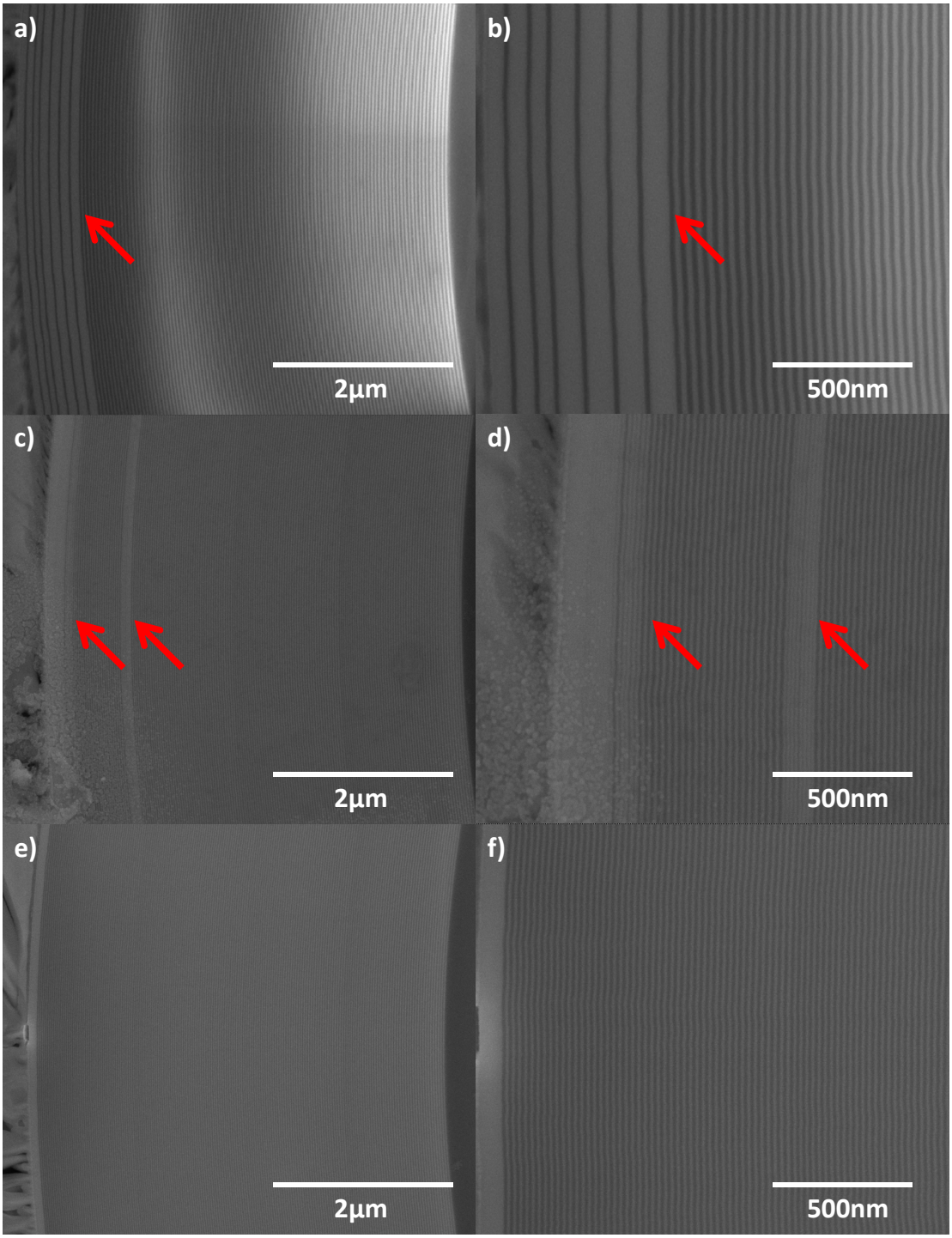

Figure 4.10: SEM images of the (a) and b)) 15 , the (c) and d)) 10A and the (e) and f)) 10B zone plates. Dark layers are Al_2O_3 and light layers are Ta_2O_5. Areas in the zones where problems with the deposition process led to flaws in the structure are marked with a red arrow.

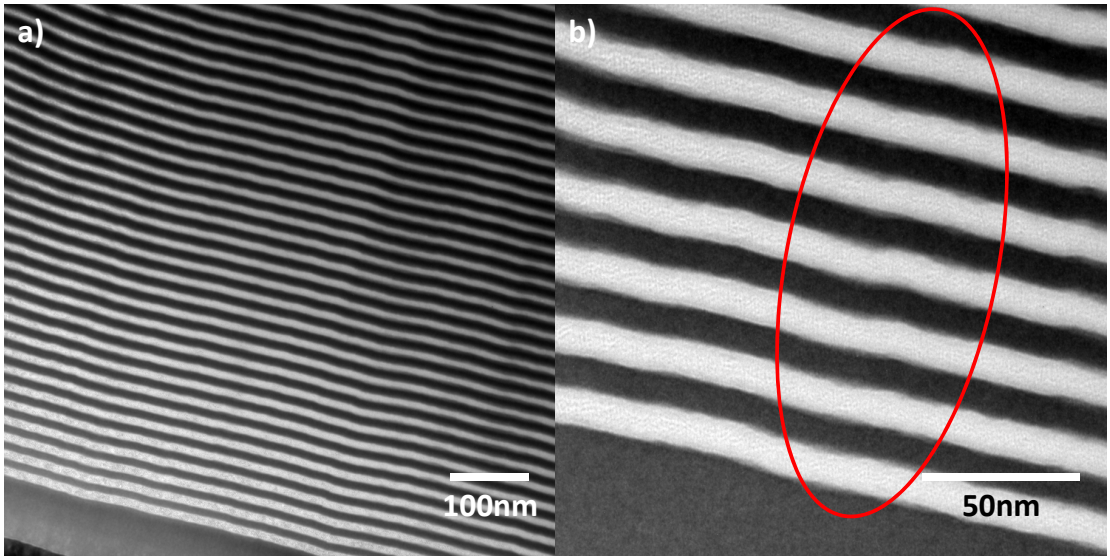

Figure 4.11: TEM images of the 10B zone plate on the upper part of the layer sequence near the capping layer. a) Overview image, b) close-up image.

measured layer thicknesses for Al_2O_3 and Ta_2O_5 layers, respectively. The solid blue line represents the theoretical zone thickness. The deposited overall thickness equals 4.29 μm, whereas the targeted overall thickness equals 4.02 μm (theoretical: 4.01 μm). As described in section 4.2.1 and appendix B, the thicknesses, given by the zone plate design rule, had to be approximated step wise over a given period of cycles to create a convenient deposition scheme. The measured layer thicknesses show a large scattering for both materials. The values of the individual thicknesses were fitted with a straight line, where the fits for Ta_2O_5 and Al_2O_3 lie above the theoretical thicknesses for the whole and most of the deposition, respectively. The slope of the linear fit well resembles the trend of the theoretical zone thicknesses. For Al_2O_3 the fitted line does not deviate as much from the theoretical thicknesses as it is the case for Ta_2O_5, but its slope is shallower which means that the zone plate design rule (equation 2.9) is less obeyed.

The consequences of the results obtained from the microscopic investigation problems of the zone plates on their X-ray optical performance will be presented in the following.

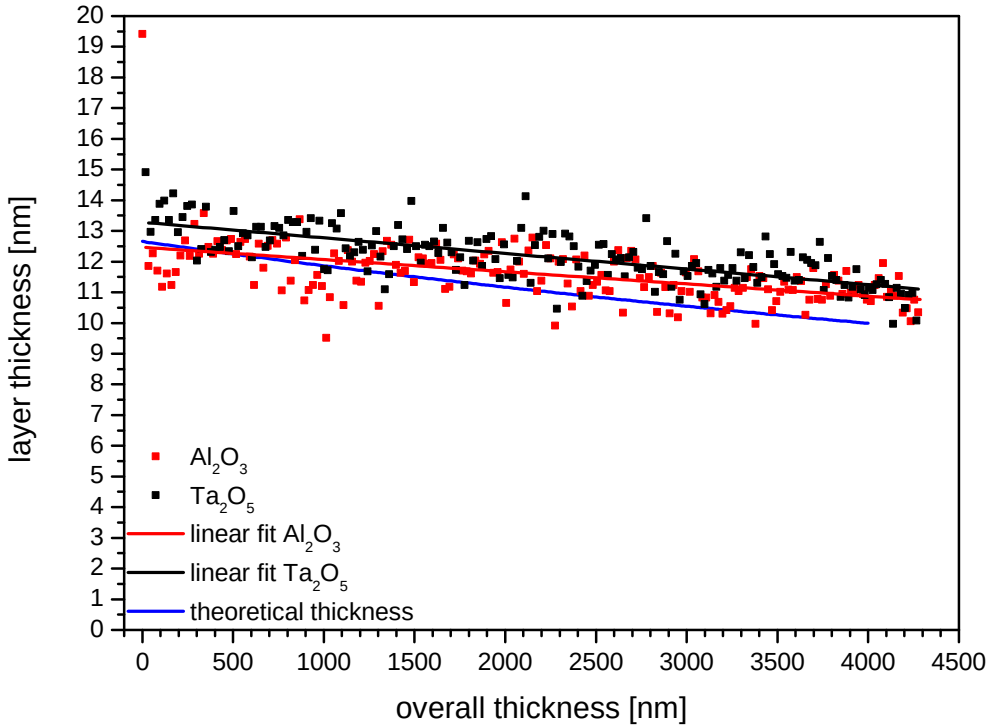

Figure 4.12: Layer thicknesses measured in TEM of Al_2O_3 (red) and Ta_2O_5 (black), compared to the theoretical thickness calculated with equation 2.9.

4.4 X-ray optical performance

4.4.1 Soft X-ray regime

All performance tests in the soft X-ray regime were conducted as proof of principle experiments at the new scanning X-ray microscope MAXYMUS at beamline UE46_PMG2 at BESSY II, Berlin. The imaging performance of the zone plates was tested with different Siemens-star patterns as test objects which are often used to characterize FZPs in terms of resolution.

A series of SEM images of a commercial Au Siemens-star (X30-30-2 by Xradia) as an example of such a test object, with a minimum feature size of 30 nm and a structure height of 180 nm is presented in figure 4.13, where figure 4.13 a) presents an overview over

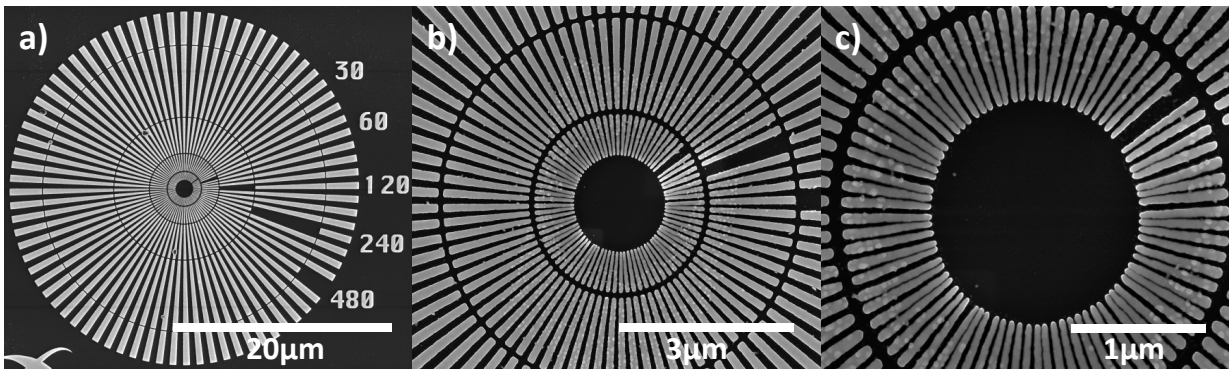

Figure 4.13: Series of SEM images, showing the Au Siemens-star test pattern, X30-30-2 by X-radia. a) Overview over the whole test pattern. The numbers denote the smallest structure sizes in that part of the Siemens-star. b) Image of the two innermost rings of the test pattern. The structure sizes range form 30 nm at the middle of the inner ring over 60 nm at the border between first and second ring to 120 nm at the outer part of the second ring. c) Close-up image of the innermost ring of the Siemens-star.

the whole test structure. The numbers represent the minimum structure sizes in each ring of the test pattern. In figure 4.13 b) and c), the center area of the Siemens-star is shown in more detail.

First X-ray images, acquired with the $\Delta r = 35$ nm zone plate on a Cu-TEM grid at 1150 eV photon energy, with a Ni Siemens-star as test object, manufactured by the X-ray microscopy group at BESSY II, are shown in figure 4.14, where figure 4.14 a) shows an overview over the whole Siemens-star. To obtain this image, a step-size of 88 nm was

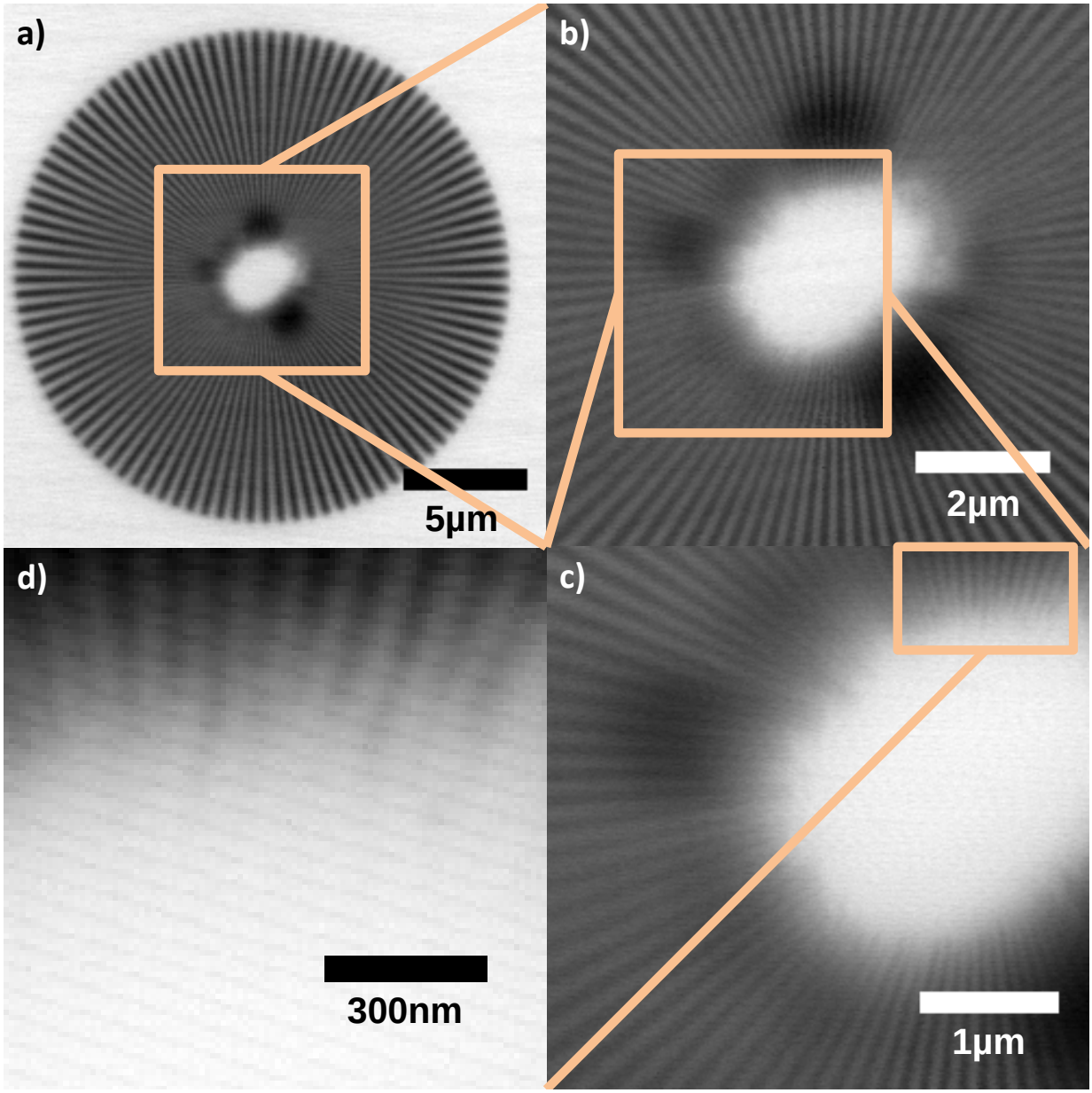

Figure 4.14: SXM images in transmission of details of a Ni Siemens-star test pattern at various magnifications at 1150 eV taken with the $\Delta r = 35$ nm FZP. Structure sizes smaller than 39 nm can be resolved at the highest magnification (image parameters: dwell time 50 ms; step-size 10 nm).

chosen with a dwell time of 1.77 ms/pixel. As the image shows, the zone plate can be used for high resolution X-ray microscopy, since even fine details of the test pattern are visible. In the first zoom-in (figure 4.14 b)) it can already be seen, where the structure of the test pattern turns from resolved to non resolved. The step size here is 32 nm with a dwell time

of 3 ms/pixel. The black parts originate from contaminations of the Siemens-star. A slight degree of astigmatism can be observed, as the resolution along one diagonal is better than along the other. Figure 4.14 c) was taken near the center part of the Siemens-star with a step size of 16 nm and a dwell time of 5 ms/pixel. An area were the structures are fine, well defined and nearly orthogonal to the scanning direction is selected, which is suited for a high resolution scan to evaluate the ultimate resolving power of the zone plate. This high resolution image is shown in figure 4.14 d). A step-size of 10 nm and a dwell time of 50 ms/pixel were used. Very fine features can be resolved in this image.

To evaluate the resolution of the multilayer Fresnel zone plate, a series of nine equidistant line profiles was recorded, as shown in figure 4.15 a), with a length of 360 nm and a spacing of 30 nm starting from the upper end of the image. The variation of the intensity

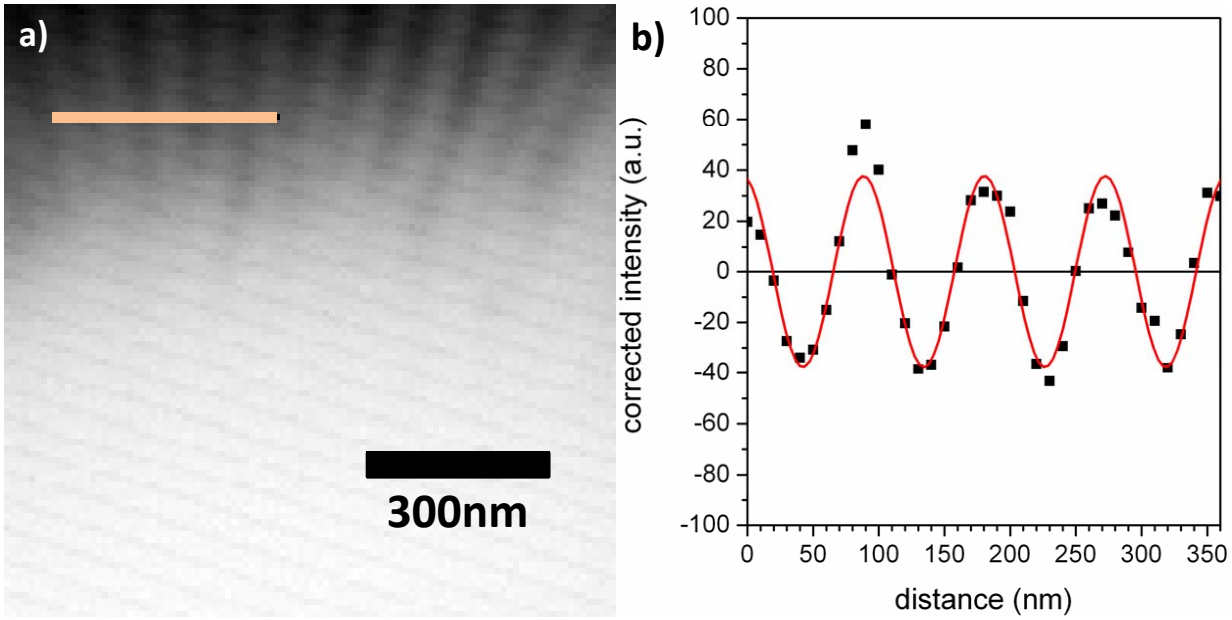

Figure 4.15: a) SXM micrograph like figure 4.14 d). b) Linear profile along the line in a). The regularly spaced inclined lines covering the whole picture and which can be seen especially in the lower left part of the image are synchrotron based artefacts.

along each line can be described by a curve of the form (equation 4.1):

$$I = B + mx + A * sin\left(\pi * \frac{x - x_c}{w}\right), \tag{4.1}$$

where $B+mx$ defines an inclined background intensity, A is the amplitude of the signal

oscillations and w their period. The overall low contrast of the images is due to both, a not perfectly opaque center stop (2 - 6 % transmission from center to edge) and the low total number of zones. The image contrast decreases with decreasing spatial frequency w. Below 38.8 nm, the patterns of the Siemens-star vanish. The resolution of the zone plate lies at or below this value and its determination is here limited by the quality of the Siemens-star pattern and not by the resolution of the zone plate.

As a consequence, a second test with the $\Delta r = 35$ nm zone plate on a Ta-TEM grid and the commercial Siemens-star, presented in figure 4.13 as test object was conducted at 1496 eV photon energy. This energy was chosen to achieve a good contrast between the transparent Al_2O_3 layers and the absorbing Ta_2O_5 layers, as well as a long focal length for comfortable handling of the optical components. The results are shown in figure 4.16, where the SXM image in figure 4.16 a) represents approximately the same field of view as the SEM image in figure 4.13 b). Both images are rotated around 180° with respect to each other. It can be seen form the SXM image, that a slight degree of astigmatism is present in the picture. The horizontal features in the left and right part of the Siemens-star are better resolved than the vertical features in the upper and lower part of the image. The astigmatism resulted in slightly different focal distances for horizontal and vertical focusing and can be due to both, the FZP being not perfectly perpendicular to the beam and not perfectly circular. The SEM image in 4.13 c) represents approximately the same field of view as the SXM image in figure 4.16 b). Again, both images are rotated around 180° with respect to each other. A comparison of both images shows, that nearly all features can be resolved in the SXM image. Here, focus has been set on the vertical features of the Siemens-star in the lower part of the ring. To demonstrate the ultimate resolution of the FZP, the close-up images figure 4.16 c) and d) where taken with a step size of 2.5 nm/pixel. In figure 4.16 c), focus was set on the horizontal and in figure 4.16 d) on the vertical features, respectively. In both cases, a comparison with figure 4.13 c) shows, that even the smallest features of the Siemens-star can be resolved in these images.

Despite the problems encountered with the $\Delta r = 15$ nm and the 10A zone plate, presented in figure 4.10, these lenses were nevertheless tested at MAXYMUS. Unfortunately it was absolutely not possible to perform imaging with the $\Delta r = 15$ nm FZP. No focus could be found with this lens and hence no images could be obtained with it. The imaging capabilities of the 10A zone plate turned out to be very limited as can be seen in figure

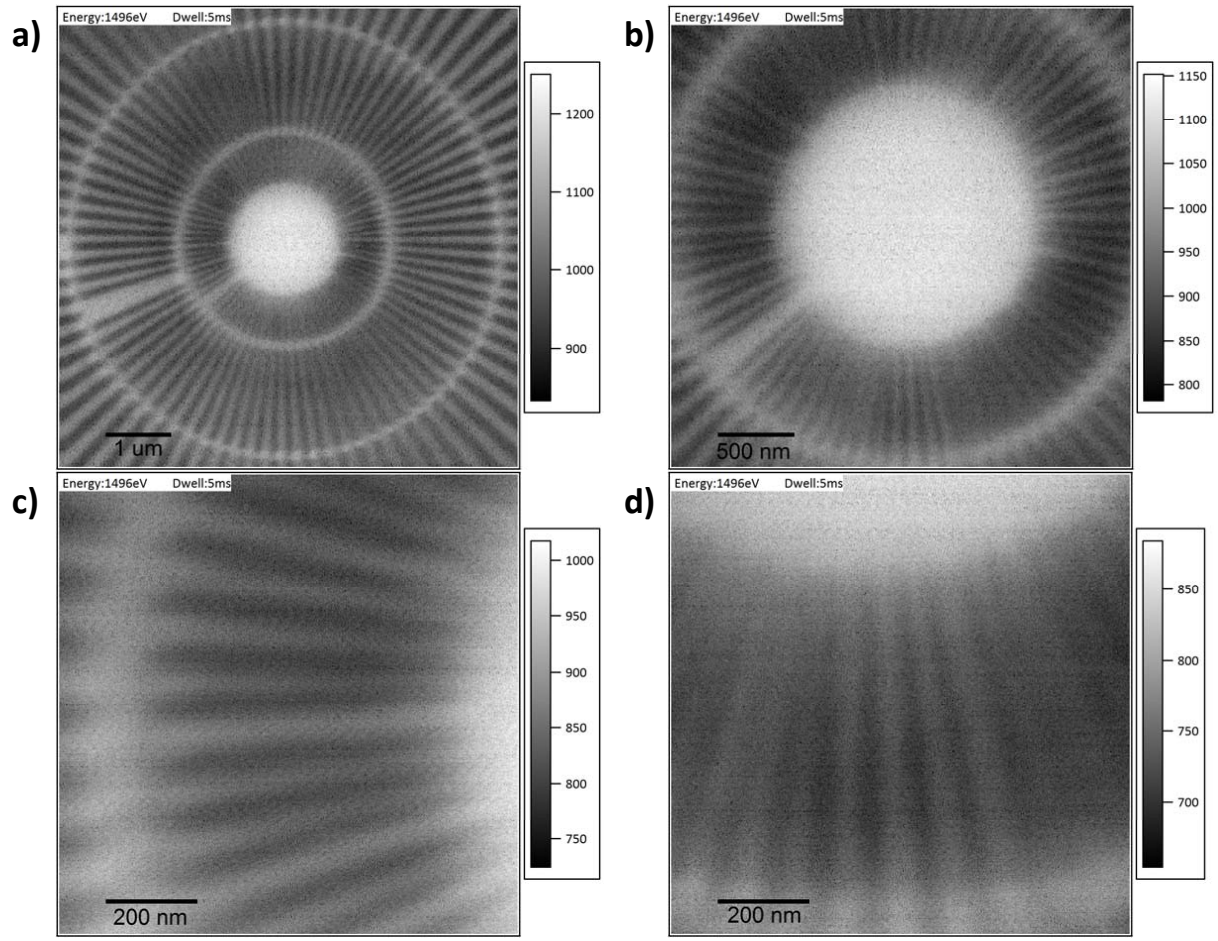

Figure 4.16: SXM images of the Au Siemens-star test pattern X30-30-2. The dwell time was 5 ms/pixel for all images. a) Overview image of the two innermost rings. The largest features of the outer ring are 120 nm, the smallest are 60 nm in size. The step size was 20 nm/pixel. b) More detailed image of the innermost ring. The largest features are 60 nm, the smallest are 30 nm in size. The step size was 10 nm/pixel. c) And d) close-up images of a fraction of the innermost ring. c) Area of the innermost ring where the structures are horizontal, d) area of the innermost ring where the structures are vertical. The finest features can be resolved in both images which were obtained with a step size of 2.5 nm/pixel.

4.17, which was recorded with a dwell time of 20 ms/pixel and a step size of 25 nm. Only structures in the third ring of the Siemens-star and further towards the outside can be resolved in this image, hence with a very low contrast. This imaging performance differs very much from the expected results for a $\Delta r = 10$ nm FZP. The very limited optical performance of these zone plates very likely resulted from the problems during the deposition process, described in section 4.3.

Figure 4.17: SXM image of the Au Siemens-star, obtained with the FZP 10A with a step size of 25 nm and a dwell time of 20 ms/pixel.

4.4.2 Hard X-ray regime

All experiments in the hard X-ray regime, were performed at the microoptics test bench at the undulator beamline ID6 at the ESRF in Grenoble, France. An X-ray energy of 8 keV was chosen for all experiments. First, the diffraction characteristics of the zone plates were tested in the form of a qualitative evaluation. The zone plates were used to focus the nearly parallel incoming X-ray beam onto a CCD-camera as described in figure 3.7. The results of this experiment for the $\Delta r = 35$ nm zone plate are shown in figure 4.18.

All images show the projection of the FZP as absorption contrast image on the screen of the CCD-camera. In the top row of figure 4.18 the results of the adjustment of the FZP via rotation around the Z- and X-axis until a closed, symmetrical diffraction ring has formed, are presented from figure 4.18 a) to d). The bright spots in the centre part are accompanied with dark spots on the active zones, due to the intensity which is diffracted

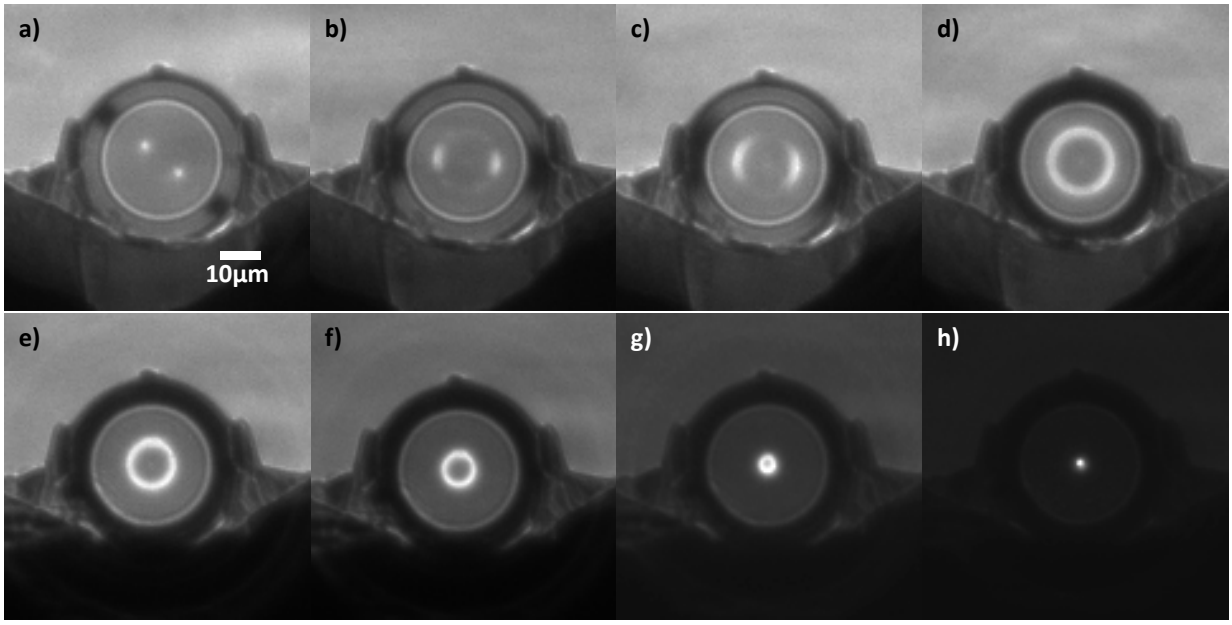

Figure 4.18: Qualitative characterization of the $\Delta r = 35\,nm$ zone plate in the hard X-ray regime. In a) to d), the zone plate is rotated around the Z- and X-axis until it is perpendicularly aligned to the beam and creates a focus ring. In e) to h) the zone plate approaches the camera until it reaches the focal point in h).

away from this area into focus and is thus missing in the projection image. In figure 4.18 b) the FZP has been rotated to some degree around the Z-axis which caused the bright spots on the central part as well as the dark spots on the active zones to grow and to move into horizontal direction. The FZP is further rotated till a ring is formed, indicating that the FZP is perpendicular to the beam. In the lower row of figure 4.18 zone plate and CCD-camera are approached until the diffraction ring turns into a focal spot. Figure 4.18 h) marks the smallest possible diffraction spot. Contrast and brightness are at very low values in this image to avoid over illumination by the very bright focal spot. If the zone plate is moved further towards the CCD-camera, the first order focal spot turns into a ring again, showing that the FZP is now in underfocused condition with respect to the camera. Even further approaching leads to the appearance of the third order focal ring, which finally turns into the third order focal spot, surrounded by the underfocused first order focal ring, which is shown in figure 4.19. A symmetrical, closed diffraction ring could also be obtained with the $\Delta r = 15\,nm$ FZP and the $\Delta r = 10\,nm$ FZP from the deposition series 10B. The results of the focusing tests are shown in figure 4.20, where figure 4.20 a) to d) shows the $\Delta r = 15\,nm$ FZP. For figure 4.20 a) the lens has been adjusted in the best

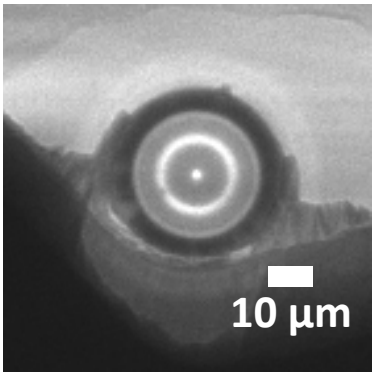

Figure 4.19: 3^{rd} order focal spot, surrounded by underfocused 1^{st} order focal ring of the $\Delta r = 35\,nm$ FZP.

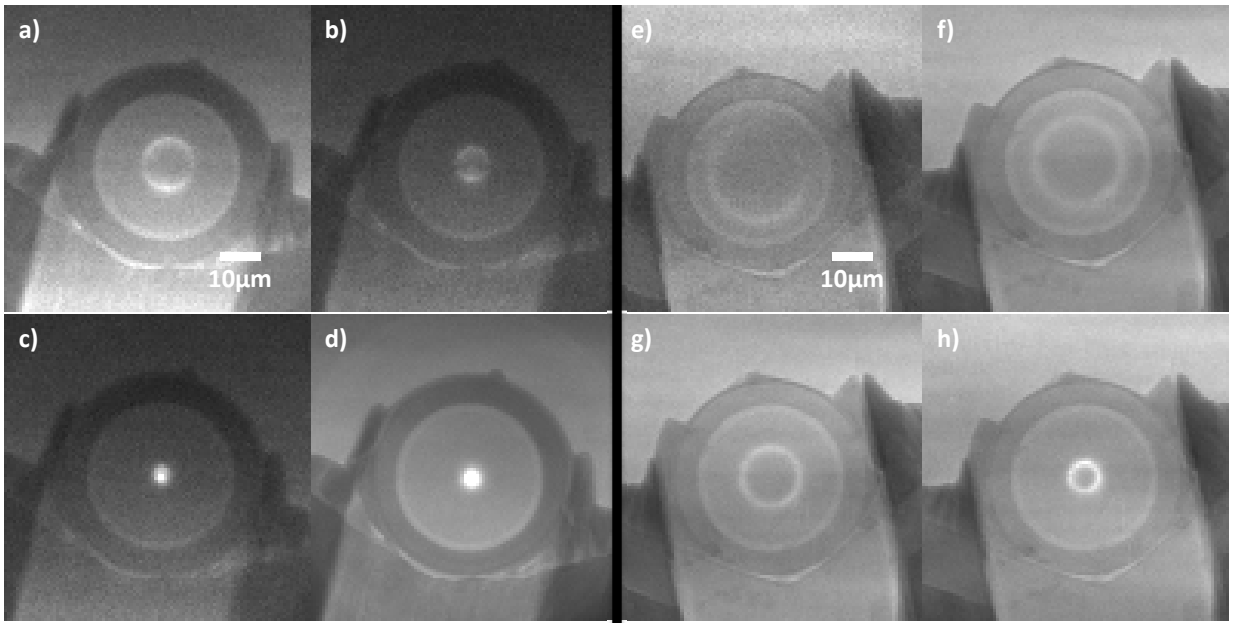

Figure 4.20: Qualitative characterization of the $\Delta r = 15$ and $\Delta r = 10\,nm$ zone plate in the hard X-ray regime. a) To d) $\Delta r = 15\,nm$ FZP and e) to h) $\Delta r = 10\,nm$ FZP.

possible way to create a symmetric focal ring. From figure 4.20 b) to d) FZP and camera have been approached until the focal distance of the lens has been reached. Figure 4.20 e) to h) shows the $\Delta r = 10\,nm$ FZP of the deposition series 10B. In figure 4.20 e) and f), the lens has been adjusted to form a symmetrical diffraction ring. In figure 4.20 g) and h) FZP and camera have been approached as close as possible. Due to the short focal length of the lens and the body of the camera, the focal distance cannot be reached in this configuration.

Table 4.5: Summary of all rotation angles for all zone plates necessary to achieve a circular focus ring and to achieve orthogonality between FZP and incoming beam.

name of zone plate	angle X-axis [°]	angle Z-axis [°]
35	0.6	0.6
15	-1.5	0.62
10A	-	-
10B	-0.4	1.1

The rotation angles which were necessary to create a complete diffraction ring and to bring the FZP in perpendicular condition to the incident beam for all zone plates are summarized in table 4.5. Contributions to the necessary rotation angle are for example: the bending of the TEM-grid, the ellipticity of the fibre and the leafing of the grid during the gluing process with the conduction silver paste. Especially the last contribution is very different for all gluing processes, wherefore these values are only to be seen as snapshot. With the zone plates of the deposition profile 10A, it was not possible to obtain a complete diffraction circle. To obtain an estimation of the diffraction efficiency of the zone plate, a horizontal intensity profile through the center of the diffraction spot in figure 4.18 h) with a length of 70 μm has been drawn and is shown in figure 4.21. The length of the line is sufficient to cover the glass substrate, the active zones of the zone plate as well as the area in the image where the light has not been attenuated by any medium except air. The diffraction efficiency (η) is defined as the ratio of the power of the beam diffracted into focus (P_{focus}) to the incident power of the beam reaching the zone plate ($P_{incoming}$) (equation 4.2).

$$\eta = \frac{P_{focus}}{P_{incoming}} \tag{4.2}$$

To obtain the power of the beam (P), the average intensity[1] ($\overline{I}$) at both locations has to be multiplied with the respective area (A) (equation 4.3)

$$P = \overline{I} * A. \tag{4.3}$$

To obtain the power of the incoming beam on the zone plate, the average background intensity ($\overline{I_b}$) has to be multiplied with the active area of the zone plate (A_{FZP}) (equation 4.4).

$$P_{incoming} = \overline{I_b} * A_{FZP} = 280 * \pi * (19^2 - 15^2)\mu m^2 = 119631.8 \tag{4.4}$$

[1]Intensity is defined as the flow of energy per unit area and unit time [65] (p. 50).

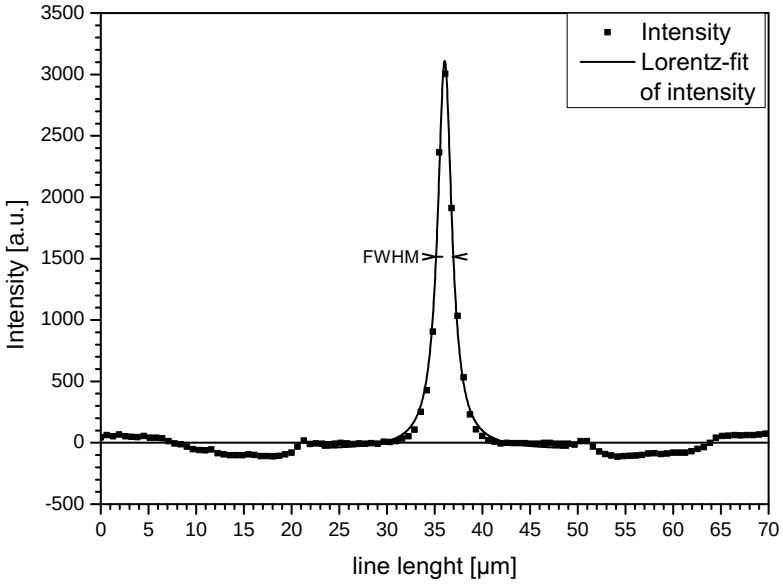

Figure 4.21: Intensity line profile along a horizontal line of 70 μm length through the center of the diffraction spot in figure 4.18 h). The peak has been fitted with a Lorentzian-curve.

The average background intensity has been measured in the area of the image outside the contour of the projection of the zone plate, where the light has not been attenuated by any medium and equals approximately 280 in arbitrary units. The active area of the zone plate is calculated by taking the difference in the squared outer and inner radii of the zone plate. This leads to a beam power on the zone plate of 119631.8. To calculate the beam power in the focus, the overall intensity distribution along the line profile has to be background corrected by subtracting the transmission of the glass core. Then, the center peak of the intensity profile is fitted with a Lorentzian-curve. The area of the focus is defined as FWHM (full width at half maximum) of the Lorentzian-curve for this calculation. The beam power in the focus is then given by (equation 4.5).

$$P_{focus} = \overline{I_f} * A_{focus} = \frac{I_f}{l_{focus}} * A_{focus} = \frac{4554.36}{1.8} * \pi * 0.9^2 \mu m^2 = 6438.6 \qquad (4.5)$$

The average intensity in the focus has been calculated by taking the integral below the Lorentzian-curve within the borders of FWHM of the focus and dividing it by the width of 1.8 μm. This yields an average intensity of 2530.2. The beam power in the focus then equals 6438,6. Finally, the ratio of both power values leads to a diffraction efficiency of

approximately 5.4 %, to be compared with a theoretical efficiency of 25 %, calculated with the CWT for a zone plate with the same area of active zones and the same thickness.

For a evaluation of the imaging properties of the zone plates, measurements were performed with the full field setup, presented in figure 3.9 in the imaging geometry presented in figure 3.8. This imaging geometry is different from the standard TXM setup, presented in figure 2.7, in several attributes. In the standard setup, object, zone plate and CCD-camera are on the optical axis and the zone plate creates a full image of the object, because its whole area contributes to image formation. In addition, the field of view of the CCD-camera can be much larger than in the present setup[2]. The special imaging geometry in this setup is hence a result of the preconditions, set by the applied components. Due to the glass core of the FZP, which does not contribute to imaging and the small field of view of the camera, sample and CCD-camera had to be used in off-axis geometry. The partial zone plate only creates a ring shaped, bright field image of that part of the object which is in front of the active zones. Therefore, the centre of the Au Siemens-star test pattern (X50-30-7 by Xradia) has been brought in front of the active zones of the FZP (see figure 3.8). Due to the small field of view of the camera, it has to be moved parallel to the optical axis into the opposite direction with respect to the test object to capture the image, created by the zone plate.

Images obtained in this geometry with the $\Delta r = 35\,nm$ FZP as objective lens in the full-field microscope are shown in figure 4.22 a) to d), which show a series of images of different parts of the Siemens-star test pattern. These images have been obtained with an exposure time of 120 s. The coordinate system for the movement has been defined in figure 3.8 with the positive Y-direction pointing down-stream, the positive Z-direction upwards and the positive X-direction into the image plane. The optical axis in the center of the setup represents 0 for X and Z and the intersection of their axes. To obtain images created from all areas of the zone plate, the Siemens-star has been moved in front of the left, right, upper and lower part of the zone plate. The camera has been moved into the opposite direction correspondingly. In figure 4.22 a) the test object has been moved 22 μm in -X and the camera 1.4 mm in +X-direction. In figure 4.22 b) the test object has been moved 18 μm in +X and the camera 1.4 mm in -X-direction. In figure 4.22 c) the test object has been moved 16 μm in +Z and the camera 1.2 mm in -Z-direction and in figure 4.22 d) the

[2]The TXM, installed at beamline U41 at BESSY II for example, offers 1300 pixels with a size of 20 μm per pixel and hence a field of view of $2.6 \times 2.6\,cm$.

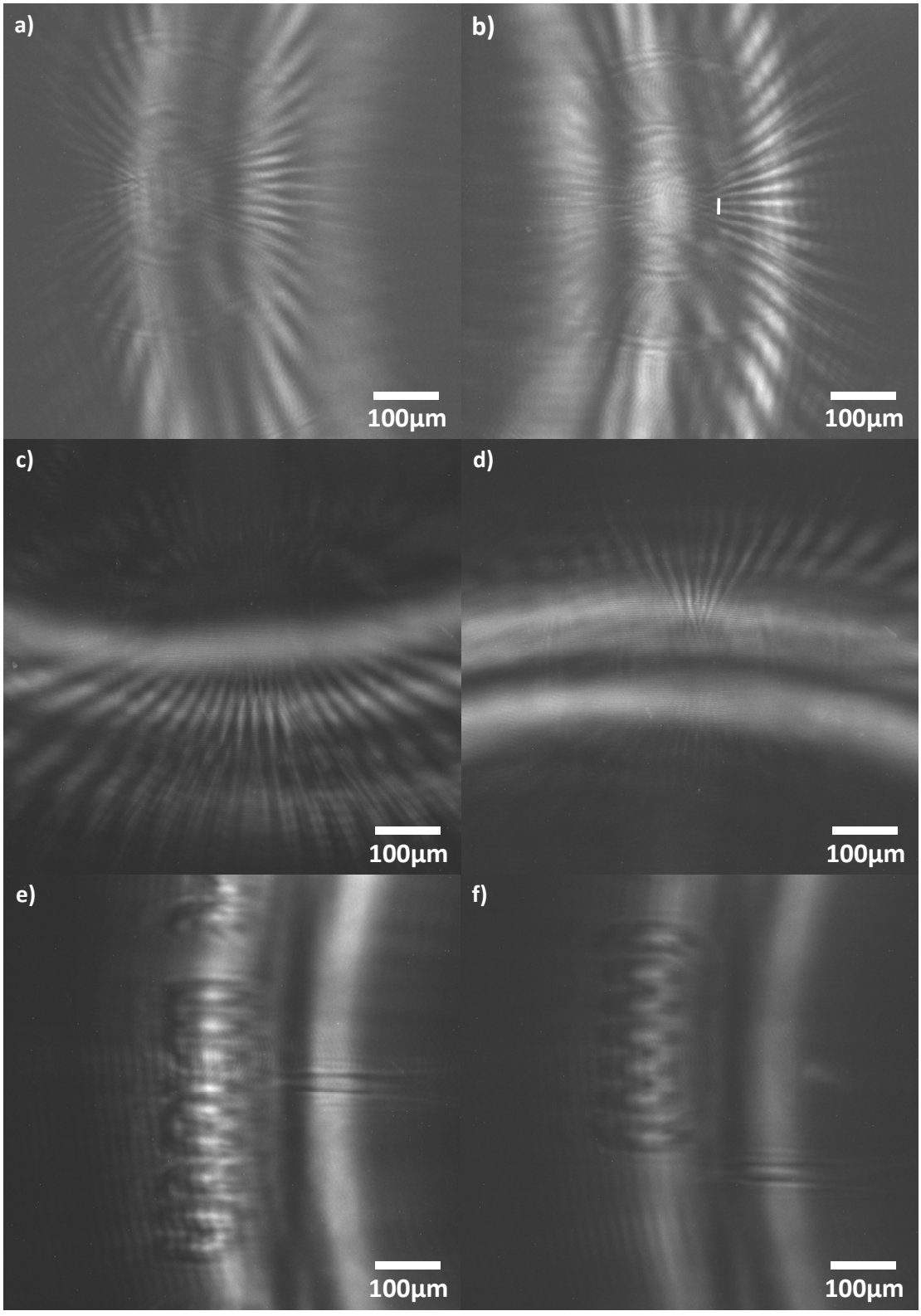

Figure 4.22: Full field X-ray images of the Siemens-star X50-30-7, a) to d) and f) obtained with 120 s, e) obtained with 300 s exposure time, at a magnification of ∼87. a) To d) show different parts of the Siemens-star, e) shows the word "width" and f) shows the word "(nm)". The line profile in b) has been used to quantify the resolution.

test object has been moved 16 μm in -Z and the camera 1.2 mm in +Z direction. All images show a fraction of a ring shaped bright field image of the Siemens-star. The width of this bright area roughly corresponds to the 4 μm thick coated area of the zone plate[3] whose zones contribute to image formation. In the bright area, the innermost and the second ring of the Siemens-star, together with its structures can be recognized. Due to the high coherence of the beam (coherence length: $10 \times 250\,\mu\text{m}^2$ H $\times$ V [105]), all structures originating from the test object are further modulated. These modulations can originate from other diffraction effects caused by interference of parts of the beam, diffracted by interfaces perpendicular to the beam direction and non diffracted parts of the beam. This effect is most visible in the innermost ring of the Siemens-star where the features can no longer be resolved and its centre part where no structures are present at all. To get a quantitative measure for the structure sizes which can be resolved in this full-field approach, a line profile along the vertical white line in figure 4.22 b) has been evaluated. Structures ≥ 120 nm can be resolved in this image. The resolvable structure sizes are much larger than the expected resolution of the FZP and also much larger than the minimum structure size of the Siemens-star of 50 nm. Figure 4.22 e) and f) show the words "width" and "(nm)", respectively. Figure 4.22 e) has been obtained with an exposure time of 300 s and figure 4.22 f) with 120 s. For both images, the camera position was 1.4 mm in +X and 1.5 μm in -Z-direction and the sample has been moved 40 μm in -X-direction. Also the values for the Z-direction of -0.99 and -1.0 μm are nearly identical. In both images the words are readable. As it is the case for the other images, further modulation effects are visible in the image, which are likely to originate from interference effects of diffracted and undiffracted parts of the beam.

[3]Calculated by measuring the distance in the image in pixels, dividing this value by the magnification and multiplying the result with the pixel size of 0.645 μm.

Chapter 5

Discussion

5.1 Manufacturing and quality of the deposited films

5.1.1 Quality of the deposition

The 35 nm FZP

Despite the theoretically possible atomic control of the layer thickness in ALD and the high quality of the films of the $\Delta r = 35\,nm$ zone plate, the deposition process still suffers from drawbacks, shown by the comparison of the deposited overall thickness from the upper and the lower part of the fibre of 4.15 and 4.29 μm, respectively and the targeted overall thickness of 4.08 μm in figure 4.9. Whereas the thickness of the Al_2O_3 layers of the sample form the lower part of the fibre closely follows the targeted values, all other layers show partially large deviations. All Ta_2O_5 layers are thicker than expected. One reason for this behaviour is an underestimated growth rate which was estimated as described in section 4.2.1 on trial samples of varying thickness of Ta_2O_5, deposited on silicon wafer pieces. The growth characteristics of Ta_2O_5 on Si however, appear to be different form the growth on Al_2O_3 in the multilayer system. Variations of the thickness of the layers during the long deposition could also be attributed to small instabilities of the reactor or of the adjacent parts, like the vacuum pump, the carrier gas supply or the heated $Ta(OEt)_5$ source. Other deviations from the ideal behaviour may be due to the refill of H_2O_2, which had to be performed during the deposition and the programming of new deposition sequences, for which the reactor chamber had to be vented and re-evacuated. The deviation of the thicknesses of films from the upper to the lower part can be attributed to a different horizontal position along the fibre, from which the TEM-samples of the upper

and the lower part have been prepared, which shows, that the ALD deposition did not occur homogeneously in the whole chamber. To shorten the overall deposition time, the process could be optimized in terms of purge times. A reduction of the purge time form 4 s to 1 s would lead to a shortening of the whole deposition process from about 126 to 86 h for the 35 nm FZP for example, and hence reduce the stability issues described above. A problem which arises with the reduction of the purge times is however the control of the completeness of the purging of the reactor from remaining precursor molecules and reaction by-products. The purge time required for the suspended fibre may also be different from that of a flat Si-substrate which can lead to an underestimation of the purge time if only tests on silicon are performed. A thorough optimization of all processes was not possible due to the limited availability of the deposition apparatus at the MPI of microstructure physics and the dedication of the device to various kinds of applications. VASE can only be applied to measure the thickness of flat specimens. Moreover, the lateral dimensions of the probe are several millimetres which leads to an averaging over this area. The very accurate measurement of the thicknesses deposited on the actual fibre is only possible by TEM, which requires a time consuming sample preparation and is therefore not suited to evaluate a large number of samples, which is necessary to efficiently optimize the process, because no *in-situ* monitoring is installed inside the ALD device. Furthermore, the evaluation of the zone thicknesses from the TEM images itself bears some uncertainties. Because the glass fibre is completely amorphous, no crystallographic axis (pole) of the substrate can be adjusted in the TEM and it is hence possible that the sample is not perfectly perpendicular to the beam and the individual layers are broadened by tilt. As the pole of the substrate serves as a reference, measurements of the upper and lower part of the sample are not completely comparable.

The 15 and 10 nm (10A) FZP

More pronounced problems with the deposition become visible in figure 4.10 for the $\Delta r = 15\,nm$ and the 10A zone plate. These depositions show severe quality issues. In the last part of the $\Delta r = 15\,nm$ zone plate (figure 4.10 a) and b)), it appears that some of the Al_2O_3 layers are completely missing in between the Ta_2O_5 layers. This regular occurrence of the same flaw may be a hint towards a mistake in the programming of the layer sequence of the last deposition session. Hence, care has to be taken that the number of cycles, loops and a possible decrement are inserted correctly into the control program of the ALD-device. During the deposition of the 10A zone plate (figure 4.10 c) and d)) two

periods occurred during which the deposition did not work reliably. For these periods, the Al_2O_3 layers are present but are significantly thinner than the Ta_2O_5 layers. This behaviour could be attributed to instabilities in the carrier gas supply or a malfunction of the dosing valve for the TMA-supply during a limited time. If the valve does not open correctly, not enough precursor can reach the fibre which can lead to a diminishing layer thickness.

The 10 nm (10B) FZP

On the contrary, the deposition of the 10B zone plate (figure 4.10 e) and f)) has worked correctly in terms of layer regularity and appearance, which is also confirmed by the TEM images in figure 4.11. Smeared out interfaces between the zones were mainly caused by the TEM sample preparation via FIB. The evaluation of the layer thicknesses and their comparison with the theoretical values in figure 4.12 showed a maximal deviation of $\leq 3\,\mathrm{nm}$ from the measured to the theoretical zone thicknesses and conclusively a deviation of the deposited overall thickness of $4.29\,\mu\mathrm{m}$ from the targeted overall thickness of $4.02\,\mu\mathrm{m}$, which resulted mainly from the evaluation of the high resolution TEM images. The main reasons for the problems encountered during the evaluation of the images can be attributed to the preparation of the specimen. The thinning of the sample with the ion beam has disturbed some of the zones by beam damage. Their inherently sharp interfaces have been smeared out and led to intermixture, which made it very complicated to distinguish between black and white layers due to a broad grey area. The 360 layer thicknesses have been measured in 47 images where each image contained 6 to 8 layers and the images had to be stitched to cover the whole zone structure by moving the sample. During this stitching, areas with sharp interfaces alternated with areas with smeared out interfaces which led to a largely varying measured thickness. As the TEM device was not equipped with a rotational holder, it was not possible to align the zones horizontally which inhibited the possibility to move the sample horizontally to avoid measuring in disturbed areas. Another problem was the varying thickness of the whole TEM-sample over the large overall thickness of $4\,\mu\mathrm{m}$ which can lead to a smear out or a grey area at the interface due to an overlap of black and white layers over a large projection depth. This causes problems for the distinction of the individual layers and their correct measurement.

Summary

The problems encountered during the deposition and possible ways of solving them can be summarized as follows: The whole deposition process requires a further optimization and thus a closer investigation of the processes involved, which was not possible during this thesis, as the work has been done in collaboration with the MPI in Halle (Saale) and the access to the ALD device was hence limited. A general concern is the long-term stability of the process lasting several days, wherefore the shortening of the cycle times is of great importance. In addition, an accurate estimation of the growth rate is absolutely necessary, for which the growth of the zone materials on top of each other instead of Si should be thoroughly studied. A huge benefit would hence be the possibility to measure the thickness of the growing films *in-situ* during the deposition.

As the first FZPs ever made with this preparation technique the obtained results are nevertheless encouraging, shown by the comparison of the microscopic appearance of the zone structures and the optical performance of these zone plates with standard EBL and sputter-sliced zone plates.

5.1.2 Comparison with other FZP manufacturing techniques

A comparison of the zone structures, manufactured by the new method of ALD deposition and FIB sectioning and thinning, with the structures of zone plates made by the "sputter-sliced" and the EBL technique, shows some benefits of the new approach.

Comparison with the "sputter-sliced" technique

A SEM image of the $\Delta r = 35\,nm$ FZP is compared with SEM images of zone structures of multilayer zone plates manufactured by sputtering in figure 5.1, where figure 5.1 a) shows an overview image of the $\Delta r = 35\,nm$ FZP, made by ALD and FIB. The dark layers are Al_2O_3 and the light grey layers are Ta_2O_5. This image shows the same characteristics as figure 4.8 b): the zones are regularly spaced and show sharp interfaces, their boundaries are well defined with little to no intermixture between the zones. Even the large overall layer thickness of $>4\,\mu m$ does not lead to roughness accumulation and therefore even the zones deposited lastly present satisfying quality. The thick light grey layer on the far left side is the final Ta_2O_5 protection coating. Figure 5.1 b) has been taken form reference [123]. In this image, the black rings are Al and the white rings are Cu, deposited onto a

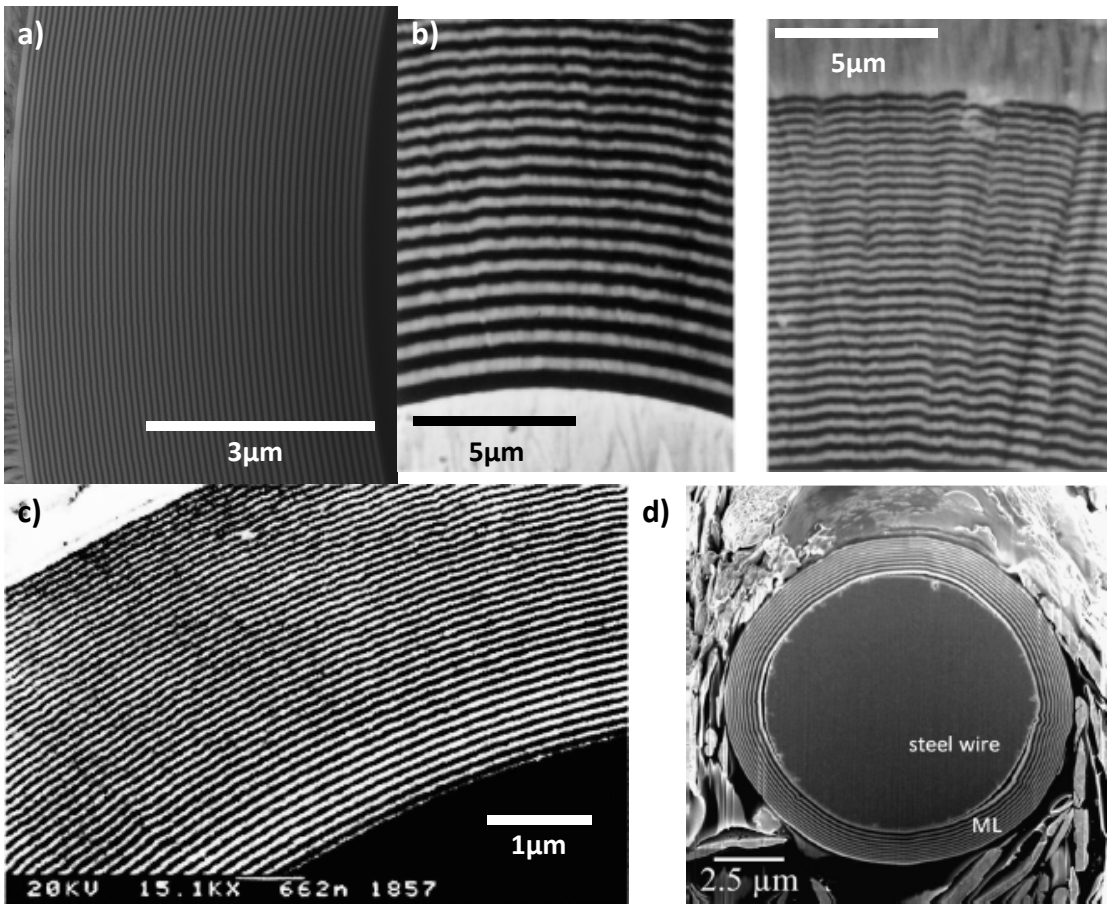

Figure 5.1: Comparison of SEM micrographs of the zone structures of FZPs made by following our new manufacturing method with other multilayer FZPs from the literature: a) FZP with $\Delta r = 35\,nm$, according to our new method. b) and c) sputter-sliced FZPs and d) PLD-deposited FZP, found in the literature (see text for references).

Au wire by DC magnetron sputtering with thicknesses ranging from 400 nm on the inside to 190 nm on the outside. Here, roughness accumulation during deposition is well visible. While the first layers on the lower left side of figure 5.1 b) show sharp interfaces, the last layers on the upper right side of figure 5.1 b) show a very wavy appearance. No statement has been given by the authors on the target thicknesses of the individual layers, so no judgement on their accuracy can be made. The images in figure 5.1 c) and d) have been taken from reference [108] and [152], respectively. The material system in figure 5.1 c) is NiCr - SiO_2 and the layer thicknesses range from 50 to 30 nm. This image shows the same characteristics as figure 5.1 b) with the first layers showing well defined, and the last layers showing very rough interfaces. The material system in d) is ZrO_2 - Ti, where 20 layers with thicknesses from 115 to 85 nm were deposited with PLD. Despite the high quality and the "self-smoothing" effect which is claimed by the authors for PLD deposited layers, the adhesion to the wire substrate is bad, only few layers with large thicknesses have been deposited and the quality of the substrate is not suited for optical applications. Zone structures of multilayer FZPs deposited with SPCVD are presented in [126, 127].

Comparison with EBL-based techniques

The comparison with SEM images of zone plates manufactured with electron beam lithography shows, especially when it comes to side views, that these zone plates also suffer from problems during the fabrication, which are presented in figure 5.2, where figure 5.2 b), taken from reference [89], shows the polymer galvanoform of a Ni FZP, made with a 3-layer process of EBL, RIE and electrodeposition in side view. The structures on the left have 50 nm period and an aspect ratio of 7 : 1, the structures on the right have 40 nm period and an aspect ratio of 8.75 : 1. Whereas the structures on the left show a constant width from top to bottom, the structures on the right show undercut at the bottom due to scattering effects in the resist and the substrate during the EBL exposure. As the displayed structures have not yet been plated with Ni, they do not resemble the final zone plate. Figure 5.2 c) taken from reference [102], shows the zone structures of a gold zone plate, made with the double patterning technique, in plane view. The zone structures show a period of 30 nm with an aspect ratio of 5 : 1. The images exhibit two common flaws of electroplated zone plates: The zone structures are complete in areas where the zones are wide, but interrupted in areas where the zones are fine. This behaviour is well visible in the inset and has a diminishing effect on the FZP efficiency. A second problem

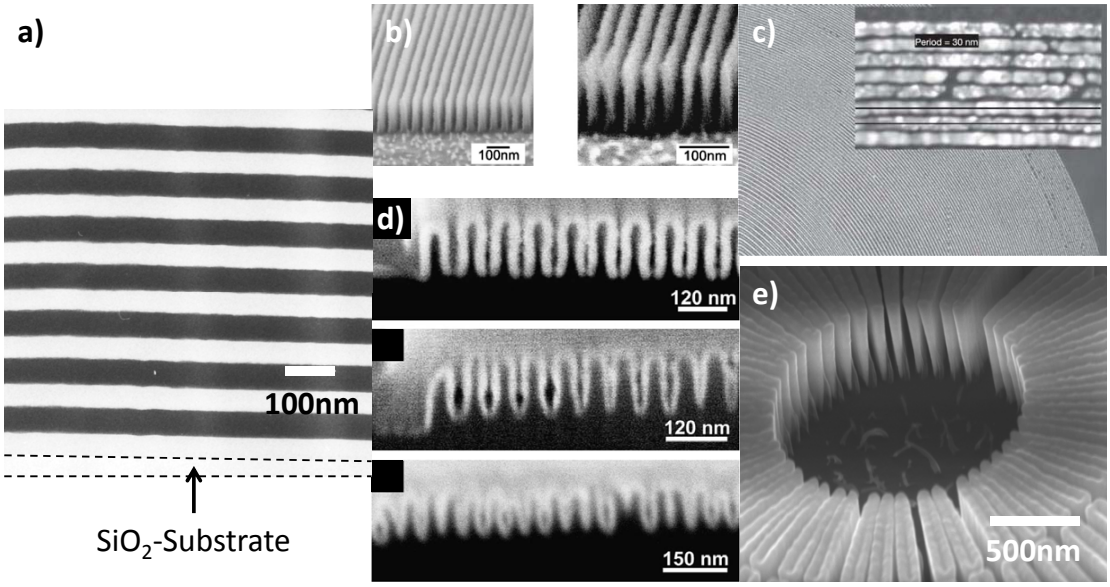

Figure 5.2: For comparison a) shows a TEM image of the $\Delta r = 35\,\mathrm{nm}$ FZP, manufactured with our new technique. All other images show SEM micrographs for the illustration of problems with the fabrication of zone plates and test structures with EBL techniques. b) FZP, 3-layer process; c) FZP, double patterning; d) FZP, zone-doubling; e) Test object (X50-30-7), single layer process. a) To c) have been taken from the literature (see text for references).

which often occurs with electroplated zone plates is overplating. If the plating process is conducted longer than necessary to completely fill the plating mould, the overplated metal leads to a broadening of the zones and hence slanted zone boundaries. Figure 5.2 d) taken from reference [8], shows the zone structures of a Ir coated silicon zone plate, made with the zone-doubling technique, in cross section. The FZPs show outermost zone widths of (top) 20 nm, (middle) 15 nm and (bottom) 12.5 nm with an aspect ratio of 15 : 1 for 12.5 nm zone plate. Despite the high resolution of 9 nm that these zone plates can provide, it is clearly visible, that the zones have slanted side walls and that the RIE process has not produced a rectangular zone profile, which leads to a virtual broadening of the zones in the projection. In addition, the iridium coating at the top and the bottom of the zones leads to a reduction of the diffraction efficiency. Figure 5.2 e) shows the Siemens-star test object X50-30-7 in side view. The finest features have 50 nm width and an aspect ration of 13 : 1. In this image, the problems encountered when zone- or teststructures, suitable for the hard X-ray regime are produced with EBL, become apparent. In addition to the need for an increase in structure width, high structures lead to a very pronounced undercut at the bottom and hence very slanted side walls, due to the long exposure time (high required dose) and scattering effects during the EBL process. ALD deposited zone plates do not suffer from slanted zone boundaries, because the coating is conformal over the whole length of the fibre as shown in figure 5.2 a) and the aspect ratio is independent of the zone width .

All these results clearly show, that the layer quality is superior for zones plates deposited with ALD, if the process is running reliably (as discussed above). Furthermore, the sectioning of conformally coated fibres to obtain the zone plate prevents slanted zone boundaries and offers high aspect ratio zone plates with fine outermost zone widths. Two drawbacks of the technique are however the accumulation of zone displacement errors caused by deviations of the deposited to the theoretical zone thicknesses and the need for *in-situ* thickness control for accurate growth rate determination. Nevertheless, the method shows a high potential for further experiments.

5.2 X-ray optical performance

5.2.1 Soft X-ray regime

No examples have been found in the literature that any kind of multilayer zone plate has ever been used in the soft X-ray regime ($\leq 1500\,\mathrm{eV}$). This shows, that the newly developed process, consisting of multilayer deposition via ALD and sectioning and thinning via FIB has been, for the very first time, successfully used to perform imaging with multilayer zone plates in this energy range (see section 4.4.1).

With the $\Delta r = 35\,\mathrm{nm}$ zone plate it was possible to obtain diffraction limited focusing and thus imaging in the soft X-ray regime below 1500 eV in the SXM by resolving features below 39 nm in a nickel and a gold Siemens-star test pattern. A slight degree of astigmatism is present in the images of figure 4.14 and 4.16, which is also manifested in different focal lengths for horizontal and vertical features. Several origins of astigmatism are possible for the applied zone plates. First of all the TEM-grids on which the zone plates were prepared may suffer from bending, caused by their handling. This is especially probable for zone plates on Cu-grids, which are much softer than the grids made of molybdenum which is a much more rigid material. Bending can also be introduced during the glueing procedure, when the grid is partly floating on the conduction silver paste, which prevents that it is glued exactly flat on the holder. A second source of astigmatism can be the ellipticity of the fibre substrate. This property has been measured to be below an accuracy of 50 nm in TXM (below the accuracy of the measurement). According to literature the roundness of the substrate should be better than $0.5 \times \Delta r$ [153] which is 17.5 nm in this case. Therefore, the substrate cannot be excluded as a source for astigmatism. Other possible aberrations, like coma and spherical aberration can be attributed to different layer thicknesses on the upper and the lower part of the fibre (nonconcentricity), and differences in layer thicknesses compared to the zone plate design rule (radial displacement), respectively [153]. According to Vladimirsy or Attwood the placement accuracy for the zones has to be better than $1 \times \Delta r$ or $0.25 \times \Delta r$ [153, 6], respectively to avoid these aberrations. The maximum deviations for the individual zone thicknesses are 8 and 13 nm for Al_2O_3 and Ta_2O_5 zones, respectively for the layers measured on the upper part of the fibre with the $\Delta r = 35\,\mathrm{nm}$ zone structure. As the Ta_2O_5 layers are all thicker, and the Al_2O_3 layers are all thinner than desired, the effects seem to cancel each other out in this case. For the layers of the lower part of the fibre, the

Al_2O_3 layers follow the theoretical thickness quiet closely, whereas the Ta_2O_5 layers are all thicker than desired, which leads to a total deviation larger than $1 \times \Delta r$ for the placement accuracy. The total displacements of layers from the upper and the lower part of the fibre to the targeted value equal 72 and 212 nm, respectively. Nevertheless it was possible to perform diffraction limited imaging with different $\Delta r = 35$ nm zone plates which leaves room for speculation about the applicability of theoretical restrictions to these zone plates.

Although the obtained results were encouraging for the $\Delta r = 35$ nm zone plates, the drawbacks suffered with the $\Delta r = 15$ nm and the 10A zone plate show, that accurate process control, especially in the ALD, is mandatory for good imaging properties. With the $\Delta r = 15$ nm zone plate, where the outermost zones do not follow the zone plate design rule but show very thick Ta_2O_5 layers in combination with few regular Al_2O_3 layers it was not at all possible to obtain a focus in the STXM. This may be due to the fact that the radiation transmitted through the Al_2O_3 does not interfere constructively at a focus point, but is diffracted into other directions where the radiation is not usable for imaging, or to a misalignment of the FZP in the beam (as a similar FZP creates a focal spot in the hard X-ray regime (see below)).

With the 10A zone plate, the situation is only slightly better. A focus could be obtained in the STXM but the resolvable feature size of > 100 nm was much larger than the outermost zone with of 10 nm. The reason may, also in this case, be the irregularities in the layers during the deposition process. In the two areas where the transparent Al_2O_3 zones do not show the thickness dictated by the zone plate design rule, their diffraction behaviour is different. Very thin zones lead to shorter focal lengths and the rays, originating from these zones, may lead to spherical aberration and thus a broadening of the focus. In addition, the zone plate design rule was approximated by periods of constant zone widths, for the deposition of the $\Delta r = 10$ and 15 nm zone plates in contrast to the varying decrement applied for the $\Delta r = 35$ nm zone plate (see appendix B). The constant zone widths over a certain period of zones can also contribute to the broadening of the focus by diffracting the light as a beam of constant or diverging width, in contrast to a focus, in analogy to the side maxima of a diffraction grating of constant line density. The pure influence of the difference in the deposition strategies on imaging cannot be evaluated until experiments with the 10B zone plate in the STXM have been performed which was not possible in the time frame of this thesis due to the limited availability of beam time at

MAXYMUS.

5.2.2 Hard X-ray regime

All attempts to implement multilayer FZPs in X-ray microscopy have so far been performed in the hard X-ray regime. Two experiments were performed for this thesis to characterize the zone plates: The focusing of nearly parallel X-rays onto a CCD-camera and full-field X-ray imaging with the zone plate as objective lens (see section 4.4.2).

Qualitative focusing of the FZPs

With the focusing experiments of parallel radiation onto the CCD-camera it was possible to achieve symmetrical diffraction rings for the $\Delta r = 35$, 15 and 10 nm (10B) zone plates via appropriate adjustment of the rotation angles around the X- and Z-axis. The necessity for this adjustment is similar to the occurrence of astigmatism in the STXM-images: bending of the TEM-grid, floating of the grid on the conduction silver paste, used to glue it to the holder, and possible ellipticity of the fibre substrate. As the gluing procedure and hence the bending of the grid by handling it are not completely reproducible, the values of the tilt angles given in table 4.5, needed to adjust the FZP perpendicularly to the beam, can only be seen as momentary values. Despite the nominal resolution of the applied zone plates of ≤ 35 nm it was not possible to focus all the radiation into just one pixel with a size of 0.645 μm of the CCD-camera. The line profile yielded a focal spot size of 1.8 μm (FWHM) (figure 4.21) for the $\Delta r = 35$ nm zone plate, which is slightly larger than the resolution of the camera of two pixels (1.3 μm). This shows the limitation of this experiment to determine the resolution of the FZP, as we have seen that the same FZP shows 120 nm resolution in the hard X-ray regime in full-field microscopy (see below) as well as below 39 nm resolution in scanning microscopy in the soft X-ray regime (see above). The FWHM of the focus could perhaps be reduced by using an OSA to reduce the background near the focus, by blocking radiation diffracted from zones which do not show the exact zone width and placement accuracy and thus have a different focal length. If the radiation, originating form these zones, hits the screen convergently or divergently, both can lead to significant broadening. Nevertheless, the expected resolution of 35 nm could not have been evaluated with this test anyway, even under perfect conditions, due to the large pixel size of the camera.

In the focusing test of the $\Delta r = 15\,nm$ zone plate it turned out that the problems during the deposition also have a large impact on the focusing performance in the hard X-ray regime. In contrast to the STXM experiments in the soft X-ray regime, where no focus could be obtained at all, it was possible to achieve a symmetrical diffraction ring. The intensity of the ring was however smaller than in the case of the $\Delta r = 35\,nm$ zone plate, and its distribution showed interruptions as well as some kind of halo (figure 4.20 a) to c)), which can, most likely, be led back to the irregularities during deposition. The determination of the focal spot size as FWHM of the intensity line profile and the calculation of the diffraction efficiency was therefore omitted.

The diffraction ring for the FZP 10B (figure 4.20 e) to f)) shows sharper boundaries than the $\Delta r = 15\,nm$ zone plate which is in agreement with the well defined zone structure presented in figure 4.10 e) and f). Due to the short focal length is was however not possible to bring the FZP close enough to the CCD-camera to achieve a focal spot. Therefore, the spot size in FWHM and the diffraction efficiency could not be determined. With the 10A zone plate it was not possible to achieve a symmetrical diffraction ring, which is also attributed to the problems during deposition. A comparison of the focusing experiments with the $\Delta r = 10$ and $15\,nm$ zone plates with the STXM results also clearly shows, that the behaviour of the same zone plates can be very different at different X-ray energies.

The method to focus parallel radiation onto a CCD to evaluate the diffraction properties of a zone plate can also be found in the literature. A collection of results is presented in figure 5.3, where figure 5.3 a) and b) have been taken from reference [110] and [109], respectively. figure 5.3 a) shows the intensity distribution and the corresponding intensity profile through the focus of a NiCr - SiO_2 sputter-sliced zone plate with 188 zones and an outer zone width of $\Delta r = 30\,nm$, which has been tested at several energies. The best focusing was obtained at $19\,keV$ beam energy, whereas the lens was designed for $4\,keV$. The estimated spot size was 2-3 μm with the camera having a resolution in the same range. In this example, the glass core of the FZP is nearly transparent to the $19\,keV$ X-rays and the brought tails of the focal spot can hence be attributed to both, aberrations of the lens and transmission of undiffracted radiation through the glass core. Similar to the $\Delta r = 35\,nm$ ALD zone plate described above, the measured focal spot size of 2-3 μm in this experiment is much larger than expected for a zone plate

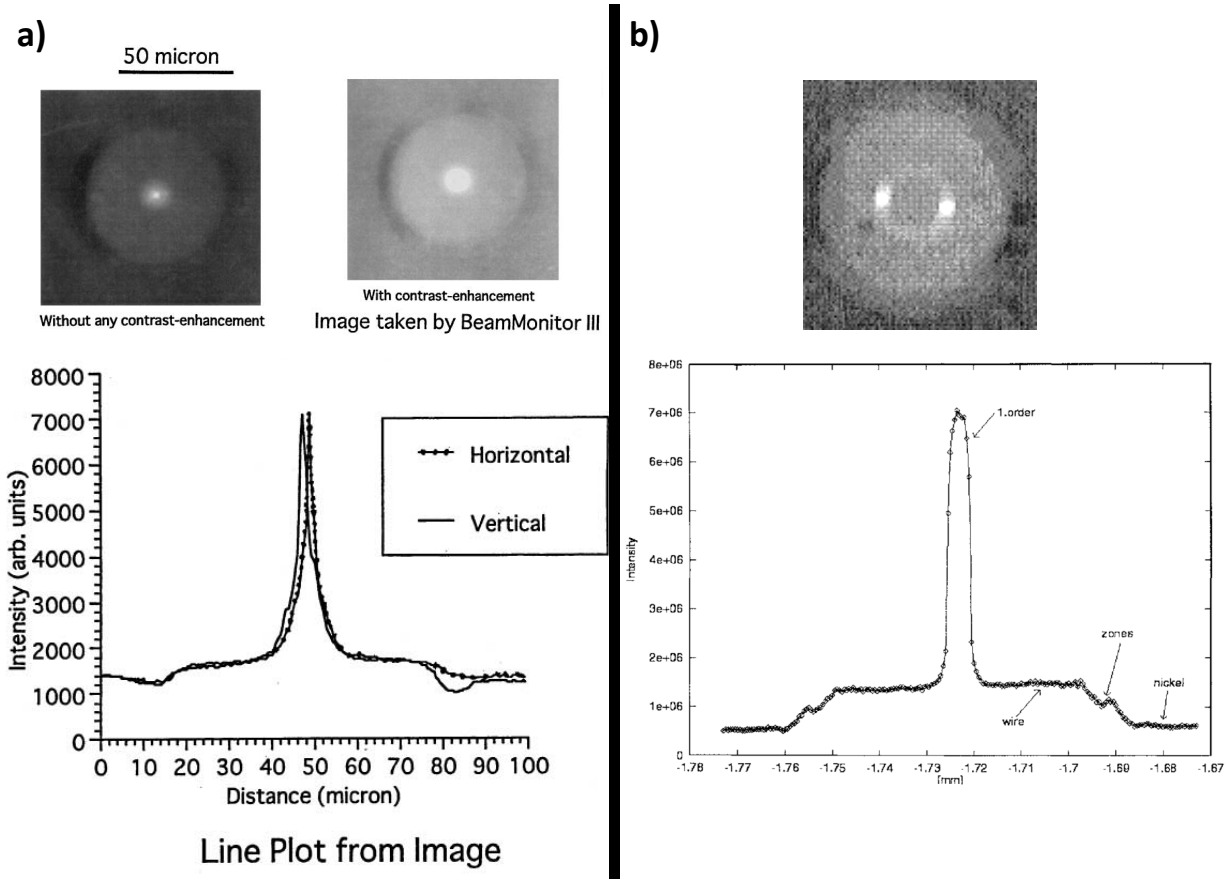

Figure 5.3: Two examples found in the literature (see text for references) for a NiCr-SiO_2 sputter-sliced zone plate, where parallel hard X-rays have been focused onto a CCD-detector at different energies.

with $\Delta r = 30\,nm$. Another example of a focusing test with a FZP in the hard X-ray regime in figure 5.3 b) shows the intensity distribution and the corresponding intensity profile through the focus of a NiCr - SiO_2 sputter-sliced zone plate with 365 zones and an outer zone width of $\Delta r = 16.9\,nm$ in defocused condition at 4.1 keV beam energy. The diffraction ring of this zone plate is not symmetrically bright, but consists of two very bright spots, accompanied by a less bright rest of a ring. This is in analogy to figure 4.18 b) where the rotation angles to bring the FZP in perpendicular condition to the incoming beam have not yet been optimized. In the setup used for their test, no possibility exists to adjust the angle between beam and FZP and the diffraction ring will thus stay non symmetric. The intensity profile has been obtained by scanning a 5 μm pinhole over the first order diffraction spot. A resolution limit of 0.8 -1 μm is claimed for this zone plate which is again much larger than the expected resolution for a $\Delta r = 16.9\,nm$ zone plate. Comparisons of the experiments performed in this thesis with the literature show, that the focusing of parallel light onto a detector is in general only suited to get a qualitative impression of the focusing capabilities of the zone plate. Due to the generally large resolutions of the applied detectors and measured spot sizes much larger than the outer zone width of the FZP, this method is not suited to characterize the zone plates in terms of their ultimate resolution. Therefore, imaging methods in the hard X-ray regime have also been applied in this thesis as well as in the literature to test the zone plates.

Full-field microscopy

To investigate the imaging properties of the zone plates more closely, the $\Delta r = 35\,nm$ FZP has been used as an objective lens in an open full-field setup, where features of a Au Siemens-star test pattern $\geq 120\,nm$ could be resolved (see section 4.4.2). One main problem of these experiments, besides the special imaging geometry, required through the narrow area of active zones of the FZP, is the high coherence of the beam. A highly coherent beam creates speckles and other interference effects in the images, which are superimposed on the modulation caused by the actual structures of the test object. These effects are clearly visible in all images of figure 4.22. To counteract these effects, the condenser in a TXM is often wobbled (in the case of a capillary) [154] or rotated [155] with a high frequency, to achieve a homogeneous illumination and to break the coherence of the beam during the exposure. Due to the static mounting of the condenser in our setup, it was not possible to perform condenser wobbling in these experiments. Another problem

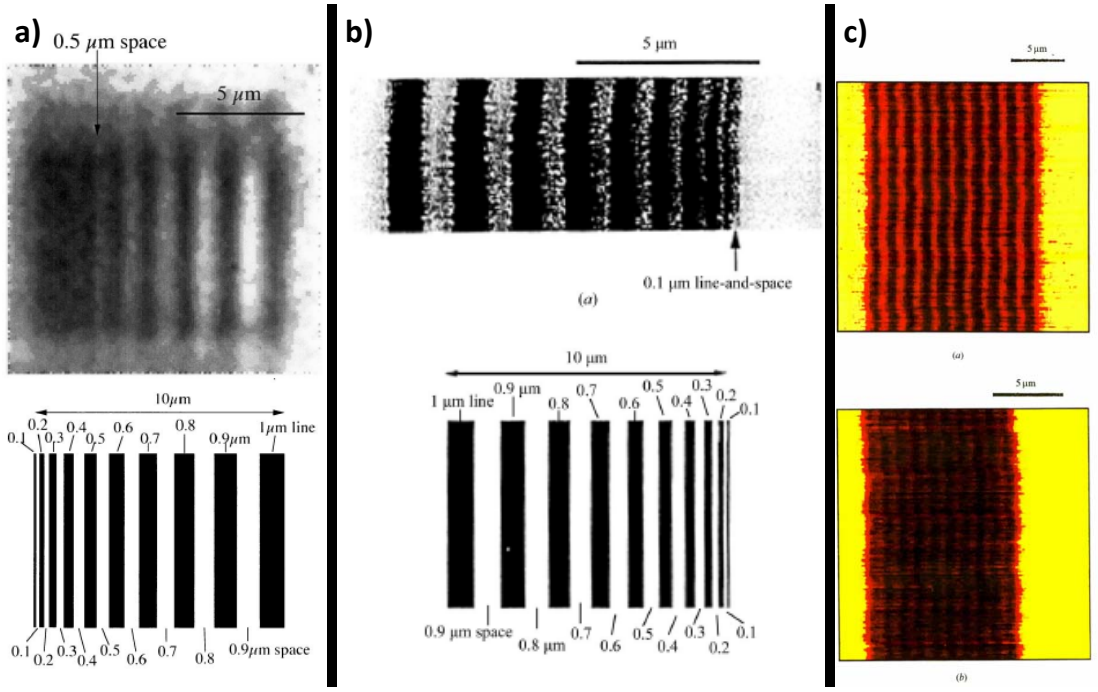

Figure 5.4: Examples found the literature (see text for references) to test the imaging capabilities of multilayer zone plates in the hard X-ray regime. a) Full-field imaging, b) and c) scanning imaging.

is the inhomogeneously illuminated area in the bright field images. This inhomogeneity could be caused by areas of FZP which direct the diffracted light into other directions than the rest of the FZP. The already discussed radial displacement of the zones and deviations from the ideal zone thicknesses may be accountable for this.

Examples for imaging experiments with multilayer zone plates can also be found in the literature (figure 5.4). The images in figure 5.4 a), b) and c) have been taken from reference [113], [156] and [124], respectively. Figure 5.4 a) has been obtained as full-field image with a sputter-sliced Cu - Al zone plate, with an outermost zone width of 250 nm and 50 zones as objective lens at 25 keV beam energy. A resolution of 500 nm has been measured with a Ta test object of 500 nm thickness and an exposure time of 240 s. Despite the long exposure time the contrast in figure 5.4 a) is very bad and especially the fine features can hardly be distinguished. A diffuser to break the high coherence of the beam has been used in this setup to avoid speckle formation which was very prominent at first. The use of a diffuser in our setup (described in figure 3.9) may have also led to a more homogeneous illumination and especially to the avoidance of additional distracting diffraction effects which made the

determination of the resolution in the full-field images of this thesis complicated. Figure 5.4 b) and c) are examples from the literature of scanning experiments in the hard X-ray regime to evaluate the resolution of zone plates. Figure 5.4 b) has been obtained with a sputter-sliced Cu - Al zone plate, with an outermost zone width of 100 nm and 50 zones at 12.4 keV beam energy. The test pattern was similar as in figure 5.4 a). The exposure parameters were a dwell time of 0.4 s/pixel and a step size of 62.5 nm/pixel. Despite the long dwell time, the contrast of the image is low, but enables the identification of 100 nm wide features which corresponds to the outer zone width of the zone plate. Another example of scanning imaging is presented in figure 5.4 c) where a sputter-sliced Ag - C zone plate, with an outermost zone width of 250 nm and 50 zones has been tested at 8.54 keV beam energy. The exposure parameters were a dwell time of 0.2 s/pixel and a pixel size of 200 nm for the upper and 150 nm for the lower image. Features of 900 and 600 nm width of a 1 μm thick gold pattern could be resolved in this experiment in the upper and the lower image, respectively. The scanning experiments of figure 5.4 b) and c) show, that scanning X-ray microscopy is a promising test technique, also in the hard X-ray regime where the zone plate in figure 5.4 b) showed diffraction limited resolution. The use or construction of a SMX for the hard X-ray range, especially if it makes use of the precision gained with interferometer control, together with the development of high resolution focusing optics with the new technique of ALD deposition and FIB sectioning and thinning would allow very efficient scanning hard X-ray microscopy.

Chapter 6

Summary and outlook

6.1 Summary

The goal of this thesis was the introduction and implementation of a new production method for Fresnel zone plates. The most popular methods for FZP production applied to date, do either involve structuring processes by EBL, or rely on the physical deposition of two materials with a very different refractive index on a longish substrate and its mechanical sectioning and thinning. In contrast, the methods applied in this thesis are the deposition of Al_2O_3 as a transparent and Ta_2O_5 as an absorbing material in an atomic layer deposition process onto a glass fibre and the sectioning and thinning of the coated fibre by focused ion beam to form the Fresnel zone plate. The coating with ALD shows several advantages over physical techniques like: chemical bonding between layers and substrate, high conformality and hence the avoidance of a rotation of the substrate, the controllability of the layer thickness in the atomic level under ideal process conditions, combined with the possibility to deposit very thin films and a high layer quality in terms of sharp interfaces and negligible accumulating roughness. The sectioning and thinning with FIB shows several advantages over mechanical preparation techniques like: the accessibility of a wide range of FZP thicknesses from a few hundred nanometers to a few tens of micrometers, facilitating the production of zone plates for the soft, as well as the hard X-ray regime, very clean cuts, not showing any scratches or other deformations on the surface and the possibility to select precisely from which location the zone plate shall be prepared.

With these techniques, zone plates with an outermost zone width of $\Delta r = 35,\ 15$

and 10 nm, the last with two different deposition schemes (10A and 10B) have been prepared as partial zone plates where the last 4 μm were deposited onto a 30 μm diameter glass fibre and thus created FZPs with a total diameter of 38 μm. The zone plate with $\Delta r = 35$ nm and the 10B both showed excellent layer quality in the SEM and TEM, in terms of zone appearance and interface roughness in areas which were not undisturbed by the TEM-sample preparation process. Both zone plates suffered however from radial displacement due to deviations of the deposited and the theoretical overall thickness. The $\Delta r = 35$ nm FZP showed a maximum deviation of 13 nm between the layer thicknesses measured in TEM images and the theoretical zone thicknesses. The thicknesses of the layers of the 10B zone plate showed a scattering of ≤ 2 nm around the mean value due to disturbances of the zone boundaries by the TEM sample preparation via FIB and a large deviation from the theoretical thicknesses. The $\Delta r = 15$ nm and 10A zone plate both showed flaws in their zone spacing and thickness in the SEM, originating from problems during the deposition. These abnormalities in their zone structure affected their optical performance.

The zone plates were tested in the SXM MAXYMUS at BESSY II in the soft, and at the microoptics test bench of the ID6 beamline at the ESRF in the hard X-ray regime. In images obtained in the SXM with the $\Delta r = 35$ nm FZP as focusing element, features below 39 nm in a nickel and a gold Siemens-star test pattern could be resolved at 1150 and 1496 eV beam energy, which corresponds to diffraction limited resolution. For the very first time, multilayer zone plates could be used as focusing elements in the soft X-ray regime, in these experiments. With the $\Delta r = 15$ nm FZP no focus could be found in the SXM. With the zone plate 10A, only features over one order of magnitude larger than the outermost zone width could be resolved most probably due to the irregularities in the zone structure. All experiments in the hard X-ray regime were performed at 8 keV beam energy. The $\Delta r = 35$ and 15 nm, and the 10B zone plate could successfully be used to focus nearly parallel radiation onto a CCD-camera and achieved circular diffraction rings by adjusting the rotation angles around the Z- and X-axis. Also in this case, the flaws in the zone structure negatively influenced the performance of the $\Delta r = 15$ nm and the 10A zone plate. The former showed some kind of halo around the actual diffraction ring, which was also not homogeneously bright. With the latter it was not possible at all to achieve a symmetrical diffraction ring. For the $\Delta r = 35$ nm zone plate, a focusing efficiency of 5.4 % has been calculated from an intensity line profile. This FZP could also

be used as objective lens in a full-field TXM setup, where features $\geq 120\,\mathrm{nm}$ could be resolved in a Siemens-star test pattern which is lower than the resolution expected for a FZP with $\Delta r = 35\,\mathrm{nm}$. The interpretation of the images is however problematic, due the high coherence of the beam which led to additional diffraction effects and the need to use off-axis imaging geometry due to the small active area of the zone plate of $4\,\mu\mathrm{m}$ and the small field of view of the camera.

After these successful first tests, the following section shall give an outlook on future possibilities based on the presented approach for FZP production.

6.2 Outlook

In the last section, the techniques and results of this thesis have been summarized. These results encourage further development of this approach and give rise to new ideas for the future concerning many aspects of the process:

First of all, new material combinations, for example containing SiO_2 (see section 4.1) should be investigated in terms of theoretical diffraction efficiency and, even more important, their feasibility in ALD. Related to the feasibility of new ALD processes, the existing processes have to be further improved in terms of short cycle times, precise predictability of the growth rate and long-term stability, as the microscopic investigation clearly showed and which was not yet possible due to the limited access to the ALD-device.

A second very important aspect is the search for other suitable substrates. Glass fibres offer a low surface roughness, a good reactivity of the surface for the ALD process as well as a high accuracy in terms of roundness, which should be measured in the future in the accuracy of the outermost zone width. They are however brittle and can therefore only be cut to very thin slices by FIB, at the moment. Fibres with larger diameters are favourable, because they offer longer focal lengths which simplifies their usage in the SXM in the soft X-ray range. With more flexible fibres, for example polymers, other sectioning techniques like microtomy may be used, which would be much faster than the preparation by FIB. High temperature stable polymers seem to be possible candidates for such attempts, because the current deposition temperature of 250°C is moderate. On the other hand, the combination of the very conformal coating by ALD and the localized

cutting by FIB offers many possibilities for the use of other substrate geometries. Possible candidates are conical substrates presenting an angle that full-fills the *Bragg*-criterion between the incoming beam and the zones, to enhance the efficiency as described in [75], or spheres which present a defined curvature for the same purpose.

A whole different idea is the use of hollow substrates, like capillaries or etched holes, which are coated by ALD on the inside. This would result in very high quality outermost zones, because they are deposited as first layers, directly onto the very smooth side wall. This effect is exploited for MLLs on flat substrates. First attempts of this approach at the beginning of this work have not been successful, so that the pursuit of this attempt requires deep fundamental investigations of all processes involved.

The rush for very fine resolutions below 10 nm can be a real advantage for ALD zone plates in the future, as ALD is capable to produce very thin films. Outermost zone width of ≤ 10 nm will definitively be a target for future depositions. Due to a decrease in efficiency and focal length, these developments have to be accompanied by the application of new substrates, as described above.

Very different test techniques have so far been applied to evaluate the optical performance of the produced zone plates: SXM in the soft, the focusing of parallel X-rays and TXM in the hard X-ray regime. The continuation of SXM tests is inevitable in the soft X-ray regime, as the existing instrument combines high precision and sufficient flexibility to perform meaningful experiments. For the future, the combination of finer outermost zone widths and larger diameter substrates, perhaps containing a defined inclination angle, is very promising. In the hard X-ray regime, the focusing of parallel X-rays with the existing setup is a purely qualitative test. The refinement of this test would require an update of the camera, or at least the imaging objective, to have a better resolution and larger minimal distances between zone plate and objective. In addition the use of an OSA could improve the contrast by blocking unwanted radiation. The performance of the zone plates in the full-field experiments was quite limited, due to their inherent properties (only 4 μm of active zones), but also due to the properties of the beam line (very high coherence of the beam). To improve the results of future experiments, the setup has to be updated, either with the possibility to wobble the condenser, or at least with a diffuser, to break the coherence of the beam. This could simplify the interpretation of the pictures

and perhaps also improve the measurable resolution. In addition this setup would profit a lot from a camera with a larger field of view, to capture a larger fraction of, or the complete image created by the zone plate. In analogy to the soft X-ray regime, the use of an SXM, preferably interferometer controlled, would also be very promising in the hard X-ray regime. The combination of high beam coherence, long focal length and thus working distance and the possibility to directly evaluate the resolution of the zone plate from the images, makes this technique very attractive. For SMX applications, the small active area of the FZP does not cause any problems due to the need of a large center stop.

The pioneering work performed for this thesis set the foundation stone for an establishment of this new technique for FZP manufacturing. The ideas presented to further develop this approach are a possible way to make it a real competition for the routinely used techniques.

Chapter 7

Zusammenfassung in deutscher Sprache

Die vorliegende Dissertation beschreibt ein neues Verfahren zur Herstellung sogenannter Fresnel'scher Zonenplatten (FZP) und die Untersuchung ihrer Abbildungseigenschaften im weichen sowie harten Röntgenbereich. Die Voraussetzungen, die zum Erstellen dieser Arbeit geführt haben, sowie die gewonnenen Ergebnisse und die aus ihnen ableitbaren Konsequenzen für das weitere Vorgehen, sollen im Folgenden zusammengefasst werden.

7.1 Einleitung und Stand der Technik

Der Wunsch, die vorteilhaften Eigenschaften von Röntgenstrahlen für Mikroskopieanwendungen zu nutzen, besteht seit ihrer Entdeckung durch Wilhelm Conrad Röntgen im Jahr 1895 [1, 2]. Ihr Einsatz wurde jedoch zunächst durch den Mangel an geeigneten Linsen verhindert, da Glas aufgrund seines nur wenig von 1 abweichenden Brechungsindexes im Röntgenbereich nicht praktikabel ist. Spiegel [3], gestapelte Konkavlinsen[1] (CRL) [4] und diffraktive Optiken [5] wurden daher als Alternativen erprobt. Das heutzutage in der Röntgenmikroskopie am meisten eingesetzte optische Element, sowohl zur Fokussierung als auch zur Bildgebung, ist die sogenannte Fresnel'sche Zonenplatte [6], durch deren Einsatz sich die Röntgenmikroskopie in den letzten Jahrzehnten [157] zu einer etablierten Methode entwickelt hat. Die FZP stellt ein radiales Beugungsgitter mit nach außen hin schmäler werdenden Streifen, den sogenannten Zonen, dar. Fokusse unterschiedlicher Ordnung werden durch konstruktive Interferenz der an den Zonen gebeugten Lichtwellen

[1] engl.: compound refractive lens

erzeugt. Die Fokallänge (f) der Zonenplatte ist eine Funktion ihres Durchmessers (D), der äußersten Zonenbreite (Δr) und der verwendeten Lichtwellenlänge (λ). Da Zonenplatten sehr chromatisch sind, zeigen sie nur bei der Verwendung von Licht mit schmaler spektraler Bandbreite beugungsbegrenzte Auflösung. Die erreichbare Auflösung der Zonenplatte hängt dabei hauptsächlich von der äußersten Zonenbreite ab.

Zonenplatten werden heutzutage hauptsächlich unter Einbeziehung von Elektronenstrahllithographie[2] (EBL) hergestellt [7]. Dabei wird ein Substrat, meist Silizium oder eine sehr dünne Siliziumnitridmembran, mit einem elektronenempfindlichen Lack belegt, der Lack wird mittels Lithographie strukturiert, entwickelt und die entstandenen Strukturen in ein anders Material überführt. Dies kann entweder durch galvanisches Auffüllen der entstandenen Gräben mit einem Metall oder durch einen Tiefenätzprozess, bei dem die entwickelten Strukturen als Maske dienen, geschehen. Zwar wurden mit speziellen Varianten des Lithographieprozesses Zonenplatten mit Auflösungen von bis zu 9 nm erzeugt [8], jedoch besitzt die Lithographie auch einige Einschränkungen. Durch Streuprozesse der Elektronen im Lack und im Substrat können nicht beliebig feine Linien geschrieben werden, wenn Muster hoher Liniendichte, wie dies bei Zonenplatten der Fall ist, verlangt werden. Des Weiteren ist das Aspektverhältnis, das in Lithographieprozessen erreicht werden kann, beschränkt, was die Herstellung von Zonenplatten mit hoher Effizienz für den harten Röntgenbereich sehr erschwert. Als Alternative wurde die sog. "sputter-sliced"-Methode entwickelt [9], bei der ein um seine Längsachse rotierendes, längliches Substrat durch physikalische Beschichtungsmethoden mit Materialien mit sehr unterschiedlichem Brechungsindex belegt und danach mit mechanischen Verfahren zu einer Linse gedünnt wird. Da die bei dieser Methode eingesetzten Beschichtungsverfahren jedoch meist Zonen mit sich akkumulierender Rauigkeit erzeugen und dies für die Auflösung von Nachteil ist und zudem die eingesetzten mechanischen Dünnungsverfahren auf einige Mikrometer minimaler Dicke beschränkt sind, ist der Einsatz dieser Zonenplatten im weichen Röntgenbereich unmöglich.

Obwohl schon etablierte Methoden zur Zonenplattenherstellung existieren, besitzen diese noch immer Schwachstellen und es ist noch keine Methode vorhanden, die Zonenplatten mit hoher Effizienz und hoher Auflösung in einem breiten Spektralbereich liefert. Die Weiterentwicklung der vorhandenen und die Neuentwicklung von Alternativmethoden zur

[2]engl.: electron beam lithography

Zonenplattenherstellung ist daher, zusätzlich getrieben vom Wunsch nach immer besserer Auflösung, unabdingbar.

7.2 Konzept und verwendete Methoden

Im Rahmen dieser Dissertation wurde ein neues Konzept zur Herstellung von Zonenplatten entwickelt, basierend auf der Grundidee, der Abscheidung von Materialien mit unterschiedlichem Brechungsindex und dem darauffolgenden Schneiden des beschichteten Substrates, ähnlich der "sputter-sliced"-Methode. Jedoch kommen hier erstmals zwei Verfahren zum Einsatz, die so noch nie zur Zonenplattenherstellung verwendet wurden. Die neue Methode zur Herstellung von Multilagenzonenplatten basiert auf der Abscheidung von Al_2O_3- und Ta_2O_5-Schichten auf einer Glasfaser mit dem Atomlagenabscheidungsverfahren[3] (ALD) [10] und dem anschließenden Schneiden und Dünnen der beschichteten Faser mittels fokussiertem Ionenstrahl[4] (FIB) [11] in einem Zweistrahlinstrument (Dualbeam^{TM}). Al_2O_3 dient hierbei als transparentes, Ta_2O_5 als absorbierendes Material. Die Eignung dieser Materialien wurde durch theoretische Berechnung der Beugungseffizienz verifiziert, außerdem eignen sich beide Materialien sehr gut für die Beschichtung mit ALD. Die Verwendung von ALD bietet viele Vorteile gegenüber Kathodenzerstäubung[5], wie die chemische Bindung der Schichten zum Substrat und untereinander, die hohe Qualität der Schichten in Bezug auf Grenzflächen- und sich akkumulierender Rauigkeit, die hohe Konformität der Schichten, ohne das Substrat rotieren zu müssen und die sehr genau einstellbare Schichtdicke. ALD stellt ein chemisches Beschichtungsverfahren dar, bei dem gasförmige Prekursoren gepulst und sukzessive, in Form von Zyklen, in den Reaktionsraum geleitet werden. Im Gegensatz zu physikalischen Beschichtungsverfahren, bei denen die Schichtdicke während der Beschichtung gemessen oder mit Eichkurven über die Beschichtungszeit ermittelt werden muss, erfolgt dies bei ALD unter idealen Bedingungen, atomlagengenau über die Anzahl an Zyklen. Der Dünnungsprozess mittels FIB bietet ebenfalls viele Vorteile gegenüber mechanischen Methoden. Das DualBeam^{TM} ermöglicht die Einstellung der Zonenplattendicke in einem weiten Bereich von einigen hundert Nanometern bis hin zu einigen zehn Mikrometern. Des Weiteren ist die Bearbeitung mittels FIB weitaus materialschonender als mechanische Methoden. Die Oberfläche bleibt frei von Kratzern und sonstigen Verformungen, was sehr saubere Schnitte ermöglicht. Die Kombination der hier

[3] engl.: atomic layer deposition
[4] engl.: focused ion beam
[5] engl.: sputtering

verwendeten Methoden erlaubt die Herstellung von Zonenplatten mit unterschiedlichen Aspektverhältnissen, die sich sowohl für den weichen als auch für den harten Röntgenbereich eignen, was bisher noch von keiner Herstellungsmethode geleistet werden konnte.

7.3 Ergebnisse der Arbeit

Im Rahmen dieser Arbeit wurden Zonenplatten mit einer äußersten Zonenbreite von $\Delta r = 35$, 15 und 10 nm auf einem Glasfasersubstrat hergestellt, wobei bei letzterer zwei verschiedene Beschichtungsschemata (10A und 10B) angewandt wurden. Die Beschichtungen erfolgten in Kooperation mit der BMBF[6]-Forschungsgruppe „Funktionale 3D-Nanostrukturen mittels Atomic Layer Deposition“ am Max-Planck-Institut für Mikrostrukturphysik in Halle (Saale). Alle Zonenplatten wurden dabei als partielle Zonenplatten hergestellt, indem die letzten 4 μm der Zonenstruktur auf eine Faser mit 30 μm Durchmesser abgeschieden und so eine Zonenplatte mit einem Gesamtdurchmesser von 38 μm erzeugt wurde. Die mikroskopische Begutachtung zeigte sowohl im Rasterelektronenmikroskop[7] (REM) als auch im Transmissionselektronenmikroskop[8] (TEM) sehr wohl definierte Zonenstrukturen und eine geringe Grenzflächenrauigkeit für die 35 nm- und die 10B-Zonenplatte. Bei der 35 nm-Zonenplatte konnten jedoch, trotz herausragender Schichtqualität, Abweichungen zwischen den berechneten idealen und den tatsächlich gemessenen Schichtdicken festgestellt werden. Die Schichtdicken der 10B-Zonenplatte zeigten eine starke Streuung um den Mittelwert, verursacht durch die Präparation der TEM-Probe mittels FIB sowie Abweichungen von den theoretischen Schichtdicken. Die Abweichungen der Individual- von den theoretischen Schichtdicken führten daher zu einer Zonenmissplatzierung von 130 bzw. 270 nm für die 35 nm- sowie 270 nm für die 10B-Zonenplatte. Sowohl die 15 nm- als auch die 10A-Zonenplatte zeigte Unregelmäßigkeiten in ihren Schichtstrukturen, die sich auf Probleme während der Beschichtung zurückführen lassen, die während der zur Verfügung stehenden Zeit nicht optimierbar war.

Die Zonenplatten wurden sowohl am Rasterröntgenmikroskop[9] (SXM) MAXYMUS am BESSY II im weichen, als auch am Mikrooptikprüftisch[10] (MOTB) der Strahllinie

[6] Bundesministerium für Bildung und Forschung
[7] engl.: scanning electron microscope
[8] engl.: transmission electron microscope
[9] engl.: scanning X-ray microscope
[10] engl.: microoptics test bench

ID6 an der ESRF im harten Röntgenbereich untersucht. Mit der 35 nm-Zonenplatte konnten im SXM Strukturen mit einer Breite kleiner als 39 nm in einem Nickel- und einem Gold-Siemens-Stern-Testobjekt bei einer Strahlenergie von 1150 bzw. 1496 eV aufgelöst werden. Die gewonnenen Bilder zeigten zudem einen leichten Astigmatismus. Mit der 15 nm-Zonenplatte war es nicht möglich, einen Fokus im SXM zu finden, was sich auf die Fehler in der Zonenstruktur oder auf eine nicht optimal senkrechte Positionierung der FZP im Strahlengang zurückführen lässt. Mit der 10A-Zonenplatte ließen sich nur Strukturen auflösen, die eine Größenordnung über der äußersten Zonenbreite lagen. Die Experimente im harten Röntgenbereich wurden bei 8 keV Strahlenergie durchgeführt und beinhalteten das Fokussieren von nahezu paralleler Strahlung auf eine CCD-Kamera sowie den Einsatz der Zonenplatte als Objektivlinse in einem Vollfeld-Röntgentransmissionsmikroskopieaufbau[11] (TXM). Mit der 35-, der 15- und 10B-Zonenplatte konnte ein symmetrischer Beugungsring beim Fokussieren paralleler Strahlung erzeugt werden, in dem der Rotationswinkel um die Z- sowie der Kippwinkel um die X-Achse optimiert wurden. Auch in diesem Fall übten die Unregelmäßigkeiten in der Zonenstruktur einen negativen Einfluss auf das optische Verhalten der 15 nm- und der 10A-Zonenplatte aus. Im Beugungsring der 15 nm-Zonenplatte zeigten sich Unregelmäßigkeiten in Form von Fransen um den eigentlichen Beugungsring sowie einer leicht ungleichmäßigen Helligkeitsverteilung. Mit der 10A-Zonenplatte war es nicht möglich, einen symmetrischen Beugungsring zu erzielen. Für die 35 nm-Zonenplatte konnte eine Beugungseffizienz von 5,4 % aus einem Intensitätsprofil berechnet werden. Diese Zonenplatte konnte ebenfalls erfolgreich als Objektivlinse im Vollfeldaufbau eingesetzt werden, wo es gelang, Strukturen ≥ 120 nm eines Siemens-Stern-Testobjekts aufzulösen. Die hohe Kohärenz des verwendeten Lichts führte jedoch zu Problemen bei der Interpretation der Bilder, da sich die von den Strukturen herrührende Modulation der Intensität mit zusätzlichen Beugungseffekten, hervorgerufen durch weitere Grenzflächen in der Probe, überlagerte. Ein weiteres Problem stellte die nicht axiale Abbildungsgeometrie dar, die durch den schmalen aktiven Bereich der Zonenplatte (4 μm) und das kleine Bildfeld der Kamera (< 1 mm) nötig wurden.

Trotz der aufgetretenen Probleme bei der 10- und 15 nm-Zonenplatte, kann die Einführung dieser neuen Herstellungsmethode als Erfolg gewertet werden, da sie Zonenplatten aus einer Produktionscharge hervorgebracht hat, die sowohl Strukturen < 39 nm im weichen Röntgenbereich aufzulösen vermochten als auch im harten Röntgenbereich ein-

[11] engl.: transmission X-ray microscope

setzbar waren.

7.4 Zukünftige Perspektiven

Da es sich hier um die erste Arbeit handelt, in der ALD und FIB für die Zonenplattenproduktion zum Einsatz kamen, sollte in erster Linie die Machbarkeit demonstriert werden. Für die Zukunft ist deshalb noch Entwicklungspotenzial in einigen Teilaspekten vorhanden, die im Folgenden aufgezeigt werden sollen.

Als erster Aspekt ist die Wahl der Materialien zu nennen. Theoretische Berechnungen haben ergeben, dass die Kombination Al_2O_3 und SiO_2 die höchsten Werte für die Beugungseffizienz sowohl im weichen als auch im harten Röntgenbereich liefert. Die Abscheidung von SiO_2 mit ALD gestaltet sich jedoch als schwierig und bis jetzt ist kein Prozess, der die Zuverlässigkeit der Abscheidung von Al_2O_3 erreicht, bekannt. Neben der Erforschung neuer ALD-Prozesse ist die Weiterentwicklung der existierenden Prozesse, wie die mikroskopische Untersuchung der 15 nm- und der 10A-Zonenplatte zeigte, in Bezug auf Zuverlässigkeit, Reproduzierbarkeit, Verkürzung der Zyklenzeit und Langzeitstabilität ebenfalls unabdingbar. Dies war im Laufe dieser Arbeit aufgrund des beschränkten Zugangs zur verwendeten ALD-Anlage nur sehr begrenzt möglich. Des Weiteren sollten neue Abscheidungsstrategien entwickelt werden, um das Zonenplattengesetz möglichst genau zu approximieren.

Auch der Einsatz neuer Substrate bietet interessante Möglichkeiten. Während Glasfasern als ideales Substrat in Bezug auf Oberflächenreaktivität und -rauigkeit sowie Rundheit, die in Zukunft mit einer Genauigkeit im Bereich der äußersten Zonenbreite gemessen werden sollte, identifiziert wurden, weisen sie auch Nachteile auf. Wegen ihrer Sprödheit sind mechanische Schneideverfahren wie die Mikrotomie bei ihnen nicht anwendbar. Fasern aus hochtemperaturbeständigen Polymeren bieten dafür eine interessante Alternative. Des Weiteren sollten Fasern größeren Durchmessers verwendet werden, um die Fokallänge und damit die Handhabbarkeit zu verbessern. Auch andere Substratgeometrien wie konische Fasern oder Kugeln bieten, in Verbindung mit lokalisierter FIB-Präparation, interessante Möglichkeiten. Hohle Substrate wie Kapillaren, die auf der Innenseite beschichtet werden, sind ebenfalls denkbar. Da erste Versuche während dieser Arbeit jedoch ohne Erfolg blieben, sind dafür tiefgreifende Untersuchungen aller zugrunde

liegenden Prozesse notwendig.

Der Wunsch nach immer feinerer Auflösung treibt die Entwicklung von Zonenplatten mit immer kleineren äußersten Zonenbreiten ($\leq 10\,\mathrm{nm}$) voran. Da ALD für die Abscheidung sehr dünner Filme prädestiniert ist, ergeben sich daraus sehr interessante Möglichkeiten für den hier vorgestellten Ansatz.

Auch die Testeinrichtungen für Zonenplatten lassen sich weiter verbessern. Während SXM im weichen Röntgenbereich eine sehr weit entwickelte Methode darstellt und die Verbindung von kleineren äußersten Zonenbreiten mit Substraten größeren Durchmessers, die evtl. einen definierten Winkel zur optischen Achse aufweisen, sehr erfolgversprechend ist, besteht vor allem im harten Röntgenbereich Potenzial zu Verbesserungen. Die Fokussierung von paralleler Strahlung auf eine Kamera ist, mit dem existierenden Aufbau, ein rein qualitatives Verfahren. Mehr Aussagekraft würde sich durch den Einsatz einer neuen Kamera und/oder eines neuen Objektivs ergeben, das zum einen mehr Auflösung und zum anderen eine kürzere Minimaldistanz zwischen FZP und Kamera ermöglicht. Auch der Einsatz einer OSA könnte zu Verbesserungen in Bezug auf Streustrahlung führen. Die Probleme, die während des Tests der Zonenplatte im Vollfeldaufbau zutage traten, lassen sich zum einen auf die Zonenplatte und zum anderen auf die Strahlcharakteristik zurückführen. Um die durch die schmale aktive Fläche der Zonenplatte nötig gewordene nicht axiale Abbildungsgeometrie zumindest teilweise auszugleichen, wäre auch hier eine Kamera mit größerem Bildfeld sehr von Vorteil. Das Problem der hohen Strahlkohärenz ließe sich entweder durch die Möglichkeit den Kondensor zu schütteln[12] oder durch einen Diffuser verbessern. Dadurch ließe sich die Kohärenz der Strahlung brechen, was die Interpretation der erhaltenen Bilder vereinfachen und vielleicht die gemessene Auflösung verbessern würde. Als vielversprechende Alternative bietet sich auch im harten Röntgenbereich der Einsatz eines Rastermikroskops (SXM) an, vor allem wenn dieses über Interferometerkontrolle verfügt. Die Attraktivität dieser Technik liegt vor allem in der größeren Fokallänge im harten Röntgenbereich sowie der hohen Strahlkohärenz, die sich hier positiv auswirkt. Außerdem ließe sich die Auflösung direkt aus den Bildern bestimmen und auch die schmale aktive Fläche der Zonenplatte stellt aufgrund der Notwendigkeit eines großen Mittenstopps kein Problem dar.

[12] engl.: wobbling

Wenn nur einige der hier vorgestellten Ideen erfolgreich verwirklicht werden könnten, ließe sich die neue Technik zur Zonenplattenherstellung sicherlich als attraktive Alternative zu den bestehenden Techniken etablieren. Sie besitzt das Potenzial der Realisierung von Zonenplatten mit bis deutlich unter 10 nm äußerer Zonenbreite und der Herstellung großer Stückzahlen durch den vorgestellten Zweistufenprozess. Da die erhaltenen Linsen sehr robust im Vergleich zu EBL-Zonenplatten sind, ist aufgrund der großen von ihnen bewältigbaren Wärmelast auch eine Anwendung im Freie-Elektronen-Laser (FEL) denkbar.

Appendix A

Details of the EBL fabrication process

Description of the single layer process for FZP fabrication with EBL (presented in figure A.1, adopted from [6]): The substrate in this process is a back etched silicon frame, covered

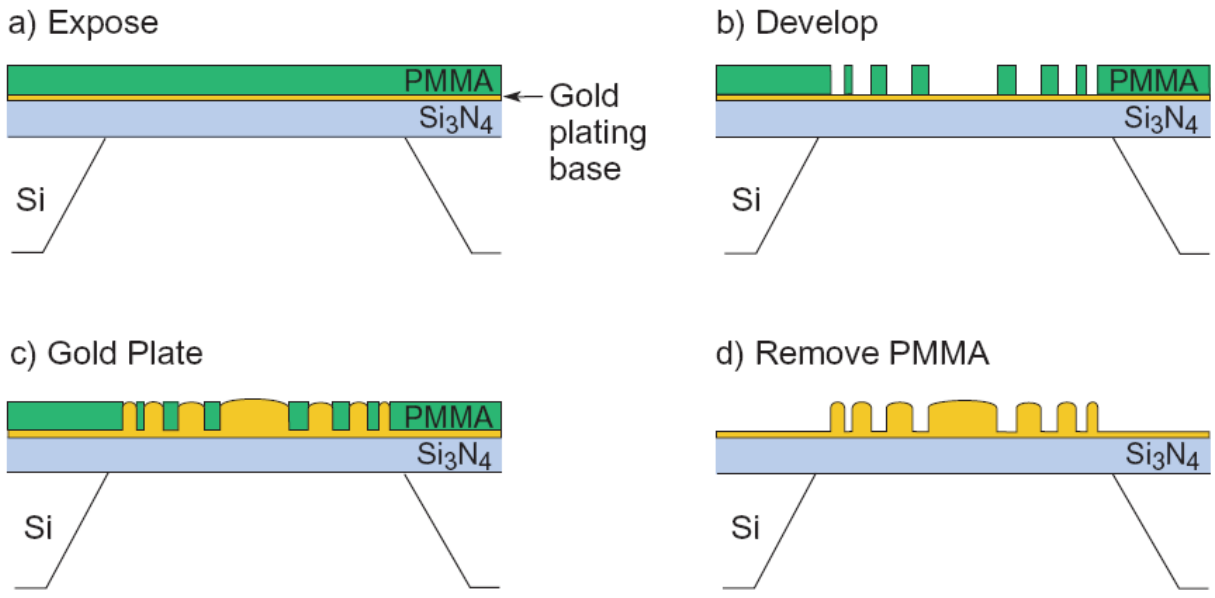

Figure A.1: Schematic illustration of the single layer process for zone plate fabrication. The fabrication steps are: a) Expose, b) Develop, c) Gold plate and d) Remove PMMA.

with a 100 nm thin Si_3N_4 membrane, used as a carrier. As a basis for the lithography, a gold plating base and a chromium adhesion layer (not shown in the image), both approx. 5 nm thick, are evaporated onto the membrane, followed by a spin coating step with

PMMA (polymethyl methacrylate). The thickness of the PMMA (around 100 nm) is adjusted, according to the target thickness of the zone plate. In the first step the zone plate pattern is written into the PMMA with electron beam lithography at a beam energy up to 100 keV a). This is followed by development b), during which the exposed areas of the resist are dissolved. Now as the plating base is exposed, the zone material (mainly gold or nickel) is electroplated into the PMMA mould c). In a final step, the remaining PMMA is dissolved in acetone, leaving a free standing zone plate on the membrane d).

Description of the double layer process for FZP fabrication with EBL illustrated in figure A.2 (adopted from [87]): In this approach, a polymer layer (AZPN114) is deposited

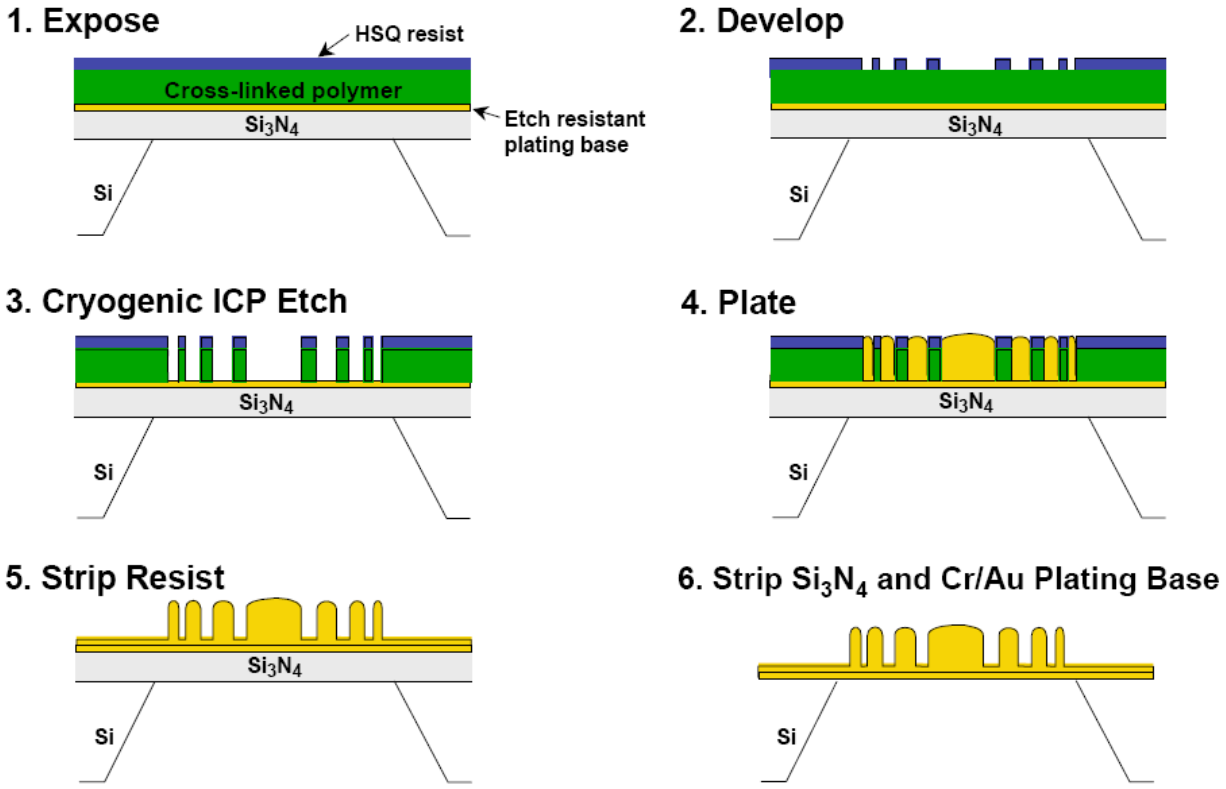

Figure A.2: Schematic illustration of the doublelayer process for zone plate fabrication. The fabrication steps are: 1. Expose, 2. Develop, 3. Cryogenic ICP Etch, 4. Plate, 5. Strip resist and 6. Strip Si_3N_4 and Cr/Au plating base. Details are given in the text.

on top of the plating base and the adhesion layers (5 nm titanium and 10-12 nm germanium). The polymer is hard baked to form a solid base for the high resolution negative tone resist HSQ (hydrogen silsesquioxane) which is deposited after the baking step on top the AZPN114 with a thickness of 30 nm. In step 1. the coated membrane is exposed

with the zone plate pattern, followed by development 2. in which the non exposed areas are dissolved. In step 3. the pattern is transferred into the hard baked polymer layer by cryogenic (-100°C) ICP etching. Then the mould is plated with the zone material 4. In step 5. and 6. the remaining resist and the Si_3N_4 membrane are stripped.

Appendix B

Details of the ALD deposition of the zone plates

As the deposition of the $\Delta r = 35\,nm$ zone plate was performed during a different time period than the deposition of the $\Delta r = 10$ and $15\,nm$ zone plate, different growth rates where estimated for their deposition.
For the $\Delta r = 35\,nm$ FZP, the growth rates equal:

Al_2O_3: $t = 0.13*x - 7.17$

Ta_2O_5: $t = 0.06*x - 0.71$

For the $\Delta r = 10$ and $15\,nm$ FZP, the growth rates equal:

Al_2O_3: $t = 0.14*x - 3.07$

Ta_2O_5: $t = 0.08*x - 1.03$

where x is the number of ALD-cycles and t is the resulting thickness in nm.

For the zone plate with $\Delta r = 35\,nm$ 103 zones with a thickness ranging from 44 to 35 nm were deposited. This corresponds to a number of ALD cycles varying from 393 to 327 for Al_2O_3 and 700 to 554 for Ta_2O_5. After each loop, a defined decrement, different for both materials, is subtracted from the number of cycles of the previous loop, to gain a closer resemblance to the theoretical zone thickness. The maximum deviation of the theoretical thickness for each zone, calculated via equation 2.9 and the zone thickness calculated via the growth rate was 0.94 nm. In total, 51455 ALD cycles in a total deposition time of 148 hours were deposited. The individual cycle numbers are summarized in table B.1. For the deposition of the zone plate with $\Delta r = 15\,nm$, 240 zones with a thickness ranging

Table B.1: Compilation of the cycles for the deposition of the $\Delta r = 35\,nm$ zone plate.

Loops	**Material**	**Cycles (beginning)**	**decrement**
9	Al_2O_3	393	-1
	Ta_2O_5	700	-3
15	Al_2O_3	383	-2
	Ta_2O_5	673	-3
23	Al_2O_3	354	-1
	Ta_2O_5	628	-3
5	Al_2O_3	331	-1
	Ta_2O_5	560	-2
1	Ta_2O_5	448	-

from 19 to 15 nm were deposited. This corresponds to a number of ALD cycles varying from 162 to 135 for Al_2O_3 and 248 to 203 for Ta_2O_5 and remained constant for the given number of loops. In total, 450101 ALD cycles in a total deposition time of 130 hours were deposited. The individual cycle numbers are summarized in table B.2. For the deposition

Table B.2: Compilation of the cycles for the deposition of the $\Delta r = 15\,nm$ zone plate.

Loops	**Material**	**Cycles**
8	Al_2O_3	162
	Ta_2O_5	248
9	Al_2O_3	159
	Ta_2O_5	243
10	Al_2O_3	156
	Ta_2O_5	238
11	Al_2O_3	153
	Ta_2O_5	233
11	Al_2O_3	150
	Ta_2O_5	228
13	Al_2O_3	147
	Ta_2O_5	223
12	Al_2O_3	144
	Ta_2O_5	218
15	Al_2O_3	141
	Ta_2O_5	213
15	Al_2O_3	138
	Ta_2O_5	208
16	Al_2O_3	135
	Ta_2O_5	203
1	Ta_2O_5	797

of the zone plates with $\Delta r = 10\,nm$ two different depositions, termed 10A and 10B were performed. For 10B, 15 cycles less than for 10A were deposited for every Ta_2O_5 zone to better meet the target zone thickness. This adjustment of the calibration was made due to the experienced overdeposition of Ta_2O_5 on Al_2O_3 measured in the TEM investigations of the $\Delta r = 35\,nm$ zone plate. By taking overdeposition into account, the actual Ta_2O_5 layer thicknesses should be equal for 10A and 10B. In both depositions, a total number of 360 zones with a thickness ranging from 12.7 to 10 nm was deposited. The number of ALD cycles for Al_2O_3 ranged from 116 to 97 for both depositions. For 10A the number of ALD cycles for Ta_2O_5 ranged from 171 to 138, for 10B from 156 to 123. The number of cycles remained constant for both materials for the given number of loops. In total, for 10A, 47318 ALD cycles in a total deposition time of 136 hours, and for 10B, 44633 ALD cycles in 128 hours were deposited. Onto all zone plates, a capping layer of 1000 cycles Ta_2O_5 was deposited to protect the outermost zones. The individual cycle numbers are summarized in table B.3. To illustrate the different approaches for approximating the theoretical zone thicknesses with a feasible programming scheme for the ALD, the theoretical thicknesses and the targeted thicknesses, obtained via the number of ALD cycles and the growth rate, are plotted in the following against the number of the layer for the zone plate with $\Delta r = 35\,nm$ (figure B.1), $\Delta r = 15\,nm$ (figure B.2) and $\Delta r = 10\,nm$ (figure B.3).

Table B.3: Compilation of the cycles for the deposition of the $\Delta r = 10\,nm$ zone plate 10A. The zone plate 10B has been deposited with the same cycle numbers for Al_2O_3 and 15 cycles less for every layer of Ta_2O_5.

Loops	**Material**	**Cycles**
6	Al_2O_3	116
	Ta_2O_5	171
7	Al_2O_3	115
	Ta_2O_5	169
7	Al_2O_3	114
	Ta_2O_5	167
6	Al_2O_3	113
	Ta_2O_5	166
8	Al_2O_3	112
	Ta_2O_5	164
7	Al_2O_3	111
	Ta_2O_5	162
8	Al_2O_3	110
	Ta_2O_5	160
9	Al_2O_3	109
	Ta_2O_5	159
8	Al_2O_3	108
	Ta2O5	157
9	Al_2O_3	107
	Ta_2O_5	156
9	Al_2O_3	106
	Ta_2O_5	153
9	Al_2O_3	105
	Ta_2O_5	152
10	Al_2O_3	104
	Ta_2O_5	151
10	Al_2O_3	103
	Ta_2O_5	149
10	Al_2O_3	102
	Ta_2O_5	147
11	Al_2O_3	101
	Ta_2O_5	145
11	Al_2O_3	100
	Ta_2O_5	144
12	Al_2O_3	99
	Ta_2O_5	142
12	Al_2O_3	98
	Ta_2O_5	140
11	Al_2O_3	97
	Ta_2O_5	138
1	Ta_2O_5	862

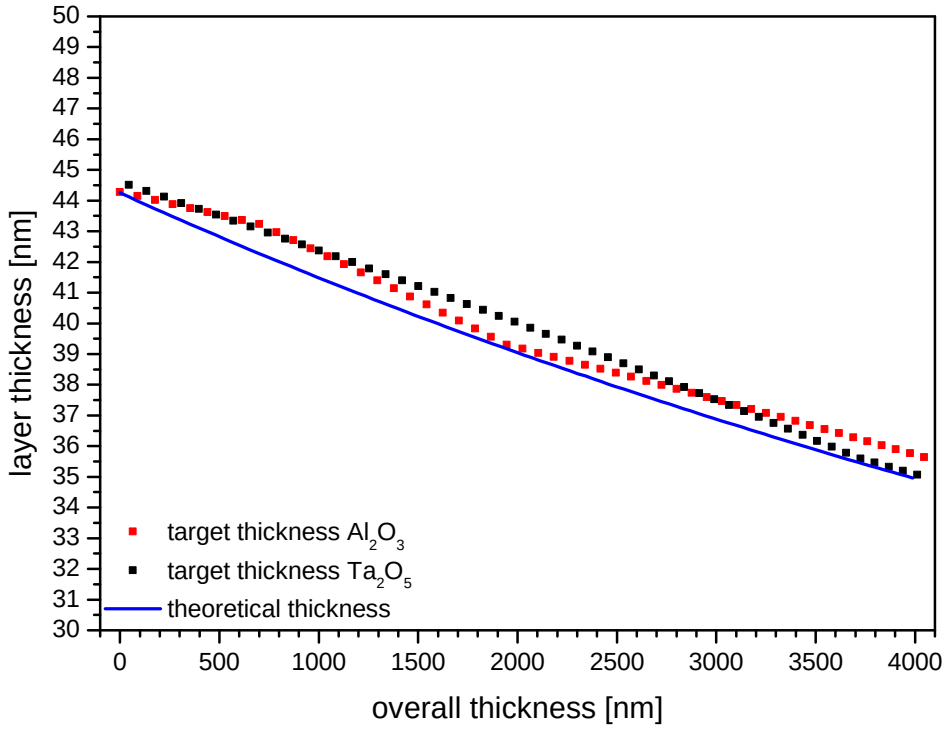

Figure B.1: Comparison of the theoretical and the targeted layer thicknesses for the $\Delta r = 35\,\mathrm{nm}$ zone plate.

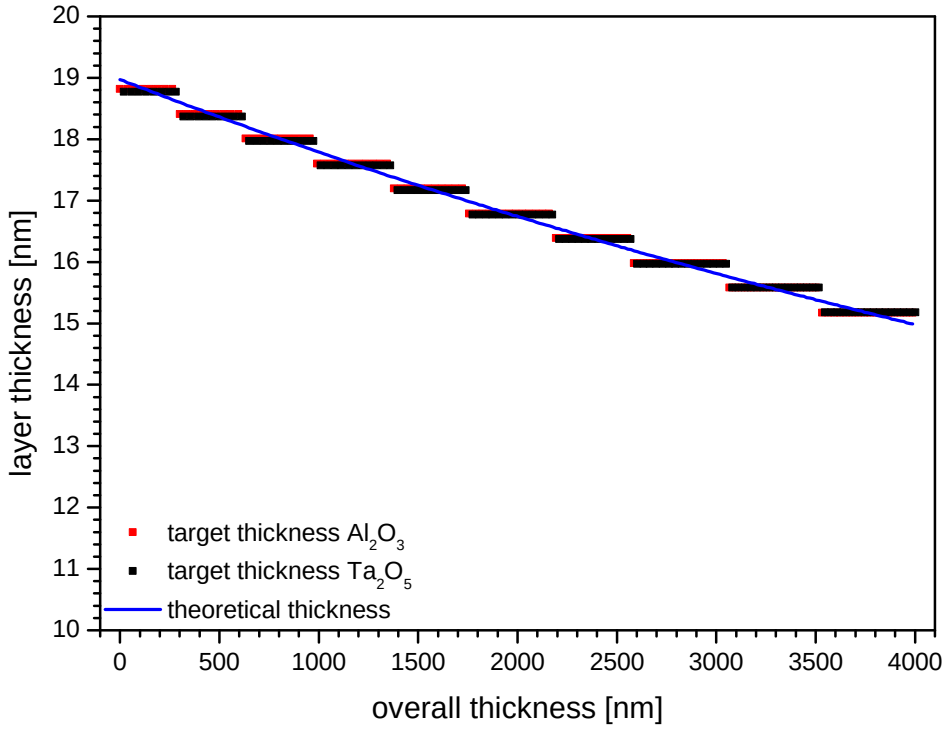

Figure B.2: Comparison of the theoretical and the targeted layer thicknesses for the $\Delta r = 15\,\mathrm{nm}$ zone plate.

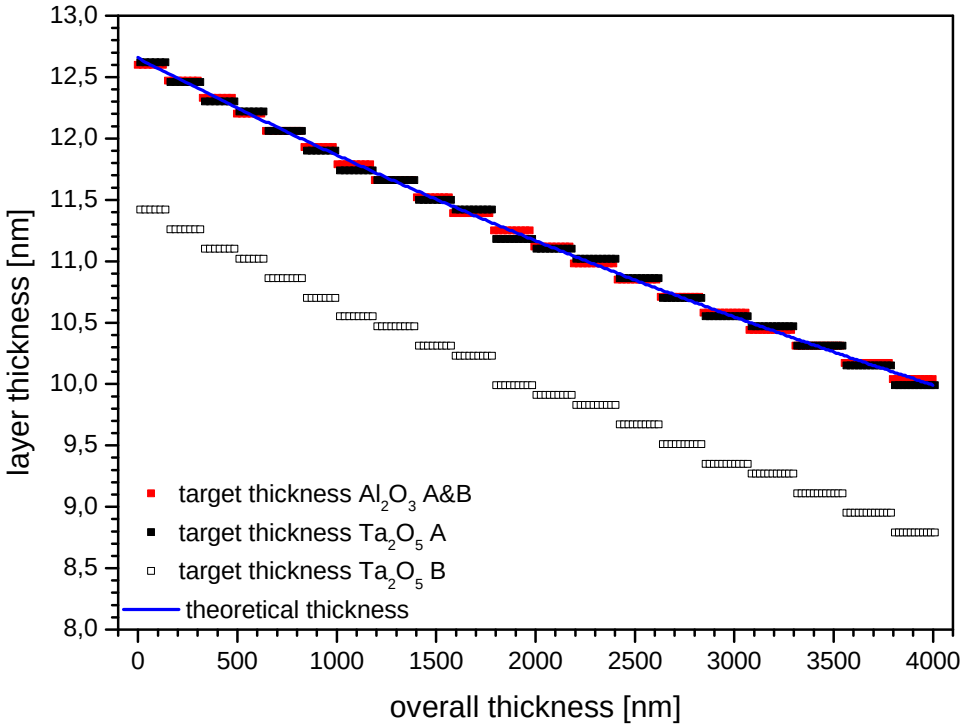

Figure B.3: Comparison of the theoretical and the targeted layer thicknesses for the $\Delta r = 10\,nm$ zone plate. The thicknesses marked with the open symbols are calculated the growth rate with 15 cycles less for each layer. The expected overdeposition has not been respected. In reality, the actual thicknesses for Ta_2O_5 should be equal for 10A and 10B.

Appendix C

Details of the FIB sectioning process of the zone plates

In the following, a compilation of the milling parameters for the sectioning and thinning procedure of the zone plates in the FEI Nova NanoLab 600 DualBeam^{TM} system is given in table C.1. At some preparation steps, no exact values for ion beam currents or pattern sizes can be given, because they are dependent on the special circumstances for this exact preparation and the experience of the user, then the parameter is defined as "variable". The angle which is referred to is the tilt angle of the stage. At 0° the stage is perpendicular to the electron beam, at 52° the stage is perpendicular to the ion beam.

Table C.1: Compilation of the parameters set for the preparation of the FZP in the Dual-Beam.

Step of Preparation	**Kind of patterning**	**Beam current**	**Pattern area (l*w*h [μm])**	**Angle [°]**	**Comment**
Deposition of protection layer	Pt-deposition	0.5 nA	5*20*1-2 (rectangle)	52	First, that half of the fibre which faces the needle, then turn the fibre by 180° and deposit on the other side.
Pre-cutting the slice	Ion-milling	7-20nA	40-60*39*8-10 (cross section) 15-25*39*8-10 (rectangle)	52	Cross-section ranges from surface of fibre to bottom. Rectangle creates bridge between slice and cross section. Size of the pattern depends on beam current, depth depends on material and total layer thickness.
Attachment of the needle	Pt-deposition	variable	variable (rectangle)	0	Needle is attached on top of the slice at the joint of the two protective coating depositions.
Free-cutting of the slice	Ion-milling	7-20nA	variable (rectangle)	0	The pattern is placed on the bridge, as close as possible to the cross-section.
Transfer	-	-	-	0	The slice is lifted from the fibre to the TEM-grid
Attachment of the slice	Pt-deposition	variable	variable (rectangle)	0	Size of the pattern and beam current depend on the situation. Two patterns on both sides with >2μm thickness are usually required.
Disconnection of the needle	Ion-milling	variable	variable (rectangle)	0	The needle is cut through, as close to the attachment point as possible.
Filling of the gaps	Pt-deposition	0.03-1nA	variable (rectangle)	0	The gaps between slice and grid are filled with Pt Pattern and current get successively larger. First, one side is filled, then grid is turned 180°.
Thinning of the slice	Ion-milling	5-1nA	variable (cleaning cross section)	51-53	The slice is successively thinned from both sides to form the FZP. To achieve a perpendicular cut, the slice has to be over- or under-tilted if the slice shall be thinned from the back or front side. The current is decreased from 5 over 3 to 1 nA and the size of the pattern is decreased accordingly.
optional: beam stop deposition	Pt-deposition	3nA	15*2-3 (circle)	52	On the FZPs for the soft X-ray range, a beam stop is deposited directly onto the glass core of the FZP. All glass should be covered, but no zones obstructed.

Appendix D

Details of the applied substances, substrates and other components

D.1 Chemical components

Al_2O_3-precursor

product: Trimethylaluminium (TMA), $(CH_3)_3Al$; purity >98 %; product number: 93-1360; CAS registry number: 75-24-1; supplier: Strem Chemicals, Inc.

Ta_2O_5-precursor

product: Tantalum(V)ethoxide, $Ta(OEt)_5$; purity: 99.99+ % Ta (PURATREM); product number: 93-7303; CAS registry number: 6074-84-6; supplier: Strem Chemicals, Inc.

H_2O_2-precursor

product: Hydrogen peroxide H_2O_2; purity: 30 % (in aqueous solution); product number: 822287; supplier: Merck KGaA

glue for the fibres

product: EPO-TEC H20E-PFC; description: two component epoxy glue, containing silver for electrical conductivity, extra low out gassing (NASA-test verified); supplier: PolytecPT

D.2 Substrates and support materials

glass fibre

product: A2 fiber; diameter: 30 μm; material: glass (SiO_2); supplier: SCHOTT AG

TEM-grids

Cu-grids: material: Cu; product number: GRD-0001.01.01; diameter: 3 mm; thickness: 20 - 25 μm; posts: 3; supplier: Omniprobe. Illustration for Cu-grid see figure D.1.

Mo-grids: material: Mo; product number: GRD-0001.03.01; diameter: 3 mm; thickness: 20 - 25 μm; posts: 3; supplier: Omniprobe. Illustration for Mo-grid see figure D.2.

support mesh

product: wire cloth; material: stainless steel V4A (1.4571); mesh width: 0.4 - 0.5 mm

D.3 Mechanical components

D.3.1 Components for MAXYMUS (BESSY)

modified FZP-holder

custom made; material: Si-Al-bronze (AMS 4631, 4634); product number for material: C64200; supplier for material: National Bronze & Metals, Inc.; dimensions: 1.4 x 1 x 1.4 cm (l x w x h); hole: 200 μm. Illustration see figure D.3.

OSA

custom made; material: stainless steel V2A (1.4301); dimensions: 26.2 x 5.6 x 0.1 (l x w x t); holes: 20 / 25 / 30 μm; supplier: Günther Frey GmbH & Co. KG. Illustration see figure D.4.

D.3.2 Components for ID6 (ESRF)

zone plate holder

custom made; material: Al; dimensions: 1.5 x 2.4 x 2 cm (l x w x h); holes: 3 x 200 μm. Illustration see figure D.5.

aperture holder for full-field

custom made; material: Al; dimensions: 6 x 1 x 0.2 cm (l x w x t). Illustration see figure D.6.

aperture for full-field

custom made; material: Pt/Ir 95/5 %; dimensions: 45 x 4 x 0.1 mm (l x w x t); holes: 3 x 38 $\pm$2 μm; supplier: Günther Frey GmbH & Co. KG. Illustration see figure D.7.

test object holder

custom made; material: Al; dimensions: 4 x 4 x 2 cm (l x w x h); window/hole: 3.5 x 3.5 mm / 200 μm. Illustration see figure D.8.

nanopositioners

product: ANR200/RES; function: rotation 360° (endless) in both directions; encoder: resistive; supplier: attocube systems AG.; Illustration see figure D.9.
product: ANGt101/RES; function: tilt 6.6° (total); encoder: resistive; supplier: attocube systems AG.; Illustration see figure D.10.

D.4 X-ray optical components

hard X-ray Siemens-star test pattern

product number: X50-30-7; supplier: Xradia Inc.; material: gold; smallest feature size: 50 nm; structure height: 700 nm $\pm$ 10%; Siemens-star diameter: 30 μm; substrate: Si_3N_4-membrane (500 x 500 x 0.3 μm) on Si-frame (2 x 2 mm); membrane is mounted on 5 x 5 mm Si-chip. Illustration of mounting see figure D.11.

soft X-ray Siemens-star test pattern

product number: X30-30-2; supplier: Xradia Inc.; material: gold; smallest feature size: 30 nm; structure height: 180 nm ± 10%; Siemens-star diameter: 30 μm; substrate: Si_3N_4-membrane (200 x 200 x 0.1 μm) on Si-frame (2 x 2 mm); membrane is mounted on 5 x 5 mm Si-chip. Mounting similar as in figure D.11.

hard X-ray beam stop

custom made from supplier: NTT-AT Corporation; material: gold; pattern thickness: 30 - 40 μm; pattern diameter: 30 μm; substrate: SiC/SiN-membrane (1500 x 1500 x 2/0.3 μm) on Si-frame (10 x 10 mm). Illustration of pattern layout see figure D.12.

D.5 Collection of drawings and images

Figure D.1: Cu-TEM grid by Omniprobe.

Figure D.2: Mo-TEM grid by Omniprobe.

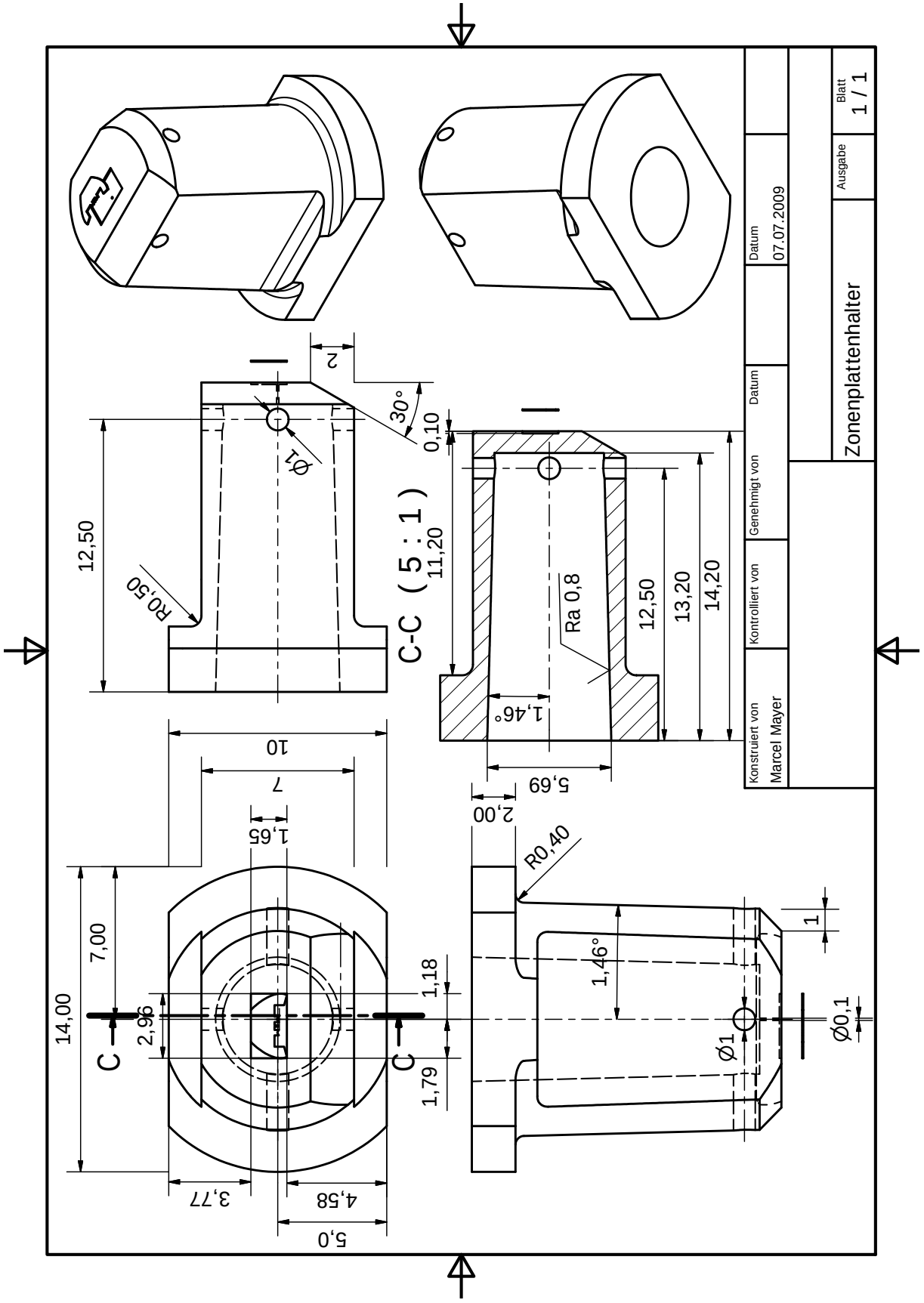

Figure D.3: Modified FZP holder for MAXYMUS.

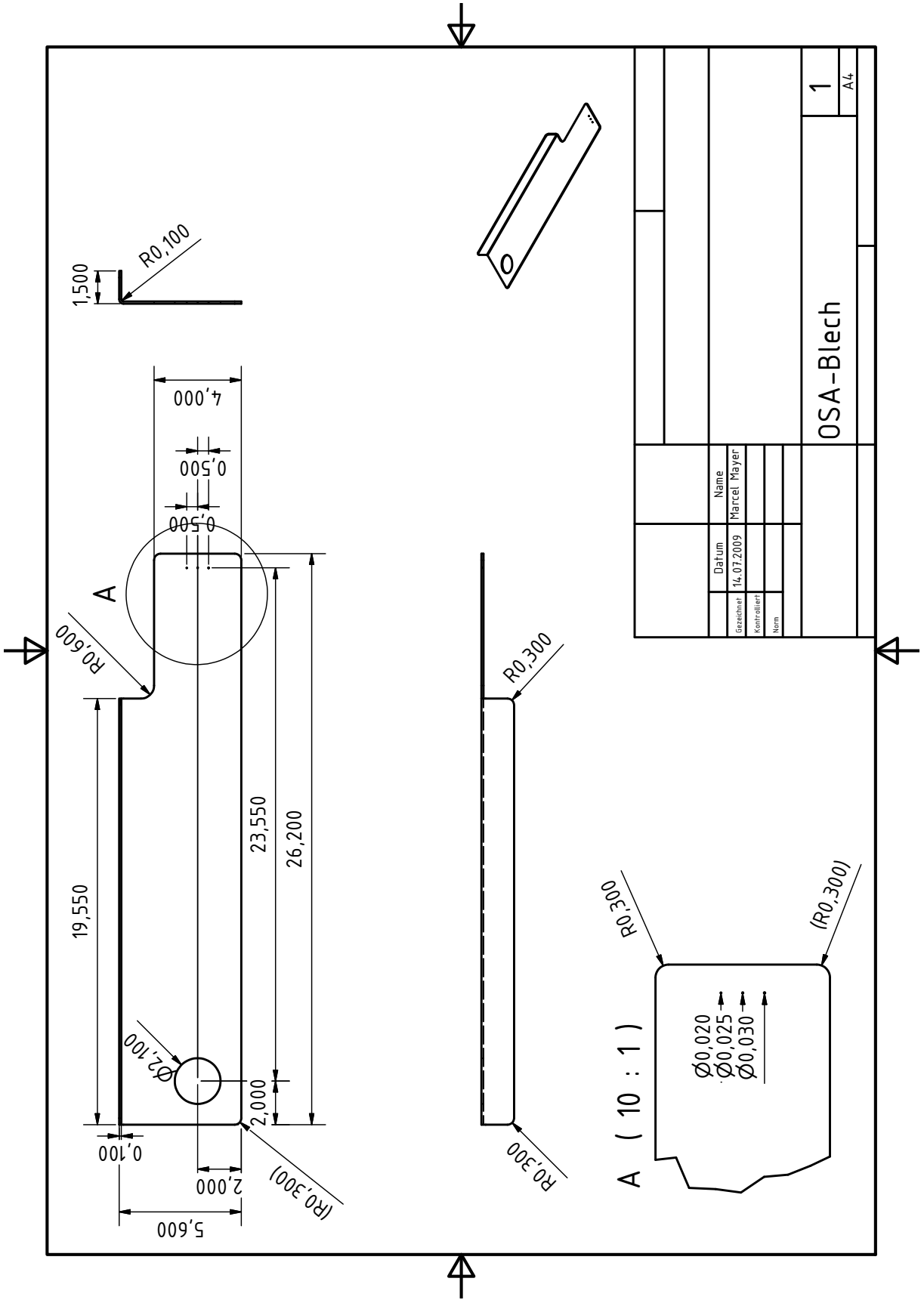

Figure D.4: OSA for MAXYMUS.

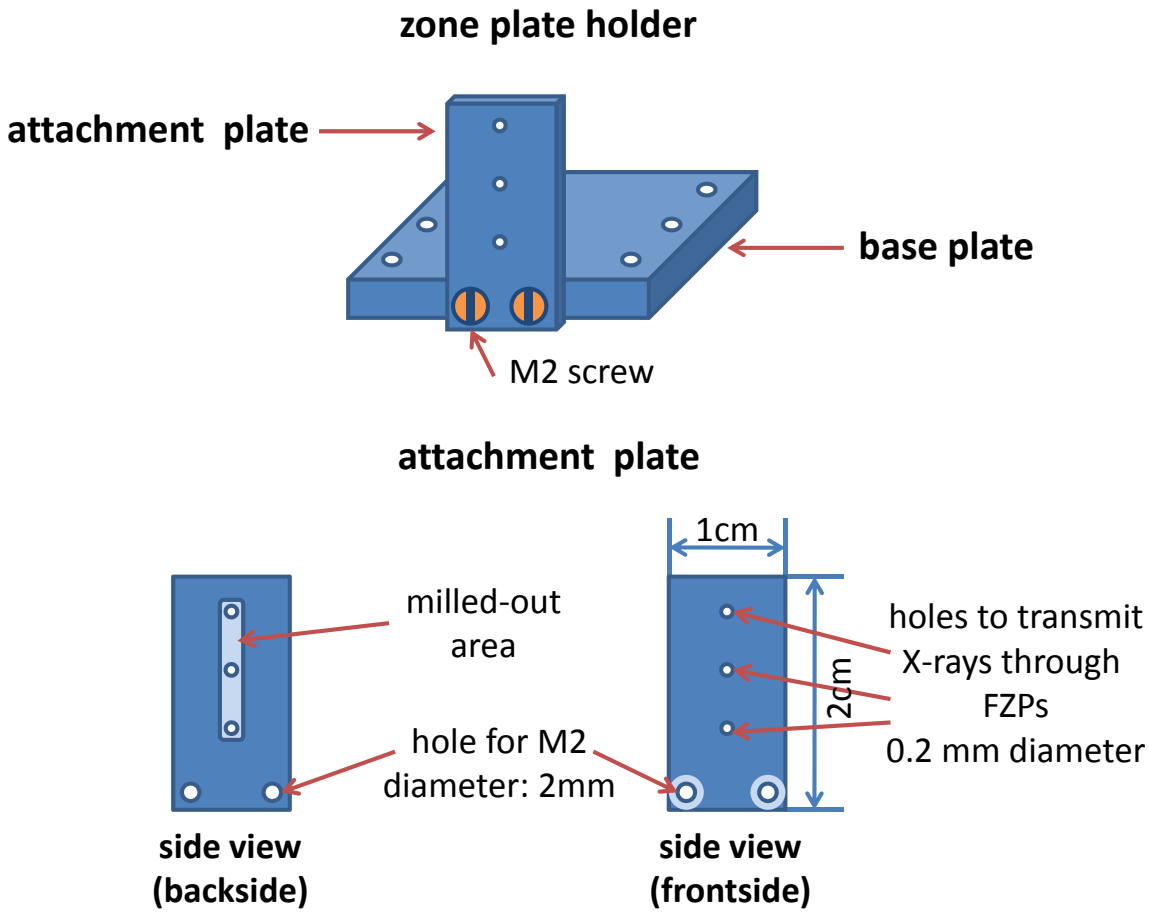

base plate

The base plate is designed to fit ANGt101/RES in size and hole arrangement.

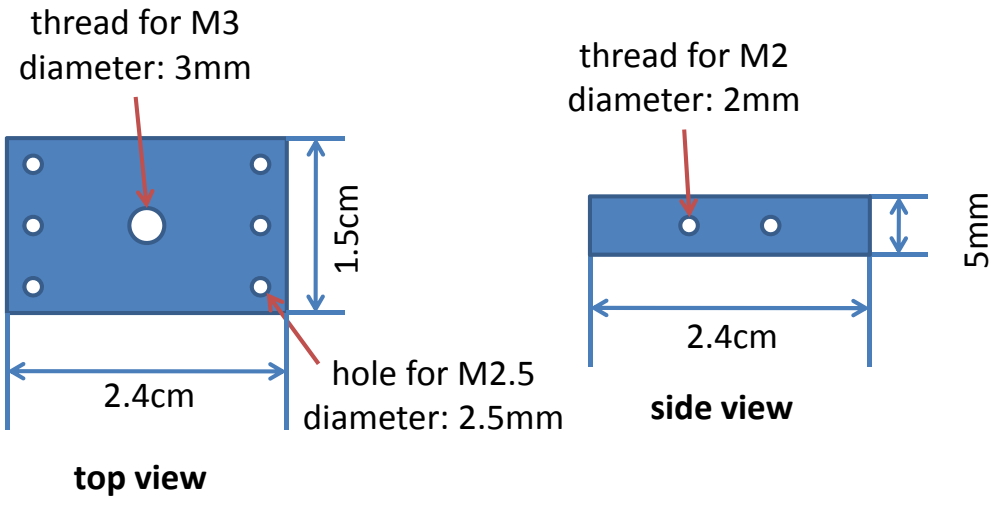

Figure D.5: Zone plate holder.

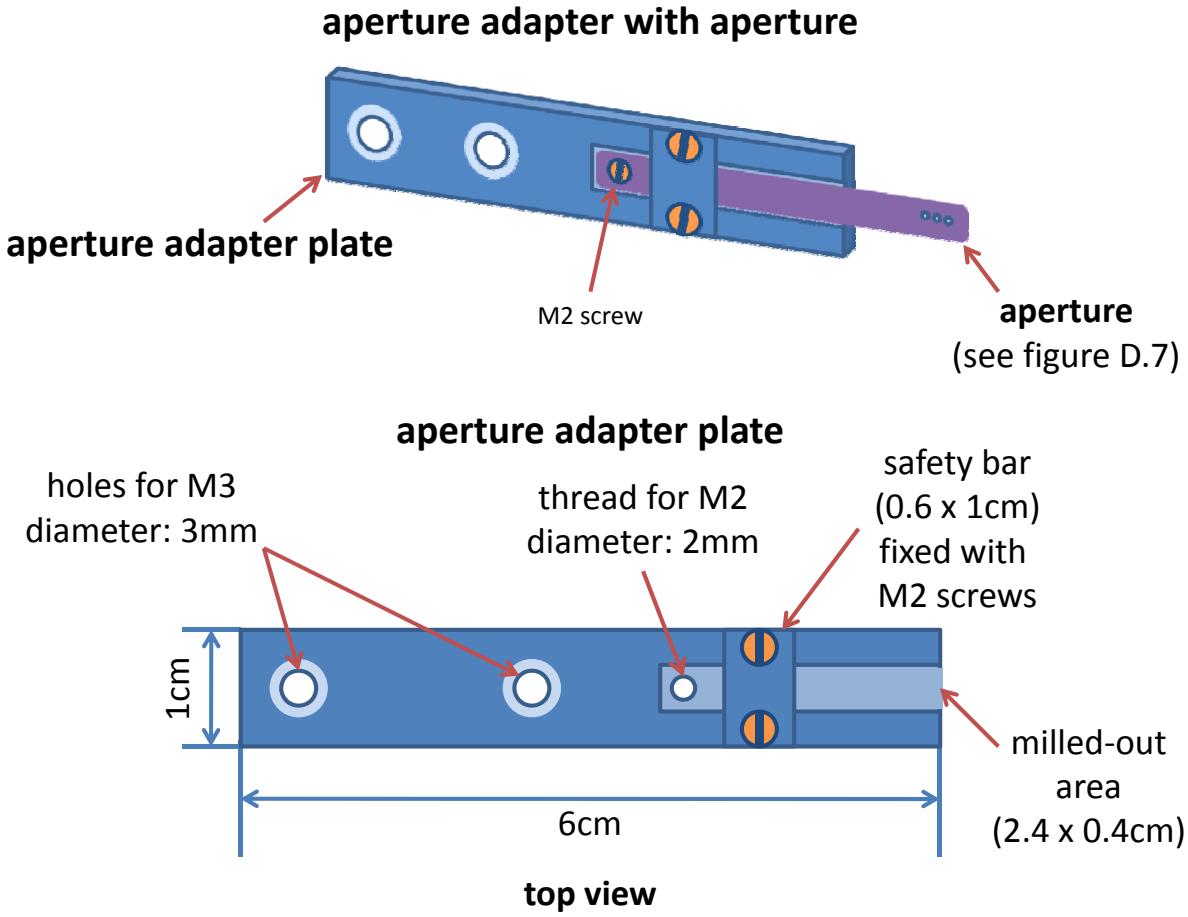

Figure D.6: Aperture holder.

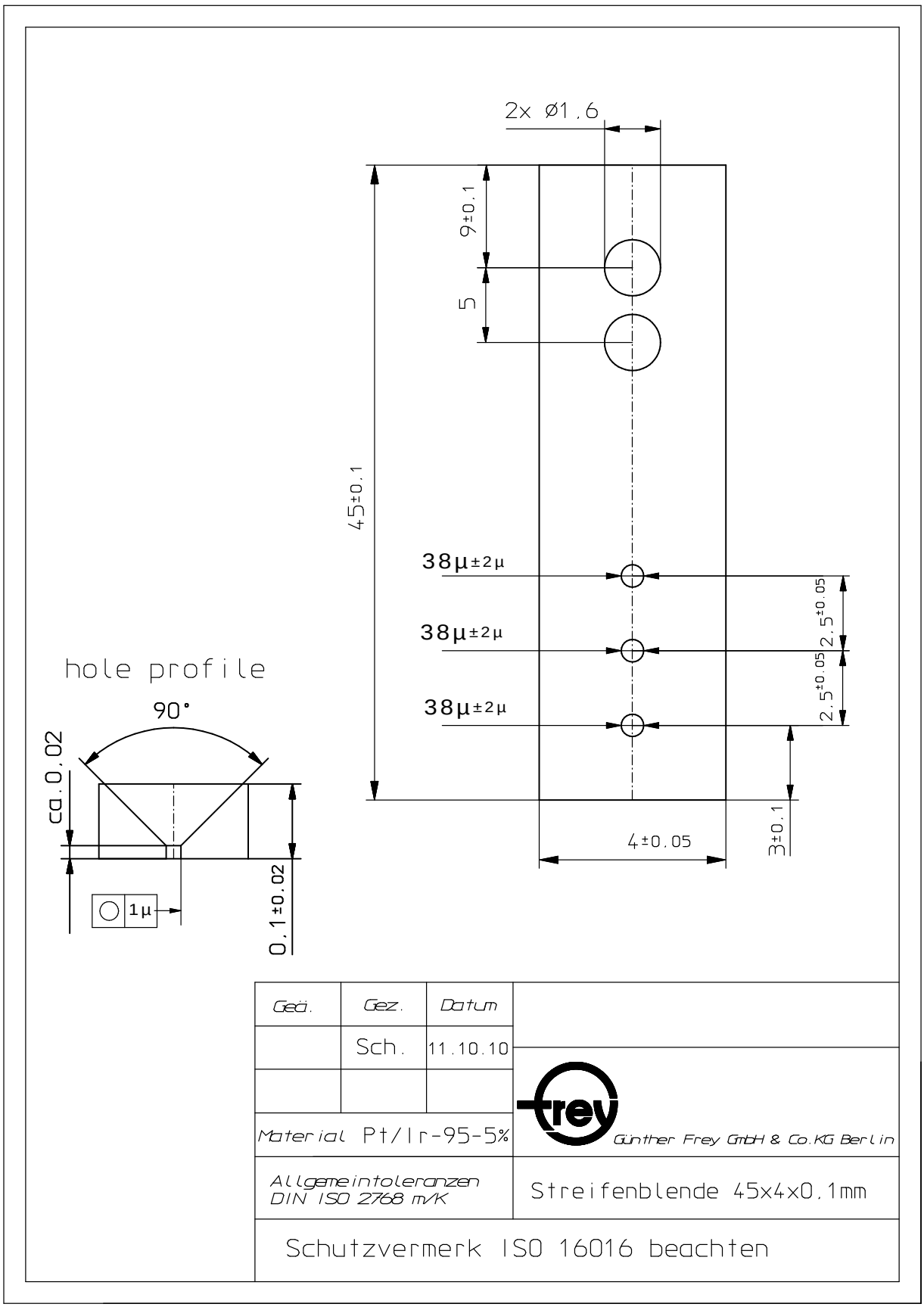

Figure D.7: Aperture for full-field experiments.

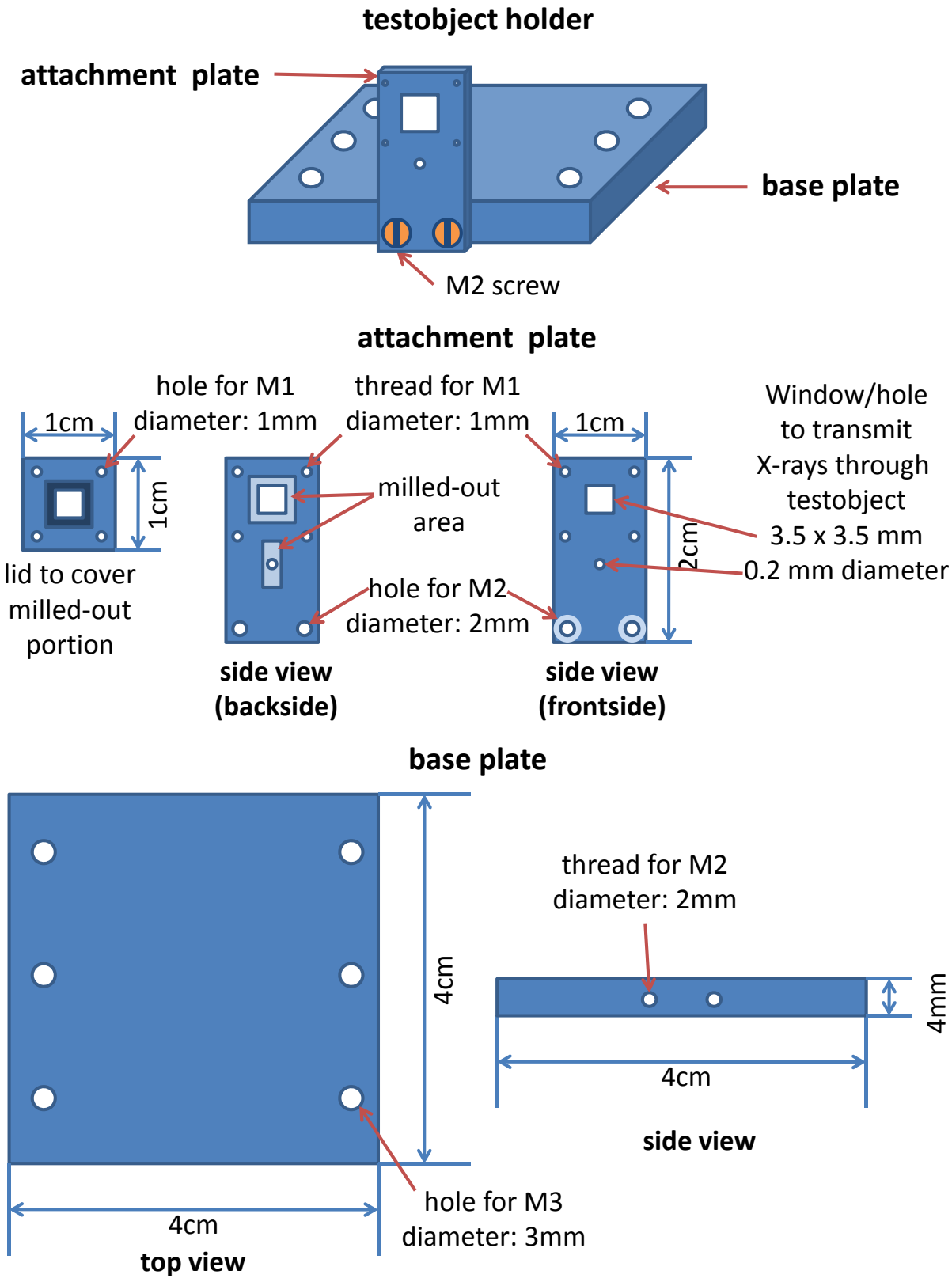

Figure D.8: Testobject holder.

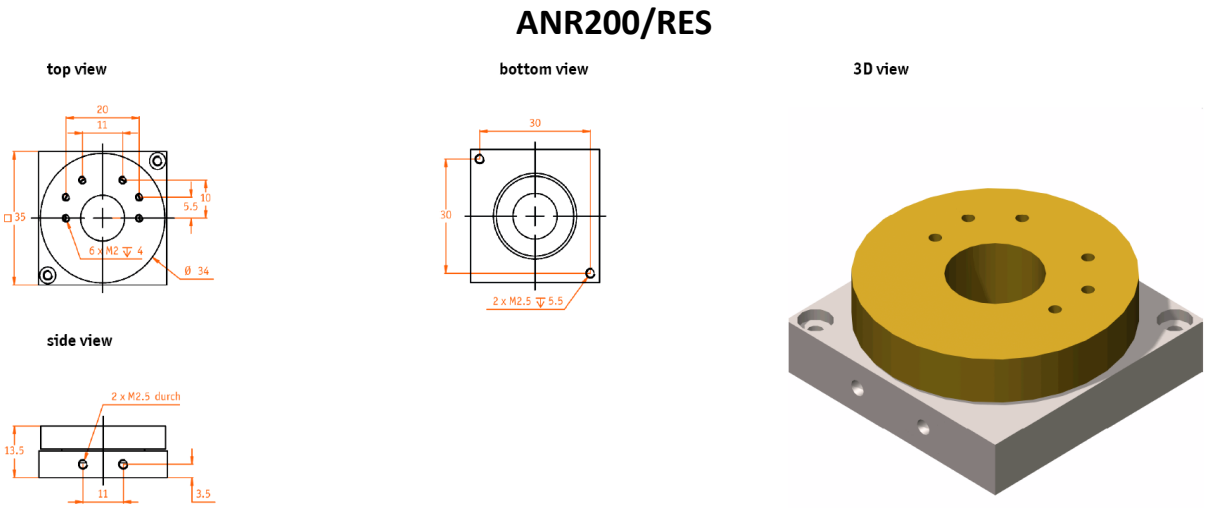

Figure D.9: Attocube nanopositioner ANR200/RES.

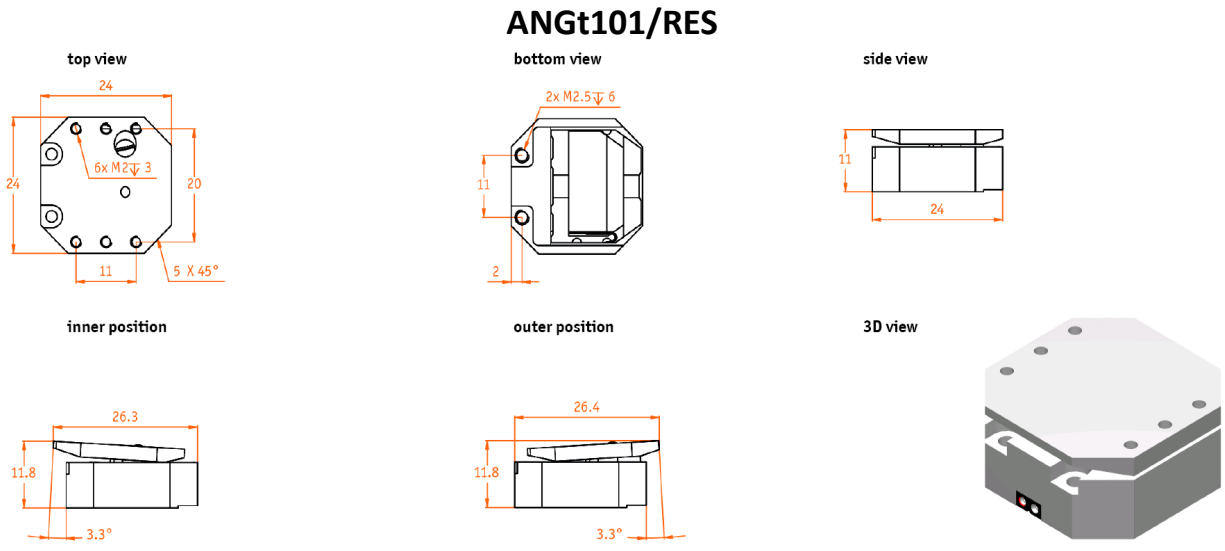

Figure D.10: Attocube nanopositioner ANGt101/RES.

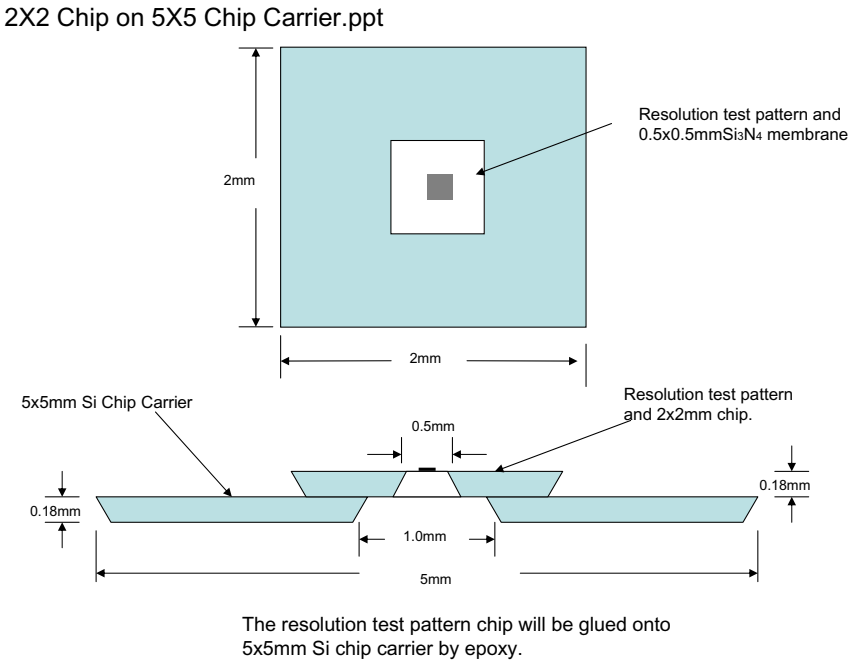

Figure D.11: Mounting of Siemens-star on Si-chip (for X50-30-7; as delivered from Xradia).

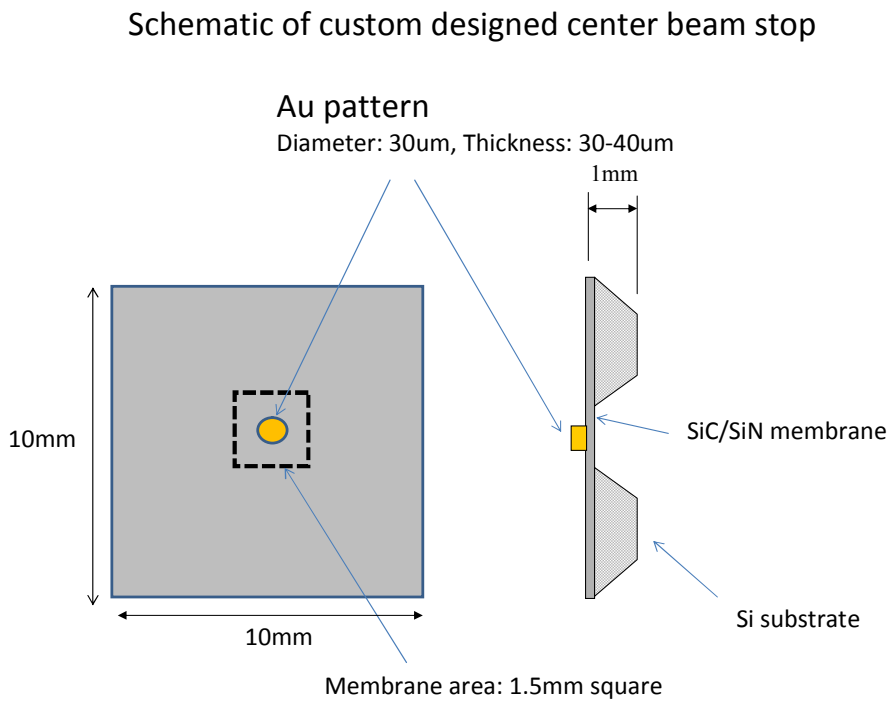

Figure D.12: Beam stop layout from NTT-AT.

Collaborations

The work for this thesis would not have been possible without the help of many people outside the institute. Here I want to sum-up all collaborations, which have been established during the time of this thesis:

For atomic layer deposition

The BMBF[1] research group **functional 3D-nanostructures by atomic layer deposition** at the **Max-Planck-Institute of Microstructure Physics at Halle (Saale)** (Dr. Mato Knez and Dr. Adriana Szeghalmi).

For theory on FZP efficiency

The **microscopy group of BESSY II** of the **Helmholtz Zentrum Berlin für Materialien und Energie** (Dr. Gerd Schneider, Dr. Stefan Rehbein and Dr. Peter Guttmann).

For hard X-ray experiments

Dr. Aanatoly Snigirev and Dr. Irina Snigireva at the **"techniques and instruments test beamline" ID6** (beamline staff: Dr. Carsten Detlefs and Dr. Thomas Roth) at the **European Synchrotron Radiation Facility (ESRF)**.

[1] Bundesministerium für Bildung und Forschung

List of Figures

List of Tables

Bibliography

[1] C. W. Röntgen, *Über eine neue art von strahlen - vorläufige mitteilung*, *Sitzungsberichte der Würzburger Physikalisch-Medizinischen Gesellschaft* (1895).

[2] C. W. Röntgen, *Über eine neue art von strahlen - ii. mitteilung*, *Sitzungsberichte der Würzburger Physikalisch-Medizinischen Gesellschaft* (1896).

[3] J. H. Underwood and D. T. Attwood, *The renaissance of x-ray optics*, *PHYSICS TODAY* , April: pp. 44–52 (1984).

[4] V. Aristov, *Recent advances in x-ray refractive optics*, *Physics Uspekhi* **51**, 1: pp. 57–77 (2008).

[5] G. Schmahl, D. Rudolph, G. Schneider, J. Thieme, T. Schliebe and B. Kaulich, *Diffraction optics for x-ray imaging*, *Microelectronic engineering* **32**, 1-4: pp. 351–367 (1996).

[6] D. T. Attwood, *SOFT X-RAYS AND EXTREME ULTRAVIOLET RADIATION - Principles and Applications* (Cambridge University Press, 1999).

[7] P. Rai-Chordhury, editor, *Handbook of Microlithography, Micromachining and Microfabrication Volume 1: Microlithography* (SPIE - The International Society for Optical Engineering, 1997).

[8] J. Vila-Comamala, K. Jefimovs, J. Raabe, T. Pilvi, R. Fink, M. Senoner, A. Maaßdorf, M. Ritala and C. David, *Advanced thin film technology for ultrahigh resolution x-ray microscopy*, *Ultramicroscopy* **109**, 11: pp. 1360 – 1364 (2009).

[9] D. RUDOLPH and G. SCHMAHL, *High power zone plates for a soft x-ray microscope*, *PARSONS, D. F. (ED.). ANNALS OF THE NEW YORK ACADEMY*

OF SCIENCES, VOL. 342. ULTRASOFT X-RAY MICROSCOPY: ITS APPLICATION TO BIOLOGICAL AND PHYSICAL SCIENCES; MEETING, JUNE 13-15, 1979. VIII+402P. NEW YORK ACADEMY OF SCIENCES: NEW YORK, N.Y., USA. ILLUS pp. P94–104 (1980).

[10] A. C. Jones and M. L. Hitchman, editors, *Chemical Vapour Deposition Precursors, Processes and Applications* (The Royal Society of Chemistry, 2009), chapter 4.

[11] C. Volkert and A. Minor, *Focused ion beam microscopy and micromachining*, *MRS bulletin* **32**, 5: pp. 389–395 (2007).

[12] K. Wille, *Physik der Teilchenbeschleuniger und Synchrotronstrahlungsquellen. Eine Einführung* (Teubner Verlag, 1996).

[13] http://www.helmholtz-berlin.de/angebote/arbeiten-lernen/info/beschleunigerphysik-fuer-anfaenger/der-speicherring_de.html (2009).

[14] H. Kronmüller and S. Parkin, editors, *Handbook of Magnetism and Advanced Magnetic Materials*, volume 3 (John Wiley & Sons Ltd., 2007).

[15] H. Wende, *Recent advances in x-ray absorption spectroscopy*, *Reports on progress in physics* **67**, 12: pp. 2105–2181 (2004).

[16] G. SCHÜTZ, W. WAGNER, W. WILHELM, P. KIENLE, R. ZELLER and R. FRAHM, *Absorption of circularly polarized x-rays in iron*, *Physical review letters* **58**, 7: pp. 737–740 (1987).

[17] A. Thompson, *X-ray data booklet* (Lawrence Berkeley National Laboratory, 2009).

[18] A. Compton, *The total reflexion of x-rays*, *Philosophical magazine* **45**, 270: pp. 1121–1131 (1923).

[19] M. Feser, *Scanning transmission x-ray microscopy with a segmented detector*, Doktorarbeit, State University of New York at Stony Brook.

[20] H. Chapman and K. Nugent, *Coherent lensless x-ray imaging*, *Nature photonics* **4**, 12: pp. 833–839 (2010).

[21] A. Sakdinawat and D. Attwood, *Nanoscale x-ray imaging*, *Nature photonics* **4**, 12: pp. 840–848 (2010).

[22] http://www.cxro.lbl.gov/BL612/ (2011).

[23] H. Rarback, D. Shu, S. C. Feng, H. Ade, J. Kirz, L. McNulty, D. P. Kern, T. H. P. Chang, Y. Vladimirsky, N. Iskander, D. Attwood, K. McQuaid and S. Rothman, *Scanning x-ray microscope with 15-nm resolution*, *Review of Scientific Instruments* (1988).

[24] B. Niemann, D. Rudolph and G. Schmahl, *X-ray microscopy with synchrotron radiation*, *APPLIED OPTICS* (1976).

[25] G. Schmahl, D. Rudolph, B. Niemann and O. Christ, *Zone-plate x-ray microscopy*, *Quarterly Reviews of Biophysics* (1980).

[26] G. Schneider, P. Guttmann, S. Heim, S. Rehbein, D. Eichert and B. Niemann, *X-ray microscopy at bessy: From nano-tomography to fs-imaging*, in J.-Y. Choi and S. Rah, editors, *Synchrotron Radiation Instrumentation: Ninth International Conference*, volume CP879, pp. 1291–1294 (American Institute of Physics, 2007).

[27] T. Eimuller, B. Niemann, P. Guttmann, P. Fischer, U. Englisch and R. Vatter, *The magnetic transmission x-ray microscopy project at bessy ii*, *JOURNAL DE PHYSIQUE IV* **104**: pp. 91–94 (2003).

[28] P. Guttmann, X. Zeng, M. Feser, S. Heim, W. Yun and G. Schneider, *Ellipsoidal capillary as condenser for the bessy full-field x-ray microscope*, *9TH INTERNATIONAL CONFERENCE ON X-RAY MICROSCOPY* **186** (2009).

[29] P. Dhez, P. Chevallier, T. Lucatorto and C. Tarrio, *Instrumental aspects of x-ray microbeams in the range above 1 kev*, *Review of scientific instruments* **70**, 4: pp. 1907–1920 (1999).

[30] A. SNIGIREV, *The recent development of bragg-fresnel crystal optics - experiments and applications at the esrf (invited)*, *Review of scientific instruments* **66**, 2: pp. 2053–2058 (1995).

[31] P. KIRKPATRICK and A. V. BAEZ, *Formation of optical images by x-rays*, *JOURNAL OF THE OPTICAL SOCIETY OF AMERICA* **38**, 9: pp. 766–774 (1948).

[32] P. Kirkpatrick, *The x-ray mircoscope*, *Scientific American* **180**: pp. 44–47 (1949).

[33] H. Mimura, S. Matsuyama, H. Yumoto, H. Hara, K. Yamamura, Y. Sano, M. Shibahra, K. Endo, Y. Mori, Y. Nishino, K. Tamasaku, M. Yabashi, T. Ishikawa and K. Yamauchi, *Hard x-ray diffraction-limited nanofocusing with kirkpatrick-baez mirrors*, *Japanese Journal of Applied Physics* **44**: pp. 539–542 (2005).

[34] Y. Mori, K. Yamauchi, K. Yamamura and Y. Sano, *Development of plasma chemical vaporization machining*, *Review of scientific instruments* **71**, 12: pp. 4627–4632 (2000).

[35] H. Mimura, K. Yamauchi, K. Yamamura, A. Kubota, S. Matsuyama and Y. Sano, *Image quality improvement in a hard x-ray projection microscope using total reflection mirror optics*, *Journal of synchrotron radiation* **11**: pp. 343–346 (2004).

[36] H. Wolter, *Spiegelsysteme streifenden einfalls als abbildende optiken für röntgenstrahlen*, *Annalen der Physik* **Band 10**: pp. 94–114 (1952).

[37] F. Jansen, D. Lumb, B. Altieri, J. Clavel, M. Ehle and C. Erd, *Xmm-newton observatory. i. the spacecraft and operations*, *Astronomy and astrophysics* **vol.365, no.1**: pp. L1–6 (2001).

[38] I. KOZHEVNIKOV and A. VINOGRADOV, *Multilayer x-ray mirrors*, *Journal of Russian laser research* **16**, 4: pp. 343–385 (1995).

[39] E. Spiller, *X-ray optics*, in *Advances in X-ray Analysis*, volume 42, pp. 297–307 (JCPDS-International Centre for Diffraction Data, 1998).

[40] J. T. W. Barbee, *Multilayers for x-ray optics* **25**: pp. 893–915 (1986).

[41] E. Spiller, *X-ray Zone Plate Fabrication Using a Focused Ion Beam* (SPIE-The International Society for Optical Engineering, 1994).

[42] S. GAPONOV, S. GUSEV, B. LUSKIN, N. SALASHCHENKO and E. GLUSKIN, *Long-wave x-ray-radiation mirrors*, *Optics communications* **38**, 1: pp. 7–9 (1981).

[43] A. Szeghalmi, S. Senz, M. Bretschneider, U. Goesele and M. Knez, *All dielectric hard x-ray mirror by atomic layer deposition*, *APPLIED PHYSICS LETTERS* **94**, 13 (2009).

[44] A. WALKER, T. BARBEE, R. HOOVER and J. LINDBLOM, *Soft-x-ray images of the solar corona with a normal-incidence cassegrain multilayer telescope*, *Science* **241**, 4874: pp. 1781–1787 (1988).

[45] J. Goldsmith, K. Berger, D. Bozman, G. Cardinale, D. Folk and C. Henderson, *Sub-100-nm lithographic imaging with an euv 10x microstepper*, *Proceedings of SPIE–the international society for optical engineering* **3676** (1999).

[46] F. CERRINA, G. MARGARITONDO, J. UNDERWOOD, M. HETTRICK, M. GREEN and L. BRILLSON, *Maximum - a scanning photoelectron microscope at aladdin*, *Nuclear instruments&methods in physics research. Section A, Accelerators, spectrometers, detectors and associated equipment* **266**, 1-3: pp. 303–307 (1988).

[47] H. Mimura, S. Handa, T. Kimura, H. Yumoto, D. Yamakawa, H. Yokoyama, S. Matsuyama, K. Inagaki, K. Yamamura, Y. Sano, K. Tamasaku, Y. Nishino, M. Yabashi, T. Ishikawa and K. Yamauchi, *Breaking the 10nm barrier in hard-x-ray focusing*, *NATURE Physics* pp. 1–4 (2009).

[48] M. KUMAKHOV and F. KOMAROV, *Multiple reflection from surface x-ray optics*, *Physics reports* **191**, 5: pp. 289–350 (1990).

[49] C. MacDonald and W. Gibson, *Applications and advances in polycapillary optics*, *X-ray spectrometry* **32**, 3: pp. 258–268 (2003).

[50] C. S. W., *The handbook of x-ray single-bounce monocapillary optics, including optical design and synchrotron applications*, Doktorarbeit, Cornell University (2008).

[51] X. Zeng, F. Duewer, M. Feser, C. Huang, A. Lyon, A. Tkachuk and W. Yun, *Ellipsoidal and parabolic glass capillaries as condensers for x-ray microscopes*, *APPLIED OPTICS* (2008).

[52] T. Tomie, *The birth of the x-ray refractive lens*, *Spectrochimica acta. Part B, Atomic spectroscopy* **65**, 3: pp. 192–198 (2010).

[53] A. Snigirev, V. Kohn, I. Snigireva and B. Lengeler, *A compound refractive lens for focusing high-energy x-rays*, *Nature* **384**, 6604: pp. 49–51 (1996).

[54] A. Snigirev, V. Kohn, I. Snigireva, A. Souvorov and B. Lengeler, *Focusing high-energy x rays by compound refractive lenses*, *Applied optics-OT* **37**, 4: pp. 653–662 (1998).

[55] B. Lengeler, C. Schroer, J. Tummler, B. Benner, M. Richwin and A. Snigirev, *Imaging by parabolic refractive lenses in the hard x-ray range*, *Journal of synchrotron radiation* **6**: pp. 1153–1167 (1999).

[56] B. Lengeler, C. Schroer, M. Richwin, J. Tummler, M. Drakopoulos and A. Snigirev, *A microscope for hard x rays based on parabolic compound refractive lenses*, *Applied physics letters* **74**, 26: pp. 3924–3926 (1999).

[57] B. Lengeler, C. Schroer, B. Benner, A. Gerhardus, T. Gunzler and M. Kuhlmann, *Parabolic refractive x-ray lenses*, *Journal of synchrotron radiation* **9**: pp. 119–124 (2002).

[58] C. Schroer, M. Kuhlmann, U. Hunger, T. Gunzler, O. Kurapova and S. Feste, *Nanofocusing parabolic refractive x-ray lenses*, *Applied physics letters* **82**, 9: pp. 1485–1487 (2003).

[59] C. Schroer and B. Lengeler, *Focusing hard x rays to nanometer dimensions by adiabatically focusing lenses*, *Physical review letters* **94**, 5 (2005).

[60] V. Nazmov, E. Reznikova, A. Somogyi, J. Mohr and V. Saile, *Planar sets of cross x-ray refractive lenses from su-8 polymer*, *Proceedings of SPIE–the international society for optical engineering* **5539**: pp. 235–243 (2004).

[61] E. Reznikova, T. Weitkamp, V. Nazmov, A. Last, M. Simon and V. Saile, *Investigation of phase contrast hard x-ray microscopy using planar sets of refractive crossed linear parabolic lenses made from su-8 polymer*, *Physica status solidi. A, Applied research* **204**, 8: pp. 2811–2816 (2007).

[62] Y. Dudchik and N. Kolchevsky, *A microcapillary lens for x-rays*, *Nuclear instruments & methods in physics research. Section A, Accelerators, spectrometers, detectors and associated equipment* **421**, 1-2: pp. 361–364 (1999).

[63] Y. Kohmura, M. Awaji, Y. Suzuki, T. Ishikawa, Y. Dudchik and N. Kolchevsky, *X-ray focusing test and x-ray imaging test by a microcapillary x-ray lens at an undulator beamline*, *Review of scientific instruments* **70**, 11: pp. 4161–4167 (1999).

[64] Y. Dudchik, F. Komarov, M. Piestrup, C. Gary, H. Park and J. Cremer, *Using of a microcapillary refractive x-ray lens for focusing and imaging*, *Spectrochimica acta. Part B, Atomic spectroscopy* **62**, 6-7: pp. 598–602 (2007).

[65] E. Hecht, *Optics 4th edition* (Addison Wesley, 2002).

[66] J. L. Soret, *Über die durch kreisgitter erzeugten diffraktionsphänomene*, *Annalen der Physik und Chemie* **156**: pp. 99–113 (1875).

[67] R. Wood, *Phase-reversal zone-plates, and diffraction-telescopes*, *The Philosophical magazine* pp. 511–522 (1898).

[68] A. BAEZ, *Resolving power in diffraction microscopy with special reference to x-rays*, *Nature* **169**, 4310: pp. 963–964 (1952).

[69] A. BAEZ, *A study in diffraction microscopy with special reference to x-rays*, *Journal of the Optical Society of America* **42**, 10: pp. 756–762 (1952).

[70] A. BAEZ, *A study in diffraction microscopy with special reference to x-rays*, *Journal of the Optical Society of America* **42**, 10: pp. 756–762 (1952).

[71] A. BAEZ, *Self-supporting metal fresnel zone-plate to focus extreme ultra-violet and soft x-rays*, *Nature* **186**, 4729: pp. 958–958 (1960).

[72] A. BAEZ, *Fresnel zone plate for optical image formation using extreme ultraviolet and soft x radiation*, *Journal of the Optical Society of America* **51**, 4: p. 405 (1961).

[73] J. KIRZ, *PHASE ZONE PLATES FOR X-RAYS AND EXTREME UV*, *JOURNAL OF THE OPTICAL SOCIETY OF AMERICA* **64**, 3: pp. 301–309 (1974).

[74] W. B. Yun, P. J. Viccaro, B. Lai and J. Chrzas, *Coherent hard x-ray focusing optics and applications*, *Review of Scientific Instruments* **63**: pp. 582–585 (1992).

[75] J. MASER and G. SCHMAHL, *COUPLED WAVE DESCRIPTION OF THE DIFFRACTION BY ZONE PLATES WITH HIGH ASPECT RATIOS*, *OPTICS COMMUNICATIONS* **89**, 2-4: pp. 355–362 (1992).

[76] G. Schneider, *Zone plates with high efficiency in high orders of diffraction described by dynamical theory*, *APPLIED PHYSICS LETTERS* **71**, 16: pp. 2242–2244 (1997).

[77] G. Schneider, *Influence of roughness and interdiffusion in zone plate structures on the diffraction efficiency described by coupled wave theory*, *APPLIED PHYSICS LETTERS* **73**, 5: pp. 599–601 (1998).

[78] G. SCHMAHL and D. RUDOLPH, *Lichtstarke zonenplatten als abbildende systeme für weiche röntgenstrahlung*, *Optik* **29**, 6: p. 577 (1969).

[79] N. Ceglio, *The impact of microfabrication technology on x-ray optics*, *AIP conference proceedings* **no.75**: pp. 210–22 (1981).

[80] D. Sayre, *Proposal for the utilization of electron beam technology in the fabrication of an image forming device for the soft x-ray region*, *Technical Report RC* **3974**, 17965 (1972).

[81] M. Altissimo, F. Romanato, L. Vaccari, L. Businaro, D. Cojoc and B. Kaulich, *X-ray lithography fabrication of a zone plate for x-rays in the range from 15 to 30 kev*, *Microelectronic engineering* **61-62**: pp. 173–177 (2002).

[82] A. Stein, C. Jacobsen, K. E. Lutterodt, D. Tennant, G. Bogart and F. Klemens, *Diffractive x-ray optics using production fabrication methods*, *Journal of vacuum science & technology. B, Microelectronics and nanometer structures processing, measurement and phenomena* **21**, 1: pp. 214–219 (2003).

[83] P. Ilinski, B. Lai, N. Bassom, J. Donald and G. Athas, *X-ray zone plate fabrication using a focused ion beam*, *Proceedings of SPIE–the international society for optical engineering* **vol.4145**: pp. 311–16 (2001).

[84] D. SHAVER, D. FLANDERS, N. CEGLIO and H. SMITH, *X-ray zone plates fabricated using electron-beam and x-ray-lithography*, *Journal of vacuum science and technology* **16**, 6: pp. 1626–1630 (1979).

[85] D. KERN, P. COANE, R. ACOSTA, T. CHANG, R. FEDER and P. HOUZEGO, *Electron-beam fabrication and characterization of fresnel zone plates for soft-x-ray microscopy*, *Proceedings of the Society of Photo-optical Instrumentation Engineers* **447**: pp. 204–213 (1984).

[86] F. van Delft, J. Weterings, and H. Romijn, *Hydrogen silsesquioxane/novolak bilayer resist for high aspect ratio nanoscale electron-beam lithography*, *Journal of vacuum science & technology. B, Microelectronics and nanometer structures processing, measurement and phenomena* **18**, 6: pp. 3419–3423 (2000).

[87] D. Olynick, E. Anderson, B. Harteneck and E. Veklerov, *Substrate cooling efficiency during cryogenic inductively coupled plasma polymer etching for diffractive optics*

on membranes, *Journal of vacuum science and technology. B, Microelectronics and nanometer structures processing, measurement and phenomena* **19**, 6: pp. 2896–2900 (2001).

[88] E. Anderson, D. Olynick, B. Harteneck, E. Veklerov, G. Denbeaux and W. Chao, *Nanofabrication and diffractive optics for high-resolution x-ray applications*, *Journal of vacuum science and technology. B, Microelectronics and nanometer structures processing, measurement and phenomena* **18**, 6: pp. 2970–2975 (2000).

[89] M. Peuker, *High-efficiency nickel phase zone plates with 20 nm minimum outermost zone width*, *Applied physics letters* **78**, 15: pp. 2208–2210 (2001).

[90] W. Chao, E. Anderson, G. Denbeaux, B. Harteneck, J. Liddle, D. Olynick, A. Pearson, F. Salmassi, C. Song and D. Attwood, *20-nm resolution x-ray microscopy demonstrated by use of multilayer test structures*, *OPTICS LETTERS* **28**, 21: pp. 2019–2021 (2003).

[91] S. Rehbein, *Nanofabrication of diffractive optics for soft x-ray and atom beam focusing*, *JOURNAL DE PHYSIQUE IV* **104**: pp. 207–210 (2003).

[92] S. Rehbein, S. Heim, P. Guttmann, S. Werner and G. Schneider, *Ultrahigh-resolution soft-x-ray microscopy with zone plates in high orders of diffraction*, *Phys. Rev. Lett.* **103**, 11: p. 110801 (2009).

[93] S. Rehbein and G. Schneider, *Volume zone plate development at bessy*, in *Proc. 8th Int. Conf. X-ray Microscopy*, IPAP Conf. Series 7, pp. 103–106 (2005).

[94] S. Rehbein, P. Guttmann, S. Werner and G. Schneider, *Development of chemical-mechanical polished high-resolution zone plates*, *Journal of vacuum science and technology. B, Microelectronics and nanometer structures processing, measurement and phenomena* **25**, 6: pp. 1789–1793 (2007).

[95] S. Werner, S. Rehbein, P. Guttmann, S. Heim and G. Schneider, *Towards high diffraction efficiency zone plates for x-ray microscopy*, *Microelectronic engineering* **87**, 5-8: pp. 1557–1560 (2010).

[96] M. Lindblom, J. Reinspach, O. von Hofsten, M. Bertilson, H. Hertz and A. Holmberg, *High-aspect-ratio germanium zone plates fabricated by reactive ion etching in chlo-*

rine, *Journal of vacuum science and technology. B, Microelectronics and nanometer structures processing, measurement and phenomena* **27**, 2: pp. L1–L3 (2009).

[97] P. Charalambous, P. Anastasi, R. Burge and K. Popova, *Fabrication of high resolution x-ray diffractive optics at king's college, london*, *X-RAY MICROBEAM TECHNOLOGY AND APPLICATIONS* **2516**: pp. 2–14 (1995).

[98] P. Charalambous, *Fabrication and characterization of tungsten zone plates for multi kev x-rays*, *AIP conference proceedings* **507**: pp. 625–630 (2000).

[99] P. Charalambous, *Status of nanofabrication at zoneplates.com*, in *Proc. 8th Int. Conf. X-ray Microscopy*, IPAP Conf. Series 7, pp. 127–129 (2005).

[100] L. Ocola and A. Stein, *Effect of cold development on improvement in electron-beam nanopatterning resolution and line roughness*, *Journal of vacuum science and technology. B, Microelectronics and nanometer structures processing, measurement and phenomena* **24**, 6: pp. 3061–3065 (2006).

[101] J. Reinspach, M. Lindblom, O. von Hofsten, M. Bertilson, H. Hertz and A. Holmberg, *Cold-developed electron-beam-patterned zep 7000 for fabrication of 13 nm nickel zone plates*, *Journal of vacuum science and technology. B, Microelectronics and nanometer structures processing, measurement and phenomena* **27**, 6: pp. 2593–2596 (2009).

[102] W. Chao, B. Harteneck, J. Liddle, E. Anderson and D. Attwood, *Soft X-ray microscopy at a spatial resolution better than 15nm*, *NATURE* **435**, 7046: pp. 1210–1213 (2005).

[103] W. Chao, J. Kim, S. Rekawa, P. Fischer and E. H. Anderson, *Demonstration of 12 nm Resolution Fresnel Zone Plate Lens based Soft X-ray Microscopy*, *OPTICS EXPRESS* **17**, 20: pp. 17669–17677 (2009).

[104] K. Jefimovs, J. Vila-Comamala, T. Pilvi, J. Raabe, M. Ritala and C. David, *Zone-doubling technique to produce ultrahigh-resolution x-ray optics*, *Phys. Rev. Lett.* **99**, 26: p. 264801 (2007).

[105] J. V. Comamala, S. Gorelick, E. Farm, C. Kewish, A. Diaz and R. Barrett, *Ultra-high resolution zone-doubled diffractive x-ray optics for the multi-kev regime*, *Optics express* **19**, 1: pp. 175–184 (2011).

[106] S. Tamura, M. Yasumoto, T. Mihara, N. Kamijo, Y. Suzuki and M. Awaji, *Multilayer fresnel zone plate for high-energy x-ray by dc sputtering deposition*, *Vacuum* **66**, 3-4: pp. 495–499 (2002).

[107] D. RUDOLPH, B. NIEMANN and G. SCHMAHL, *Status of the sputtered sliced zone plates for x-ray microscopy*, *Proceedings of the Society of Photo-optical Instrumentation Engineers* **316**: pp. 103–105 (1981), ISSN 0361-0748.

[108] B. Kaulich, *Phase zone plates for hard X-ray microscopy*, in McNulty, I, editor, *X-RAY MICROFOCUSING: APPLICATIONS AND TECHNIQUES*, volume 3449 of *PROCEEDINGS OF THE SOCIETY OF PHOTO-OPTICAL INSTRUMENTATION ENGINEERS (SPIE)*, pp. 108–117 (1998), Conference on X-Ray Microfocusing - Applications and Techniques, SAN DIEGO, CA, JUL 22-23, 1998.

[109] A. Duvel, D. Rudolph and G. Schmahl, *Fabrication of thick zone plates for multi-kilovolt x-rays*, *AIP conference proceedings* **507**: pp. 607–614 (2000), ISSN 0094-243X, doi:10.1063/1.1291219.

[110] N. Kamijo, Y. Suzuki, M. Awajia, A. Takeuchi, K. Uesugi and M. Yasumoto, *Characterization of the sputtered-sliced zone plate for high energy x-rays*, *Nuclear instruments & methods in physics research. Section A, Accelerators, spectrometers, detectors and associated equipment* **467**: pp. 868–871 (2001).

[111] K. SAITOH, K. INAGAWA, K. KOHRA, C. HAYASHI, A. IIDA and N. KATO, *Characterization of sliced multilayer zone plates for hard x-rays*, *Review of scientific instruments* **60**, 7: pp. 1519–1523 (1989).

[112] N. KAMIJO, S. TAMURA, Y. SUZUKI and H. KIHARA, *Fabrication and testing of hard x-ray sputtered-sliced zone-plate*, *Review of scientific instruments* **66**, 2: pp. 2132–2134 (1995).

[113] M. Awaji, Y. Suzuki, A. Takeuchi, H. Takano, N. Kamijo and S. Tamura, *X-ray imaging microscopy at 25 kev with fresnel zone plate optics*, *Nuclear instruments & methods in physics research. Section A, Accelerators, spectrometers, detectors and associated equipment* **467**: pp. 845–848 (2001).

[114] M. Awaji, Y. Suzuki, A. Takeuchi, H. Takano, N. Kamijo and M. Yasumoto, *Microfocusing of 82 kev x rays with a sputtered-sliced fresnel zone plate*, *Review of scientific instruments* **74**, 11: pp. 4948–4949 (2003).

[115] N. Kamijo, Y. Suzuki, H. Takano, S. Tamura, M. Yasumoto and A. Takeuchi, *Microbeam of 100 kev x ray with a sputtered-sliced fresnel zone plate*, *Review of scientific instruments* **74**, 12: pp. 5101–5104 (2003).

[116] N. Kamijo, Y. Suzuki, A. Takeuchi, M. Itou and S. Tamura, *Microbeam of 200 kev x-ray with sputtered-sliced zone plate*, *Japanese journal of applied physics* **48**, 1 (2009).

[117] M. Yasumoto, S. Tamura, N. Kamijo, Y. Suzuki, M. Awaji, A. Takeuchi, H. Takano, Y. Kohmura and K. Handa, *Suppression of corrugated boundaries in multilayer fresnel zone plate for hard X-ray synchrotron radiation using cylindrical slit*, *JAPANESE JOURNAL OF APPLIED PHYSICS PART 1-REGULAR PAPERS SHORT NOTES & REVIEW PAPERS* **40**, 7: pp. 4747–4748 (2001).

[118] M. Yasumoto, S. Tamura, N. Kamijo, Y. Suzuki, M. Awaji and A. Takeuchi, *Computer-controlled fabrication of concentric multilayer fresnel zone plate for synchrotron radiation hard x-ray*, *Combinatorial and Artificial Intelligence Methods in Materials Science. Symposium (Materials Research Society Symposium Proceedings Vol.700)* p. 173 (2002).

[119] S. Tamura, M. Yasumoto, N. Kamijo, Y. Suzuki, M. Awaji and A. Takeuchi, *New approaches to fabrication of multilayer fresnel zone plate for high-energy synchrotron radiation x-rays*, *Vacuum* **80**, 7: pp. 823–827 (2006).

[120] S. Tamura, M. Yasumoto, N. Kamijo, A. Takeuchi, K. Uesugi and Y. Suzuki, *Multilevel-type multilayer X-ray lens (Fresnel zone plate) by sputter deposition*, *VACUUM* **83**, 3: pp. 691–694 (2008), 9th International Symposium on Sputtering and Plasma Processes, Kanazawa, JAPAN, JUN 06-08, 2007.

[121] S. Tamura, M. Yasumoto, N. Kamijo, A. Takeuchi, K. Uesugi, Y. Terada and Y. Suzuki, *Fabrication and testing of sputtered-sliced kinoform style Fresnel zone plate*, *VACUUM* **84**, 12, Sp. Iss. SI: pp. 1457–1459 (2010), 10th International Symposium on Sputtering and Plasma Processes, Kanazawa, JAPAN, JUL 08-10, 2009.

[122] M. Yasumoto, S. Tamura, N. Kamijo, K. Uesugi, A. Takeuchi and Y. Suzuki, *Observation of kinoform-style multilayer Fresnel zone plate by scanning ion microscopy*, *VACUUM* **84**, 5, Sp. Iss. SI: pp. 669–671 (2009), 4th Vacuum and Surface Science Conference of Asia and Australia, Matsue City, JAPAN, OCT 28-31, 2008.

[123] S. Tamura, K. Murai, N. Kamijo, K. Yoshida, H. Kihara and Y. Suzuki, *Focusing efficiency of a multilayer fresnel zone plate for hard x-ray fabricated by dc sputtering deposition*, *Vacuum* **59**, 2-3: pp. 553–558 (2000).

[124] Y. Suzuki, N. Kamijo, S. Tamura, K. Handa, A. Takeuchi and S. Yamamoto, *Hard x-ray microbeam experiment at the tristan main ring test beamline of the kek*, *Journal of synchrotron radiation* **4**: pp. 60–63 (1997).

[125] S. Tamura, M. Yasumoto, N. Kamijo, Y. Suzuki, M. Awaji and A. Takeuchi, *Novel application of sputtered-sliced concentric multilayers to various optical elements for synchrotron radiation high-brilliance x-ray beamlines at spring-8*, *Vacuum* **74**, 3-4: pp. 741–746 (2004).

[126] K. Golant, S. Lavrishchev, A. Popov, I. Artyukov, R. Feshchenko and A. Mitrofanov, *Fabrication of x-ray zone plates by surface-plasma chemical vapor deposition*, *Applied optics-OT* **46**, 23: pp. 5964–5966 (2007).

[127] I. Artyukov, I. Bukreeva, V. Chernov, R. Feshchenko, K. Golant and W. Jark, *Zone plates for hard x-rays fabricated with the spcvd technology*, *Nuclear instruments & methods in physics research. Section A, Accelerators, spectrometers, detectors and associated equipment* **603**, 1-2: pp. 66–68 (2009).

[128] H. Kang, G. Stephenson, C. Liu, R. Conley, A. Macrander and J. Maser, *Synchrotron x-ray study of multilayers in laue geometry*, *Proceedings of SPIE–the international society for optical engineering* **5537**: pp. 127–132 (2004).

[129] J. Maser, G. Stephenson, S. Vogt, W. Yun, A. Macrander and H. Kang, *Multilayer laue lenses as high-resolution x-ray optics*, *Proceedings of SPIE–the international society for optical engineering* **5539**: pp. 185–194 (2004).

[130] H. Kang, H. Yan, R. Winarski, M. Holt, J. Maser and C. Liu, *Focusing of hard x-rays to 16 nanometers with a multilayer laue lens*, *Applied physics letters* **92**, 22 (2008).

[131] H. Kang, G. Stephenson, C. Liu, R. Conley, R. Khachatryan and M. Wieczorek, *Sectioning of multilayers to make a multilayer laue lens*, *Review of scientific instruments* **78**, 4 (2007).

[132] T. Liese, V. Radisch and H. Krebs, *Fabrication of multilayer laue lenses by a combination of pulsed laser deposition and focused ion beam*, *Review of scientific instruments* **81**, 7 (2010).

[133] T. Suntola, J. Antson, A. Pakkala and S. Lindfors, *Atomic layer epitaxy for producing el-thin films*, *Digest of technical papers* p. 108 (1980).

[134] T. Suntola and J. Hyvarinen, *Atomic layer epitaxy*, *Annual review of materials science. Vol.15* p. 177 (1985).

[135] T. Suntola, *Atomic layer epitaxy*, *Materials science reports* **vol.4, no.7**: pp. 261–312 (1989).

[136] T. SUNTOLA, *Atomic layer epitaxy*, *Thin solid films* **216**, 1: pp. 84–89 (1992).

[137] M. Ritala and M. Leskelä, *Handbook of Thin Film Materials*, volume Volume 1: Deposition and Processing of thin films (Academic Press, 2002).

[138] R. Puurunen, *Surface chemistry of atomic layer deposition: A case study for the trimethylaluminum/water process*, *Journal of applied physics* **97**, 12 (2005).

[139] K. Kukli, J. Aarik, A. Aidla, H. Siimon, M. Ritala and M. Leskela, *In situ study of atomic layer epitaxy growth of tantalum oxide thin films from ta(oc2h5)(5) and h2o*, *Applied surface science* **112**: pp. 236–242 (1997).

[140] J. Gierak, *Focused ion beam technology and ultimate applications*, *Semiconductor science and technology* **24**, 4 (2009).

[141] A. Kilcoyne, T. Tyliszczak, W. Steele, S. Fakra, P. Hitchcock and K. Franck, *Interferometer-controlled scanning transmission x-ray microscopes at the advanced light source*, *Journal of synchrotron radiation* **10**: pp. 125–136 (2003).

[142] J. Raabe, G. Tzvetkov, U. Flechsig, M. Boge, A. Jaggi and B. Sarafimov, *Pollux: a new facility for soft x-ray spectromicroscopy at the swiss light source.*, *Review of scientific instruments* **79**, 11: p. 113704 (2008).

[143] R. Follath, J. Schmidt, M. Weigand and K. Fauth, *The x-ray microscopy beamline ue46-pgm2 at bessy*, *AIP conference proceedings* pp. 323–6 (2010).

[144] M. Weigand, *Dynamic behavior of magnetic vortex cores under pulsed excitation observed by scanning x-ray microscopy*, Doktorarbeit, Universität Stuttgart (2011), in preparation.

[145] J. Klaus and S. George, *Atomic layer deposition of sio2 at room temperature using nh3-catalyzed sequential surface reactions*, *Surface science* **447**, 1-3: pp. 81–90 (2000).

[146] J. Klaus, O. Sneh and S. George, *Growth of sio2 at room temperature with the use of catalyzed sequential half-reactions*, *Science* **278**, 5345: pp. 1934–1936 (1997).

[147] J. Ferguson, E. Smith, A. Weimer and S. George, *Ald of sio2 at room temperature using teos and h2o with nh3 as the catalyst*, *Journal of the Electrochemical Society* **151**, 8: pp. G528–G535 (2004).

[148] D. Hausmann, J. Becker, S. Wang and R. Gordon, *Rapid vapor deposition of highly conformal silica nanolaminates*, *Science* **298**, 5592: pp. 402–406 (2002).

[149] J. Bachmann, R. Zierold, Y. Chong, R. Hauert, C. Sturm and R. Schmidt-Grund, *A practical, self-catalytic, atomic layer deposition of silicon dioxide*, *Angewandte Chemie (International ed. in English)* **47**, 33: pp. 6177–6179 (2008).

[150] J. Maser, *Theoretische beschreibung der beugungs- und abbildungseigenschaften hochauflösender zonenplatten für die röntgenmikroskopie*, Doktorarbeit, Universität Göttingen (1993).

[151] M. SIMPSON and A. MICHETTE, *IMAGING PROPERTIES OF MODIFIED FRESNEL ZONE PLATES*, *OPTICA ACTA* **31**, 4: pp. 403–413 (1984).

[152] T. Liese, V. Radisch, I. Knorr, M. Reese, P. Grossmann and K. Mann, *Development of laser deposited multilayer zone plate structures for soft x-ray radiation*, *Applied surface science* **257**, 12: pp. 5138–5141 (2011).

[153] Y. VLADIMIRSKY and H. KOOPS, *Moire method and zone plate pattern inaccuracies*, *Journal of vacuum science & technology. B, Microelectronics and nanometer structures processing, measurement and phenomena* **6**, 6: pp. 2142–2146 (1988).

[154] S. Rehbein (2010), private communication.

[155] B. Niemann, P. Guttmann, S. Rehbein and C. Knochel, *Concept and realization of the novel rotating condenser-monochromator at the gottingen txm at bessy ii*, *JOURNAL DE PHYSIQUE IV* **104**: pp. 273–276 (2003).

[156] N. Kamijo, Y. Suzuki, M. Awaji, A. Takeuchi, H. Takano and T. Ninomiya, *Hard x-ray microbeam experiments with a sputtered-sliced fresnel zone plate and its applications*, *Journal of synchrotron radiation* **9**: pp. 182–186 (2002).

[157] J. Kirz and C. Jacobsen, *The history and future of x-ray microscopy*, *9TH INTERNATIONAL CONFERENCE ON X-RAY MICROSCOPY* **186** (2009).